GAMMA RAYS ASSOCIATED WITH NEUTRON SCATTERING IN FUSION REACTOR MATERIALS

by

PAUL CHRISTOPHER WARNER

MAY 1984

This thesis is submitted in part-fulfilment of the requirements for the Doctor of Philosophy in Nuclear Physics at the Department of Physics, University of Aston in Birmingham

ACKNOWLEDGEMENTS

I would like to thank Dr A.J. Cox for his guidance and supervision throughout the project. Furthermore, I thank the following people:

Mr J. Phull, Laboratory Technician at Aston University for his assistance in practical work, Dr N. Taylor and Dr L. Baker for their assistance in analysis at A.E.R.E. Harwell; Mrs Susan Glendon for typing the thesis and, finally, my parents for their continuing support.

The work was carried out with a SERC CASE award in association with the Culham Laboratories.

THE UNIVERSITY OF ASTON IN BIRMINGHAM

GAMMA-RAYS ASSOCIATED WITH NEUTRON SCATTERING IN FUSION REACTOR MATERIALS

Thesis for Degree of Ph.D.

by

PAUL CHRISTOPHER WARNER

SUBMISSION 1984

ABSTRACT

The gamma-rays produced by the inelastic scattering of 14 MeV neutrons in fusion reactor materials have been studied using a gamma-ray spectrometer employing a sodium iodide scintillation detector. The source neutrons are produced by the $T(d,n)^4He$ reaction using the SAMES accelerator at the University of Aston in Birmingham. In order to eliminate the large gamma-ray background and neutron signal due to the sensitivity of the sodium iodide detector to neutrons, the gamma-ray detector is heavily shielded and is used together with a particle time of flight discrimination system based on the associated particle time of flight method. The instant of production of a source neutron is determined by detecting the associated alpha-particle enabling discrimination between the neutrons and gamma-rays by their different time of flight times. The electronic system used for measuring the time of flight of the neutrons and gamma-rays over the fixed flight path is described.

The materials studied in this work were Lithium and Lead because of their importance as fuel breeding and shielding materials in conceptual fusion reactor designs. Several sample thicknesses were studied to determine the multiple scattering effects. The observed gamma-ray spectra from each sample at several scattering angles in the angular range 0° - 90° enabled absolute differential gamma-ray production cross-sections and angular distributions of the resolved gamma-rays from Lithium to be measured and compared with published data. For the Lead sample, the absolute differential gamma-ray production cross-sections for discrete 1 MeV ranges and the angular distributions were measured.

The measured angular distributions of the present work and those on Iron from previous work are compared to the predictions of the Monte Carlo programme M.O.R.S.E. Good agreement was obtained between the experimental results and the theoretical predictions. In addition an empirical relation has been constructed which describes the multiple scattering effects by a single parameter and is capable of predicting the gamma-ray production cross-sections for the materials to an accuracy of ± 25%.

Inelastic Scattering / Fast Neutrons / Gamma-Rays / Production Cross-Sections / Fusion Materials.

CONTENTS

		Page No.
	Acknowledgements	i
	Abstract	ii
CHAPTER 1:	INTRODUCTION	
1.1	Introduction	2
1.2	Aim of project	6
CHAPTER 2:	GENERAL CONSIDERATIONS	
2.1	Kinematics of the $T(d,n)^4He$ reaction	10
2.2	Interaction of gamma rays in matter	18
2.2.2	Pair production	21
2.2.3	Scattering of gamma rays	22
CHAPTER 3:	DESCRIPTION OF APPARATUS	
3.1	Production of neutrons	30
3.2	The alpha detector	33
3.2.1	Design of the alpha detector	34
3.3	The gamma ray detector	36
3.3.1	Description of detector	45
3.3.2	Efficiency of the gamma ray detector	47
3.4	Shielding of the NaI(Tl) detector	52
3.5	Description of the electronics	54
3.5.1	Time of flight electronics	56
3.5.2	Calibration of linear line	61
CHAPTER 4:	EXPERIMENTAL PROCEDURE AND RESULTS	
4.1	Experimental procedure	65
4.2	Differential cross-section measurement	68
4.2.1	Gamma ray self-absorption factor	69
4.2.2	Geometry factor correction	71
4.2.3	Efficiency of the detector	71

		Page No.
4.2.4	Background correction factor F_1	73
4.2.5	Neutron absorption in target assembly	75
4.3	Measurement of $P(\theta)$	76
4.4	Experimental results section	83
4.4.1	Interpretation of LiF spectra	85
4.4.2	Discussion of results for LiF	97
4.4.3	Comparison of thin sample gamma ray production cross-section at 90°	98
4.4.4	Interpretation of lead spectra	99
4.4.5	Discussion of lead results	117

CHAPTER 5: METHODS OF ANALYSING MULTIPLE SCATTERING

5.1	Methods of analysing multiple scattering	121
5.2	Monte Carlo methods	125
5.2.1	Path length	126
5.2.2	Reaction type	127
5.2.3	Elastic scattering	128
5.2.4	Inelastic scattering	129
5.3	More general methods	132
5.4	Terminating neutron histories and the method of statistical weights	134
5.5	Computing techniques in neutron transport problems	137
5.6	The M.O.R.S.E. code	139
5.6.1	User	139
5.6.2	Source	139
5.6.3	Cross-section	140
5.6.4	Geometry	145
5.6.5	Walk	148
5.6.6	Analysis	150
5.6.7	Errors	153
5.7	Notes for comparison of theoretical and experimental multiple scattering effects in iron samples	163

Page No.

CHAPTER 6: DISCUSSION OF RESULTS AND FINAL CONCLUSIONS

6.1 Discussion of results and final conclusions 171

6.2 Generalization 173

6.3 Further improvements 182

APPENDICES

Appendix 1 Programme in BASIC for geometry factor calculation 186

Appendix 2 Legendre polynomial fitting 187

Appendix 3 One dimensional consideration of multiple scattering 189

REFERENCES 191

LIST OF TABLES

		Page No.
TABLE 2.1	Table from Benviste and Zenger[11]	13
TABLE 2.2	Tabulation for neutron beam profile	16
TABLE 2.3	Interaction of gamma rays in matter	18
TABLE 4.1	Tabulation of constants for measurement of $P(\theta)$	80
TABLE 4.2	Variation of gamma ray production cross-section of ^{7}Li with thickness of sample	89
TABLE 4.3	Tabulated experimental results for 4cm thick LiF sample	91
TABLE 4.4	Tabulated experimental results for 9cm thick LiF samples	91
TABLE 4.5	Tabulated angular distribution for 22cm LiF samples	92
TABLE 4.6	Legendre fitting parameters for LiF angular data	93
TABLE 4.7	Tabulated differential cross-sections for gamma ray production and its variation with thickness of lead samples	102
TABLE 4.8	Fitting parameters for lead samples	103
TABLE 4.9	Tabulated angular distributions for gamma ray production in 2.7cm lead samples	107
TABLE 4.10	Legendre fitting parameters for lead samples	108
TABLE 4.11	Tabulated angular distribution for gamma ray production in 10cm lead samples	112
TABLE 4.12	Comparison of data for lead cross-sections	118
TABLE 5.1	100 Group neutron structure	142
TABLE 5.2	21 Group gamma ray structure	143
TABLE 5.3	Tabulated M.O.R.S.E. results for gamma ray production cross-section of ^{7}Li	155
TABLE 5.4	M.O.R.S.E. results for lead	157
TABLE 5.5	Tabulated results for iron (M.O.R.S.E.)	165

		Page No.
TABLE 5.6	Previous results from Aston[40] (experimental)	165
TABLE 5.7	Results from iron after using continuous gamma data from L Cranberg[61] to correct group 1-2MeV for the 1.24MeV level	165
TABLE 6.1	Ratio of $\frac{d\sigma_o}{d\Omega} / \frac{d\sigma}{d\Omega}$ (0.2) thin for all work undertaken in project	175
TABLE 6.2	Comparison of Day's[9] results with the theoretically predicted results for the gamma ray production cross-section due to excitation of the 0.845MeV level in iron	178
TABLE 6.3	Comparison of Al-Shalabi's[40] results with the theoretically predicted results for the differential cross-section at 90° due to the excitation of the 0.845MeV level in iron	180

LIST OF FIGURES

		Page No.
FIGURE 1.1	Future conceptual design for a working fusion reactor	4
FIGURE 2.1	Neutron-alpha angular relationship for a 7° Alpha aperture	12
FIGURE 2.2	Neutron yield shape	14
FIGURE 2.3	Neutron beam profile	15
FIGURE 2.4	Angular relationships in the lab frame	17
FIGURE 2.5	Mass absorption variation with energy of photons (Price et al.[14])	26
FIGURE 2.6	Compton differential scattering cross-section per electron as a function of energy	27
FIGURE 2.7	Scattering absorption cross-section per electron for light and heavy elements as a function of photon energy (White[20])	27
FIGURE 2.8	Narrow beam mass absorption coefficients as a function of energy for a number of differential elements (White[20])	28
FIGURE 3.1	Schematic diagram of accelerator	31
FIGURE 3.2	Target assembly	32
FIGURE 3.3	Cobalt 60 gamma ray spectrum from Ge(Li) and NaI(Tl) detectors	37
FIGURE 3.4	Dynode resistor chain used for the 56/AVP photomultiplier tube used in the gamma ray detector	46
FIGURE 3.5	Peak to total ratio as a function of energy for the 762 - 762mm NaI(Tl) detector	50
FIGURE 3.6	Efficiency of NaI(Tl) detector as a function of energy	51
FIGURE 3.7	Constituents of gamma ray detector shield	53
FIGURE 3.8	Complete circuit for gamma ray spectrometer	55
FIGURE 3.9	Time of flight circuit	57

Page No.

FIGURE 3.10	Circuit for setting alpha discriminator	58
FIGURE 3.11	Alpha particle pulse height spectrum	59
FIGURE 3.12	Direct beam	62
FIGURE 3.13	Time spectrum for LiF (9cm) sample showing resolution of gamma peak	62
FIGURE 3.14	Circuit used to calibrate linear line	63
FIGURE 4.1	Schematic diagram of the laboratory arrangements	66
FIGURE 4.2	Plan view of sample for calculation of $S(\theta,E,x)$	70
FIGURE 4.3	Illustration of geometry factor calculation	72
FIGURE 4.4	Method of graphical stripping	81
FIGURE 4.5	Illustration of Covell's method	82
FIGURE 4.6	Typical LiF spectrum for 9cm sample at 60°	86
FIGURE 4.7	Level structure of ^{7}Li (Ref. 50)	87
FIGURE 4.8	Level structure of ^{19}F (Ref. 51)	88
FIGURE 4.9	Variation of measured cross-section with thickness of LiF sample	90
FIGURE 4.10	Angular distribution for gamma ray production from de-excitation of the 0.478MeV level in ^{7}Li using 22cm thick LiF samples	94
FIGURE 4.11	Angular distribution for gamma ray production from de-excitation of the 0.478MeV level in ^{7}Li using 4cm thick LiF samples	95
FIGURE 4.12	Angular distribution for gamma ray production from de-excitation of the 0.478MeV level in ^{7}Li using 9cm thick LiF samples	96
FIGURE 4.13	Energy levels in lead isotopes (Ref. 55)	100

Page No.

FIGURE 4.14	Gamma ray spectrum from 15cm lead sample at 90°	101
FIGURE 4.15	Variation of measured differential cross-section with thickness of lead samples for the gamma ray energies illustrated	104
FIGURE 4.16	Variation in measured cross-section with thickness of lead samples for the gamma ray energies illustrated	105
FIGURE 4.17	Variation in measured cross-section with thickness of lead samples for the 2.3MeV gamma ray energy group	106
FIGURE 4.18	Angular distributions of 2.7cm thick lead samples for the gamma ray energy regions shown	109
FIGURE 4.19	Angular distributions for the 2.7cm lead samples for the gamma ray energy sections shown	110
FIGURE 4.20	Angular distribution for 2.7cm lead samples for the gamma ray energy group 0.65-1MeV	111
FIGURE 4.21	Angular distribution for the production of gamma rays in the 2-3MeV region for 10cm lead samples	113
FIGURE 4.22	Angular distribution of gamma rays in the 4-5MeV region for 10cm thick lead samples	114
FIGURE 4.23	Angular distribution for 10cm lead samples	115
FIGURE 4.24	Angular distribution for production of gamma rays in the 0.65-1MeV region in 10cm thick lead samples	116
FIGURE 5.1	Effect of multiple scattering on measured cross-section by Day (9) using 2.6MeV neutrons to excite the 0.845MeV level in iron samples	123
FIGURE 5.2	A simple Monte Carlo problem	125
FIGURE 5.3	Computing techniques in Monte Carlo methods	138
FIGURE 5.4	Structure of matrix in which cross-sections are stored on the DLC-37F library tape	144
FIGURE 5.5	Boolean algebra of combining standard shapes	146

Page No.

FIGURE 5.6	Combinational geometry simulation of laboratory experiments	147
FIGURE 5.7	Random walk generating package	149
FIGURE 5.8	Comparison of experimental and M.O.R.S.E. results for gamma ray production differential cross-sections in ^{7}Li (0.478MeV level)	156
FIGURE 5.9	Comparison of M.O.R.S.E. and experimental results for lead samples in the 1-2MeV region	158
FIGURE 5.10	Comparison of M.O.R.S.E. and experimental results for lead samples in the 2-3MeV region	159
FIGURE 5.11	M.O.R.S.E. results for lead samples in the 0.4-1MeV region	160
FIGURE 5.12	Comparison of M.O.R.S.E and experimental results for lead samples in the 3-4MeV region	161
FIGURE 5.13	Comparison of M.O.R.S.E and experimental results for lead samples in the 4-5MeV region	162
FIGURE 5.14	Comparison of M.O.R.S.E and experiment on the 1.24MeV level in iron samples	166
FIGURE 5.15	M.O.R.S.E. results for iron in the 0.4-1MeV and 1-1.5MeV energy groups	167
FIGURE 5.16	M.O.R.S.E. results for iron in the 1.5-2MeV and 2-2.5MeV energy group	168
FIGURE 5.17	M.O.R.S.E. results for iron in the 2.5-3.0MeV Group	169
FIGURE 6.1	Comparison of Day's [9] results with predicted curve for the gamma ray production cross-section due to excitation of the 0.845MeV level in iron, with 2.6MeV neutrons	179
FIGURE 6.2	Comparison of Al-Shalabi's [40] results with the predicted curve for the differential gamma ray production cross-section at 90 degrees scattering angle, for the excitation of the 0.845MeV level in iron	181
FIGURE 6.3	A possible application of Trail and Raboy [67] detector to present work	184

CHAPTER 1

INTRODUCTION

1.1 INTRODUCTION

Nuclear fusion involves the fusing together of light nuclei to form heavier nuclei in a manner such that the potential energy of the product nuclei are lower than that for the lighter nuclei. The "lost" potential energy of the product nucleus, appears in the form of kinetic energy of the product particle and this may be used to create heat energy and thus electrical energy via a turbine.

Although it is possible to fuse together a number of light nuclei, the reactions of greatest interest are:-

(i) $${}^{2}_{1}H + {}^{2}_{1}H \longrightarrow {}^{3}_{1}H + P + 4.0\ MeV$$

$$\searrow\ {}^{3}_{2}He + n + 3.2\ MeV$$

(ii) $${}^{2}_{1}H + {}^{3}_{1}H \longrightarrow {}^{4}_{2}He + n + 17.6\ MeV$$

Most present fusion research is concerned with thermonuclear fusion in which the nuclei are heated to very high temperatures ($10^{8}K$) to form a plasma and the resulting thermal energy used to fuse the nuclei together. Methods of heating the plasma differ, but most success has been achieved by the Tokamak design K. Sako et al. [1], F.H. Fenny [2], S.E. Hunt [3].

There are four current Tokamaks either under construction or operating and these are TFTR (USA), JT-60 (Japan), T15 (USSR) and JET (Joint European). All these designs have the same principle in that, the plasma is contained in a torus and is considered to be the secondary coil of a large transformer. Large electrical

currents are supplied via the primary coil to heat the plasma using ohmic heating. The plasma is contained using magnetic fields which may be used for further heating, via the pinch effect. To obtain temperatures necessary for fusion, further heating is provided by neutral particle injection and radio frequency heating. The problem of containment of the plasma is one which requires the latest technology and it is hoped that the four experimental reactors mentioned earlier, will answer many of the questions concerning this.

It has been shown by Lawson[3] that the condition for a self-sustaining fusion reactor is:

$$n\ \tau > 10^{-14}\ cm^{-3}\ sec.$$

where n = plasma density

τ = confinement time

Because of this condition, the $D(T,n)\alpha$ is of most interest for the future, since it has the highest reaction rate and hence imposes least stringent conditions for self-sustaining fusion. Deuterium is plentiful, with an abundance of 1.5% and can be obtained from natural water. Tritium however is not and must be manufactured. The latter problem must be considered for design of working fusion reactors.

Most conceptual fusion reactor designs conform in general to a central core surrounded by a number of blanket materials as shown in Figure 1.1.

The vacuum is essential to separate the 10^8K plasma from the structural materials such as iron and steel.

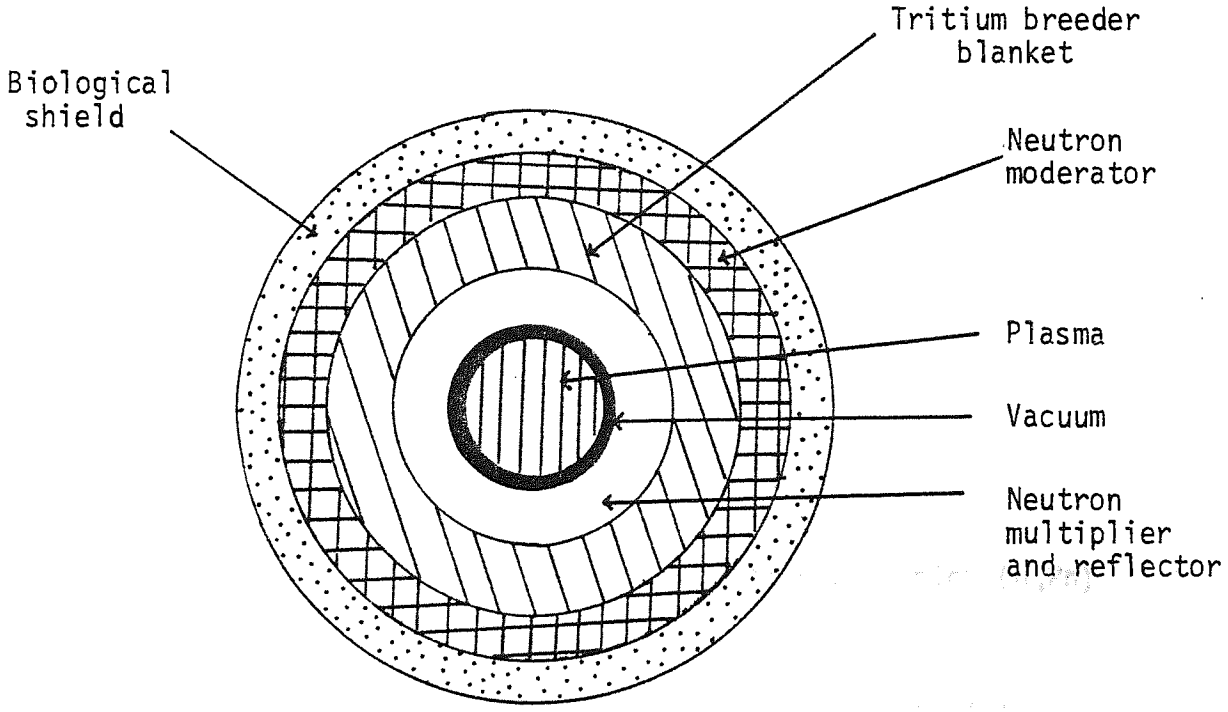

FIGURE 1.1: Future conceptual design for a working fusion reactor

The Breeder blanket will be used to manufacture tritium using the 14 MeV neutrons from the fusion reaction. The most popularly considered breeder material is natural lithium which gives tritium in the following reactions:-

$$^{6}_{3}Li + n \longrightarrow {}^{3}_{1}H + {}^{4}_{2}He + 4.8MeV$$

$$^{7}_{3}Li + n \longrightarrow {}^{3}_{1}H + {}^{4}_{2}He + {}^{1}_{0}n - 2.5MeV$$

Lithium seven is the most important isotope of the above since it has an abundance of 92.58%.

To enhance tritium breeding it is hoped to use (n,2n) reactions in the neutron multiplier blanket. The materials for such a blanket are still under speculation but Nb, Be and Lead are of prime interest. Lead has a particularly high (n,2n) reaction and low threshold since the binding energy of the nucleus is low. However, little information concerning the interaction of 14 MeV neutrons, especially inelastically scattered neutrons is available.

The moderator and reflector will be made from graphite, since this is readily available and has proved to be efficient in moderating 14 MeV fusion neutrons in fission reactors. The main purpose of this blanket, is to convert the kinetic energy of the fusion neutrons, into heat energy and to produce a thermalised neutron spectrum. Reflected neutrons will be returned to the breeder blanket for breeding of tritium.

Biological shielding must have a high thermal neutron and gamma ray absorption. For this reason likely materials to be present in such a shield are Nb, B, Pb and concrete.

It is clear that for accurate knowledge of gamma ray production, neutron reactions, heat degradation, structural (iron and steel) and shield calculations, it is necessary to have reliable data concerning the $(n,n'\gamma)$ reactions for 14MeV neutrons. Furthermore, since blanket materials are relatively thick, the problem of multiple neutron scattering is important and little data is available concerning this.

1.2 AIM OF THE PROJECT

This work is concentrated on gamma ray production cross-sections in $^{7}_{3}Li$, Natural Lead and some work with iron. The $T(d,n)\alpha$ reaction has been used to provide 14MeV neutrons for experimental work and in this energy range the main gamma producing reactions are $(n,n'\gamma)$, with (n,γ) cross-section negligible.

The differential gamma ray production cross-section is a measure of the probability that gamma radiation of energy E, will be scattered into solid angle $\Delta\Omega$, at an angle θ to the incident neutron beam. Much of the work here is concerned with measuring this quantity experimentally, both at different angles θ and for various sample thicknesses.

Of the experimental techniques available, the most significant for angular neutron scattering measurements, is the associated particle time of flight method. This method uses the alpha particle of the $T(d,n)\alpha$ reaction as a reference in time. The time difference between scattered neutrons of velocity v, and gamma rays velocity c, (velocity of light) over a flight path, may then be distinguished using fast electronics in a manner similar to that employed by Cox[4], M.L. Janicki

et al.[5] and Clarke et al.[6]

Time of flight discrimination may then be used to gate only gamma rays such as in the work by Al-Shalabi et al.[7] The advantage of this method is that closed geometry may be used and the neutron background considerably reduced. Furthermore, the problem of a forward peaked elastic neutron spectrum, interfering with the gamma ray spectrum, as outlined by Day[4], is eliminated, since only random coincidence neutrons enter the spectra. These are easily removed by subtracting at regular intervals.

The cross-section is normally defined in terms of barns per nucleus and may be measured so for very thin samples, ideally a mono-layer. However, in the practical situation such as a breeder blanket or indeed measuring cross-sections, the sample sizes are often greater than 0.2 mean free paths (Day s criterion[9]) for which multiple scattering effects become important. The effect of multiple scattering on gamma ray production cross-section is to increase it. This is due to the extra gamma rays produced by multiple neutron collisions for a constant neutron flux. The situation is made even more complicated by (n,2n) reactions and the slowing down of neutrons through the sample.

Analytical methods of treating multiple scattering problems can often become very complicated and many simplifications have to be made. Monte Carlo methods are probably the best way of treating this problem and are the most widely used in reactor core and blanket flux calculations. However, even this method requires accurate microscopic cross-section.

The main aim of the project is to measure experimentally, the effects of multiple scattering on the aforementioned possible fusion reactor materials. It is hoped that these results will be of use in blanket calculations, as a check for theoretical calculations and as a source of data for future experimentalists. The results have been analysed using a Monte Carlo programme called M.O.R.S.E. code [10] on the central computer at Harwell A.E.R.E. A large part of the research was concentrated on this, with the aim that, the experimental and Monte Carlo results compliment each other.

CHAPTER 2

GENERAL CONSIDERATIONS

2.1 Kinematics of the T(d,n)He^4 Reaction

In the present application, 14MeV neutrons were produced using the reaction:

$$ {}^{2}_{1}H + {}^{3}_{1}H \longrightarrow {}^{4}_{2}He + n + 17.6MeV $$

The alpha particles were detected at 90° to the deuteron beam nominally 140KeV.

In general, in the laboratory frame of reference the situation may be described by the diagram:

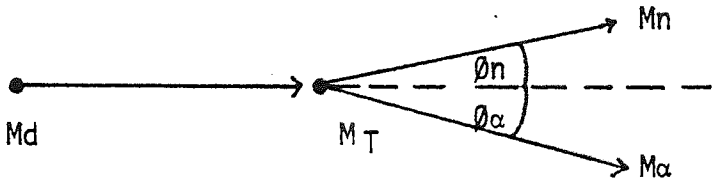

Md = mass of deuteron
M_T = mass of tritium
Mα = mass of alpha particle
Mn = mass of neutron

Benviste and Zenger[11] have shown that the equation relating the angle of emission of the neutron Øn and that of the alpha particle Øα, with respect to the incident deuteron beam, is given by:

$$ \tan Ø\alpha = \frac{-\frac{1}{2}\sin 2Ø + \sin Øn \sqrt{\frac{1}{\gamma^2} - \sin^2 Øn}}{-\sin^2 Øn + \cos Øn \sqrt{\frac{1}{\gamma^2} - \sin^2 Øn} - \frac{M\alpha}{Mn}} \quad \ldots\ldots 1.1 $$

where the parameter γ is defined as, the ratio of the velocity of the centre of mass frame, relative to the lab frame, to the velocity of the neutron in the centre of mass frame and is given by:

$$\frac{1}{\gamma^2} = \frac{M\alpha}{Mn} \cdot \frac{Md + M_T}{Md} \left(\frac{M_T}{Md + M_T} + \frac{Q}{Eo}\right) \quad \ldots\ldots\ldots\ldots 1.2$$

Eo = Incident deuteron energy.

Q = Q-value for the reaction given by:

$$Q = (M_T + Md - Mn - M\alpha)C^2$$

Equations 1. and 2. show that for a fixed $\emptyset\alpha$, the neutron angle $\emptyset n$, will depend upon the incident deuteron energy Eo. The "thick" tritium target used throughout the project, completely stopped all deuterons incident upon it. As a result deuterons of all energies from 0 to 140 KeV were producing neutrons. Furthermore, the aperture of the alpha particle detector defined $\emptyset\alpha$ to a possible $\pm 3.5^{\circ}$ half angle in the horizontal plane. The result, was to give an associated possible range of neutron angles $\emptyset n$, which were calculated from equation 1. and illustrated in Figure 2.1.

The variation in deuteron energy in the thick target, will produce a variation in the neutron yield, which is usually referred to as the neutron yield line shape. Calculation of this may be carried out using the proportionality:

$$N(\emptyset, Eo) \propto \frac{d\sigma(E)}{dW^1} \cdot \frac{dW^1}{dW} \Big/ \frac{dE}{dx} \quad \ldots\ldots\ldots\ldots\ldots\ldots 1.3$$

where:

$N(\emptyset, Eo)$ = Neutron yield

$\frac{d\sigma}{dW^1}$ = Differential cross-section for the T(dn)α reaction in the centre of mass frame

$\frac{dW^1}{dW}$ = Anisotropy factor, which is the ratio of the elemental solid angle in the centre of mass system to that in the laboratory system

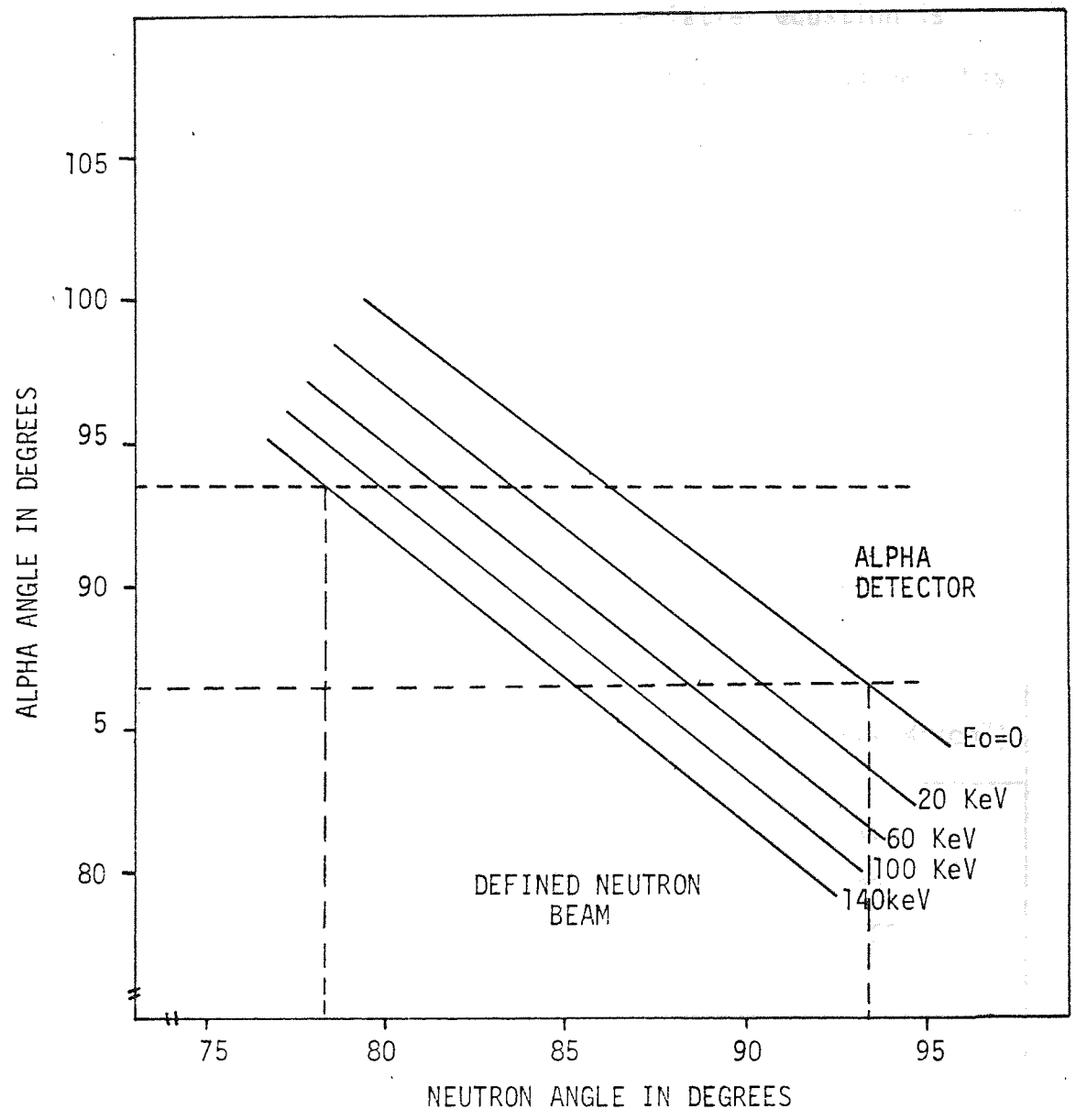

FIGURE 2.1 NEUTRON-ALPHA ANGULAR RELATIONSHIP FOR A 7° ALPHA APERTURE

$\frac{dE}{dx}$ = Rate of energy loss of deuterons of energy E in the T_i T target.

The constant of proportionality in the latter equation is $4\pi n_t$.* However, as we are only interested in the line shape, this constant is set to unity. Furthermore, Allenby [12] has shown that $\frac{dW^1}{dW}$ for deuteron energies considered approximates to unity, with an accuracy of ±1% over the small angular and deuteron energy ranges given here. The values of $d\sigma/dW^1$ were obtained from data of Conner et al. [13] and aregiven in the following table with the values of dE/dx taken from Benviste and Zenger[11].

TABLE 2.1 Table from Benviste and Zenger

E (KeV)	$\frac{d\sigma}{dW^1}$ (barns/st)	$\frac{dE}{dx}$ (KeV/Mg/cm^2)
20	4.744×10^{-3}	140
40	0.05716	220
60	0.162	260
80	0.304	282
100	0.3955	308
110	0.405	315
120	0.403	323
140	0.3725	333

The latter values were used in equation 1.3 to find the shape of

*(n_t = no. of tritium nuclei per unit vol.)

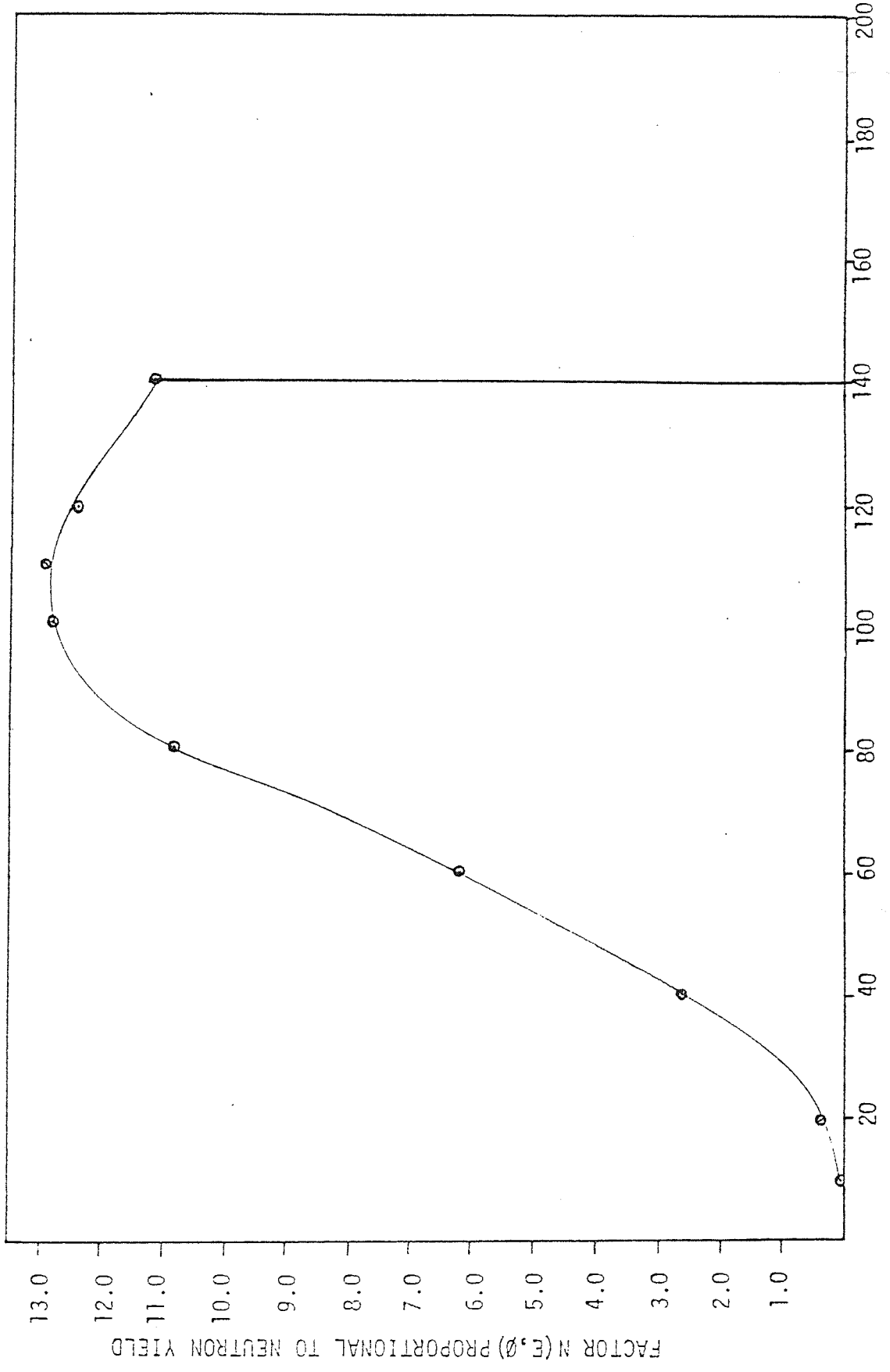

FIGURE 2.2 NEUTRON YIELD SHAPE

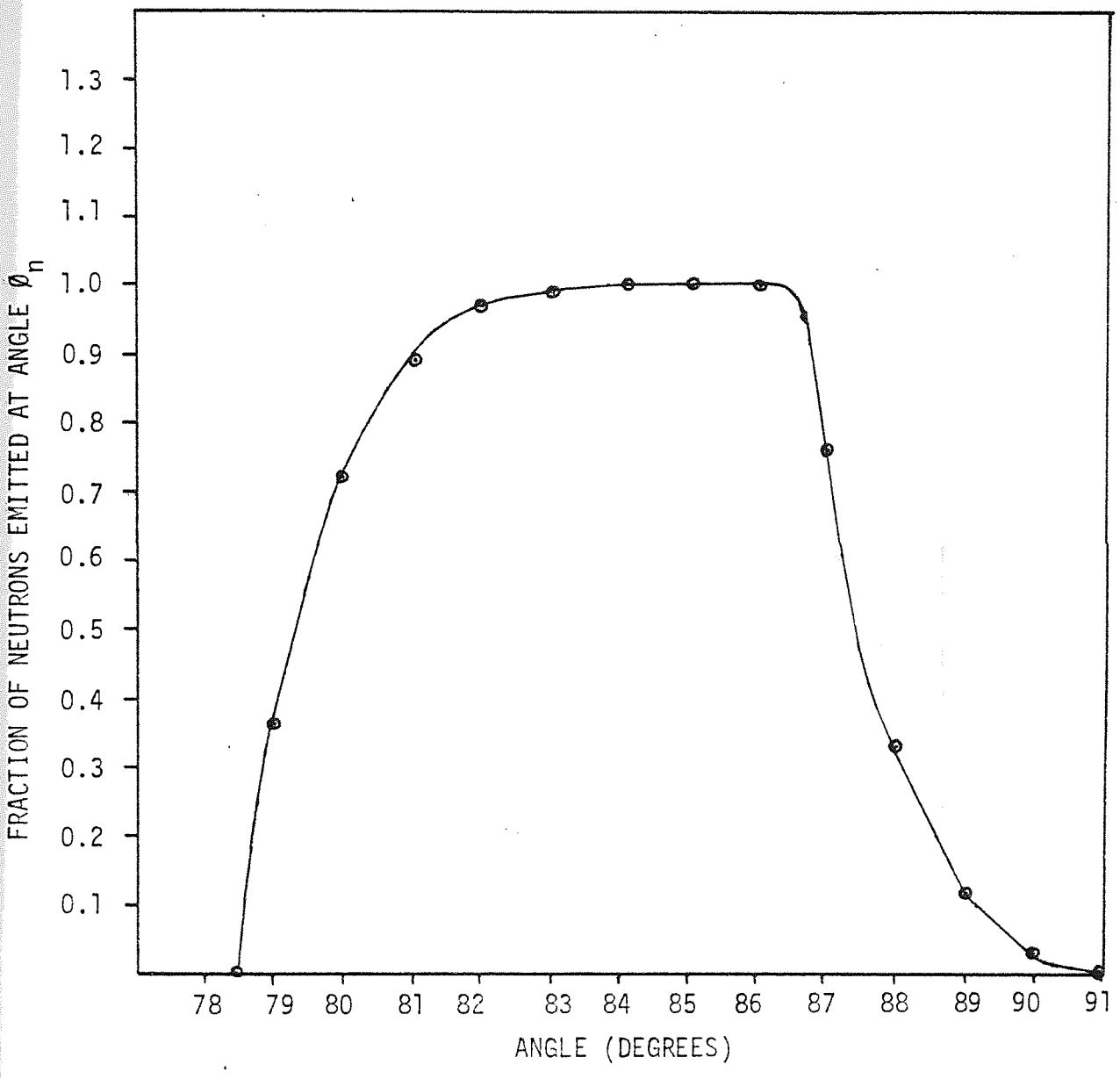

FIGURE 2.3: NEUTRON BEAM PROFILE

TABLE 2.2: TABULATION FOR NEUTRON BEAM PROFILE

DEUTERON ENERGY(KeV)		$\int_{E_1}^{E_2} N(E,\phi)dE$	F	ϕ_n (DEG.)
LOWER LIMIT E_1	UPPER LIMIT E_2			
140	140	0	0	78.5
110	140	363.4	0.36	79.0
80	140	734.5	0.72	80.0
60	140	902.2	0.89	81.0
40	140	987.7	0.97	82.0
20	140	1014.6	0.999	83.0
15	140	1015.7	1.0	84.0
5	140	1016	1.0	85.0
0	140	1016	1.0	86.0
10	115	716.6	0.71	87.0
10	85	337.8	0.33	88.0
10	60	113.8	0.11	89.0
10	40	28.4	0.03	90.0
10	20	1.5	0.001	91.0

the neutron yield curve which is shown in Figure 2.2.

From the neutron yield curve, the neutron beam profile could be calculated. This factor is defined by:

$$F = \frac{\int_{E_1}^{E_2} N(\emptyset, Eo)\, dE}{A_T}$$

where E_2 = upper limit for deutron energy

E_1 = lower limit for deutron energy $E_1 < E_2$

A_T = the total neutron output defined by:

$$A_T = \int_{o}^{Eo=140KeV} N(\emptyset, Eo)\, dE$$

For A_T, 5KeV intervals were taken using the trapezium rule to estimate the total area under the neutron line shape curve. The value attained was $A_T = 1016$. Table 2.2 illustrates the full calculation of the neutron beam profile which is shown in Figure 2.3.

The full width at half maximum is shown to be 7.2° and it is centred at 83.5° to the incident deuteron beam. This angle was chosen as the 0° neutron scattering angle in the practical arrangement. The following diagram shows the angular relationships in the laboratory frame:

Figure 2.4: Angular relationships in the lab. frame

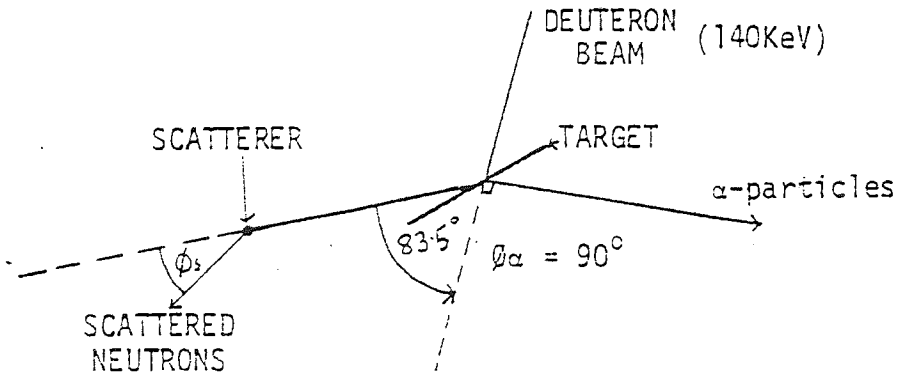

2.2 Interaction of gamma rays in matter

When photons interact with matter, there are three main absorptive processes to take into account:

1. Photo electric effect
2. Pair production
3. Compton scattering

Each of the above processes will dominate in a specific photon energy region, which will depend upon the atomic number of the element in a manner summarised in the following table.

TABLE 2.3 Interaction of gamma rays in matter

	PHOTO-ELECTRIC EFFECT	COMPTON SCATTERING	PAIR PRODUCTION
LIGHT ELEMENTS	BELOW 50 KeV	50KeV-15MeV	ABOVE 15MeV
HEAVY ELEMENTS	BELOW 0.5 MeV	0.5MeV-5MeV	ABOVE 5MeV

2.2.1 Photo-electric effect

Absorption takes place when an incident photon gives all its energy to eject an electron from the atom. The energy of the emitted electron is given by:

$$E = h\nu - I$$

h = Planck's constant
ν = Frequency of incident radiation
I = Binding energy of electron

The following classical representation shows how high and low energy photons may give up all their energy to remove electrons from atomic shells:

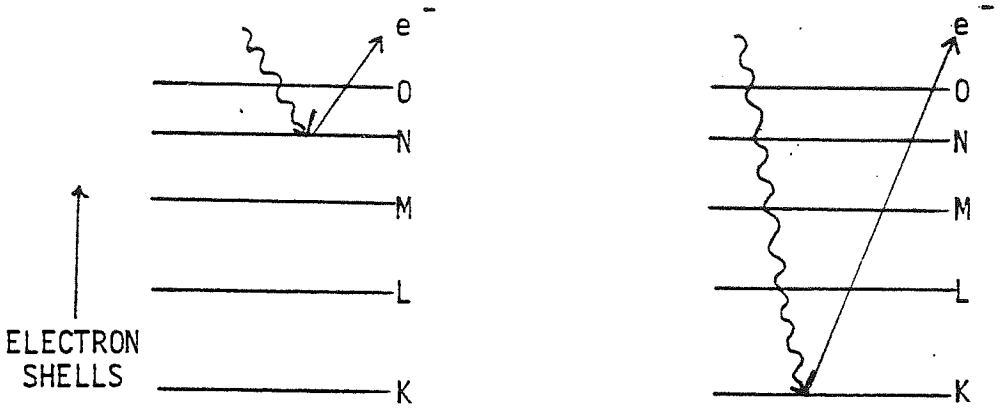

(i) U.V. PHOTONS INCIDENT

(ii) X-RAY PHOTONS INCIDENT

The diagrams show that, low energy photons lose energy by removing the loosely bound outer electrons and as the energy of the incident photon is increased, more tightly bound inner electrons can be removed until finally the K-shell electron is removed. The effect of this on the mass absorption coefficient versus energy curve, is a series of discontinuities corresponding to the K L M etc. absorption edges. Typical curves for the region in which photoelectric effect predominates are illustrates in Figure 2.5 taken from Price et al.[14]

For photon energies above the K-shell absorption edge, 80% of ionising events are due to K-electron emission. This is particularly important in gamma ray absorption where the cross-section for K-shell ionisation per atom is calculated by Heitler[15]:

$$K^{\sigma}\ \text{P.E.} \quad = \quad \frac{8\pi r_o^2}{3} \ \frac{Z^5}{137^4} \ 4\sqrt{2}\left(\frac{mc^2}{h\nu}\right)^{\frac{7}{2}}$$

r_o = classical radius of electron

mc^2 = 0.51MeV (rest energy of electron)

The latter simplifies to:

$$K^{\sigma}\ P.E. = 1 \times 10^{-9}\ Z^5\ Eo^{-\frac{7}{2}}$$

Eo = Incident photon energy

The formula illustrates the very strong dependence of the photo-electric cross-section on the atomic number Z of the absorbing element. More elaborate formulae have been reported by Allison [16], Sauter[17] and Stobbel[18], but the basic Z dependence still remains.

When the K-shell electron has been removed by a gamma ray photon, secondary fluorescent radiation will result from subsequent transitions of L and M electrons to the K-shell, giving the characteristic Kα and Kβ radiation. These photons may in turn give rise to Auger electrons by outer electron reabsorption. The cross-section for the production of fluorescent K radiation is given by:

$$\Phi_K = 1 + 1.12 \times 10^6\ Z^{-4}$$

However, this radiation is always less energetic than the initial gamma ray producing it and it is readily stopped by either shielding or electronic discrimination techniques.

2.2.2 Pair Production

Above 1.02MeV, i.e. twice the rest mass of the electron $2mc^2$, pair production may take place. The incident photon, in the presence of the nucleus, may create an electron-positron pair, with total energy equal to that of the photon. The unstable positron very quickly annihilates with a free electron in the material, to produce two 0.511MeV photons. There is also a probability of producing only one 0.511MeV photon, however, the probability for this is low and only takes place with bound electrons. The explanation of the mechanism of pair production is very complicated. One simplified picture is the Dirac electron hole image. To explain this theory, consider the following diagram:

c = velocity of light

m = mass of electron

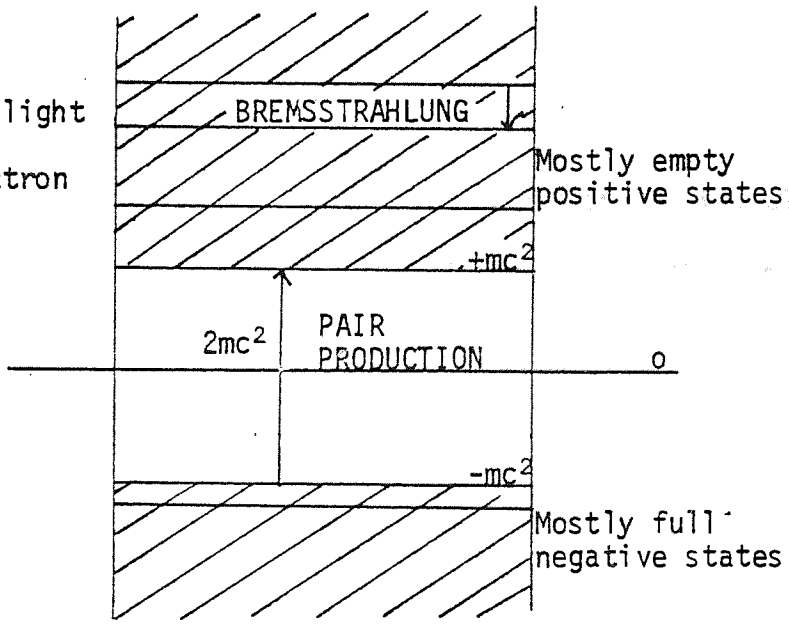

The whole of space above the threshold of mc^2 is considered to be a continuum of positive electron states. The negative solution in Dirac's theory is shown as constituting a similar high density of filled negative electron states. The only way an electron can be observed is if it crosses the energy gap $2mc^2$ to become a free electron in one of the empty positive electron states. The resulting hole in the negative energy region is then

observed as the positron in pair production. For the intermediate energy region $2mc^2 << h\nu << 137mc^2 Z^{-\frac{1}{3}}$, the cross-section for pair production in the field of the nucleus is given by:

$$\sigma_{pp} = Z^2\left(\frac{e^2}{4\pi\varepsilon_0 mc^2}\right)\left[\left(\frac{28}{9}\right) \log e\left(\frac{2h\nu}{mc^2}\right) - \frac{218}{27}\right]$$

The symbols are as before except:

e = charge on the electron

ε_0 = permitivity of free space.

The formula shows the general Z dependence and that the cross-section increases rapidly above threshold. This increase falls off at very high gamma ray energies and a constant value is reached.

It has been shown by Perrin[19] that pair production will also take place in the presence of orbital electrons. However, the threshold for this process is 2.04MeV and has a smaller cross-section than the above, in the ratio $^1/_Z$.

2.2.3 Scattering of gamma rays

The most important scattering process, for present purposes is Compton scattering. The incident photon collides with a free electron in the material to lose some of its energy, by conservation of momentum as shown below:

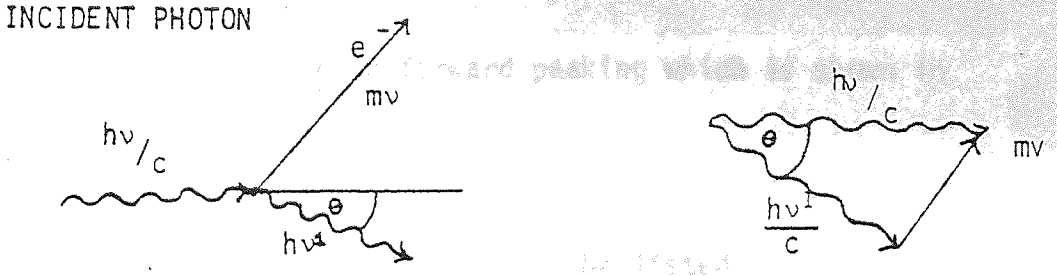

(i) Collision process (ii) Vectorial representation

m = mass of electron

v = velocity of electron

$h\nu^1$ = energy of scattered photon

It can be shown from the vectorial representation, and the conservation of energy and momentum laws, that the change in wavelength of the incident photon is given by:

$$\Delta\lambda = \lambda_o (1 - \cos\theta) \qquad (2.1)$$

λ_o = h/mc known as the compton wavelength.

Equation (2.1) shows that maximum change in energy of the incident photon occurs for 180° backward scattering and no change in energy for forward 0° scattering.

The Compton differential cross-section per electron $C(\theta)d\Omega$ is proportional to the probability that an unpolarised photon will be scattered through an angle θ into solid angle $d\Omega$. It is given by the Klein Nishina formula:

$$C(\theta)d\Omega = r_o^2 \, d\Omega \left(\frac{1 + \cos^2\theta}{2}\right) \frac{1}{[1 + \gamma_o(1-\cos\theta)]^2}$$

$$\times \quad \left\{1 + \frac{\gamma_o^2 (1 - \cos\theta)^2}{(1 + \cos^2\theta)\ (1 + \gamma_o(1 - \cos\theta))}\right\}$$

$\gamma_o = h\nu/mc^2$ for the incident photon

r_o = classical radius of electron.

The formula gives rise to forward peaking which is shown in Figure 2.6.

Other types of photon scattering may be listed:

(i) Rayleigh scattering

(ii) Thompson scattering

(iii) Nuclear resonance scattering

Rayleigh scattering involves the interaction of the incident photon with bound electrons in matter. It is mainly observable at low photon energies below 0.5MeV. However, photo-electric effect predominates in this region. Furthermore, since collision occurs with a bound electron, then recoil of the atom is very small and scattering is essentially elastic. As a result, this type of scattering is often referred to as coherent scattering and interference effects may be observed.

Thompson scattering, also coherent, has a negligible cross-section, compared with Rayleigh scattering and Compton scattering and involves scattering between the incident photon and the nucleus.

Nuclear resonance scattering is the analogue of atomic fluorescence and has a very low probability for all practical purposes.

Figure 2.7, taken from White[20] illustrates the range over which the main absorptive processes predominate, including the effects of coherent and incoherent (Compton) scattering.

Attenuation of gamma rays in matter and the Total Mass Attenuation Coefficient

For a narrow beam of photons with an incident flux Io, incident on a sample of thickness x, the equation relating the attenuated flux to the former is:

$$I = I_0 e^{-\mu x}$$

μ = Total attenuation coefficient in units m^{-1}

In all reports tabulating the attenuation coefficient use is made of the total mass attenuation coefficient which is given by (μ/ρ) where ρ is the density of the attenuating sample. If the sample is a compound then the following relation is used:

$$(\mu/\rho) = \sum_i W_i \, (\mu/\rho)_i$$

W_i = Weighted fraction of the i^{th} element in the compound

(μ/ρ) = Total mass attenuation coefficient for the i^{th} element

The mass attenuation coefficient has been calculated by various workers including White[20], Allison[16], Victoreen[21] and Grodstein[22]. All their calculations were based upon theory and empirical data using the basic assumption:

$$(\mu/\rho) = (\tau/\rho) + (\chi/\rho) + (\sigma/\rho)$$

(τ/ρ) = Total mass attenuation coefficient for photo-electric effect
(χ/ρ) = " " " " " pair production
(σ/ρ) = " " " " " Compton scattering
calculated from the Klein Nishina formula.

The summation of these three effects is illustrated in Figure 2.8

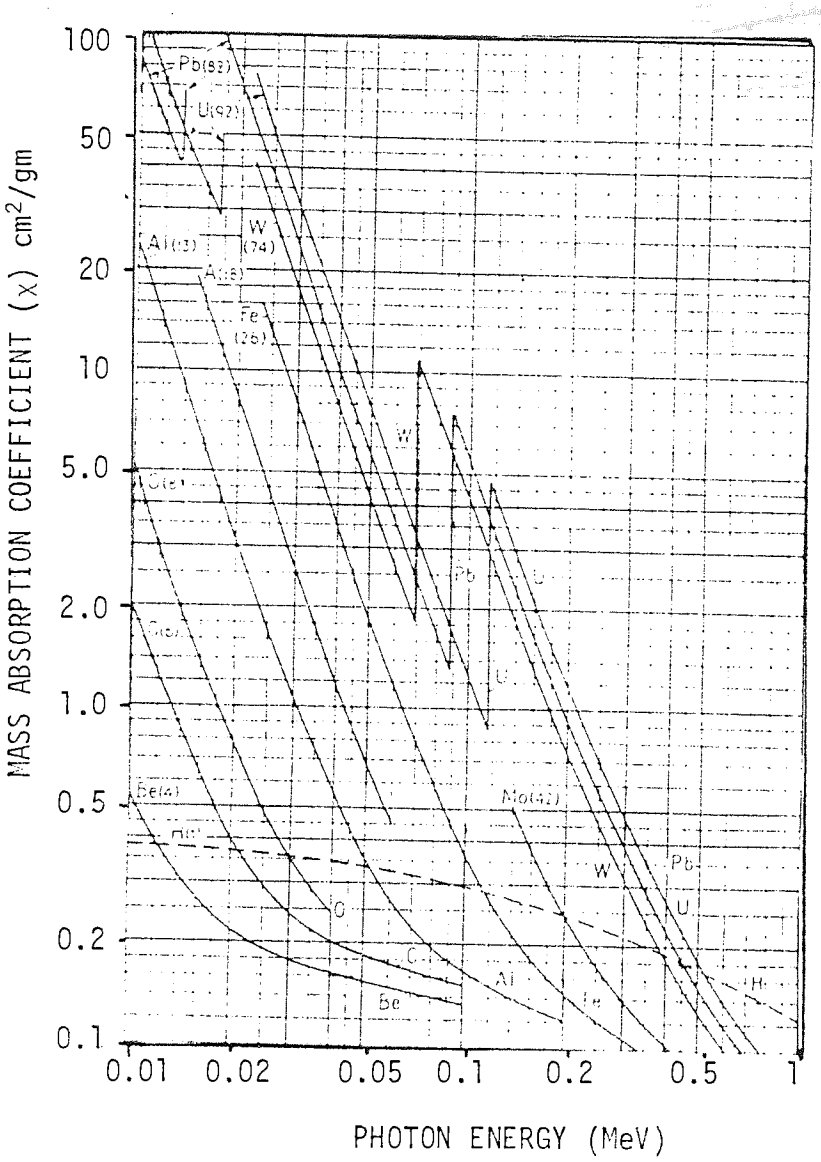

FIGURE 2.5: MASS ABSORPTION VARIATION WITH ENERGY OF PHOTONS (PRICE ET AL.[14])

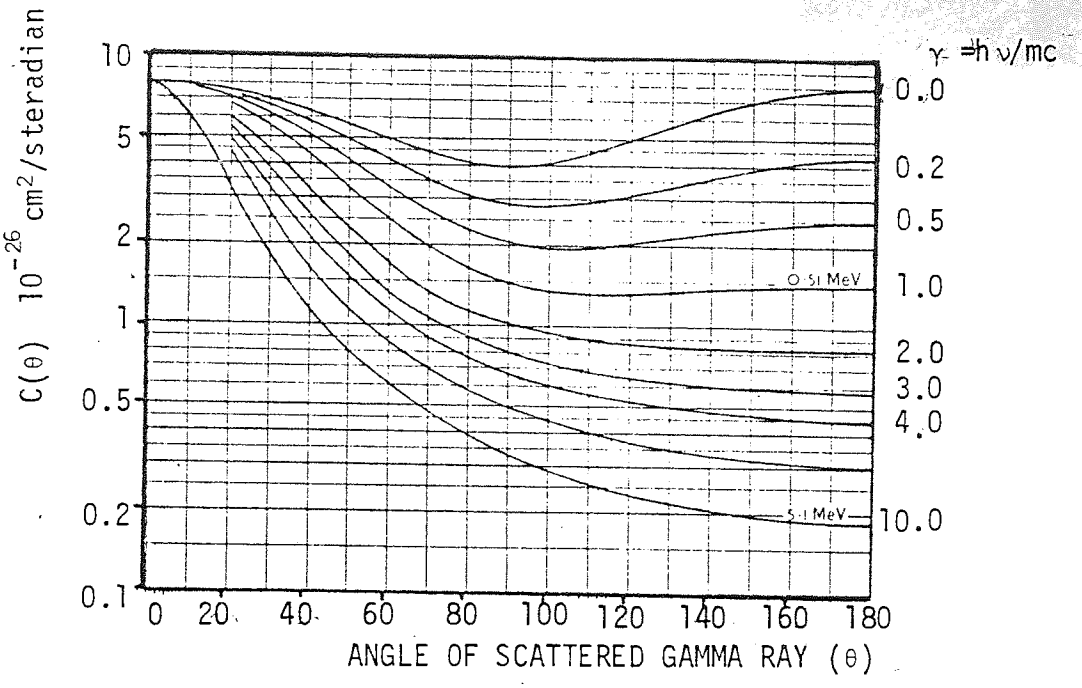

FIGURE 2.6 COMPTON DIFFERENTIAL SCATTERING CROSS-SECTION PER ELECTRON AS A FUNCTION OF ENERGY

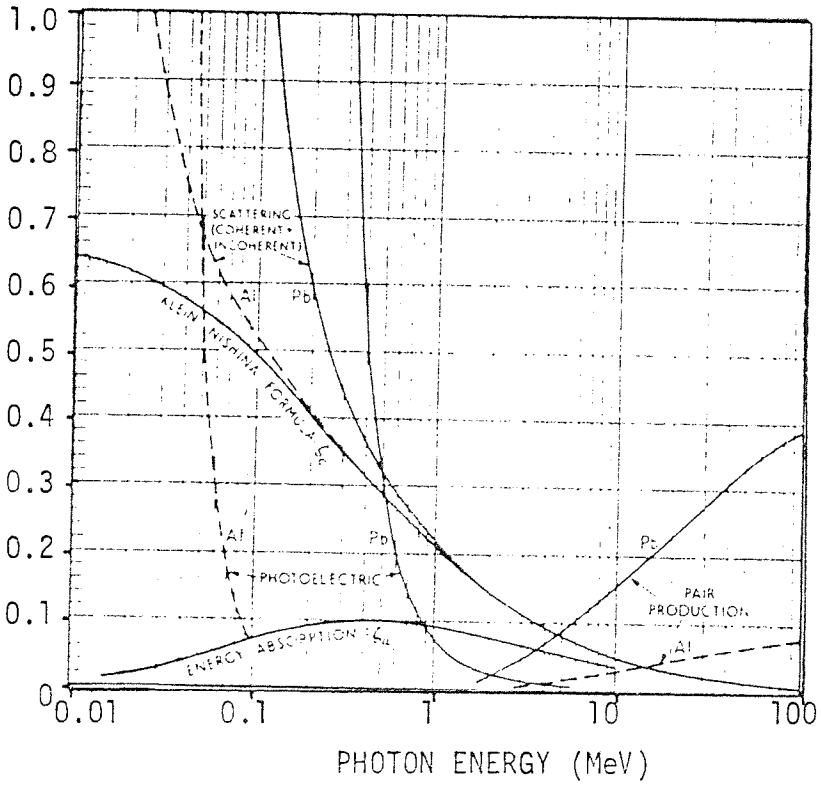

FIGURE 2.7: SCATTERING ABSORPTION CROSS-SECTION PER ELECTRON FOR LIGHT AND HEAVY ELEMENTS AS A FUNCTION OF PHOTON ENERGY (WHITE (20))

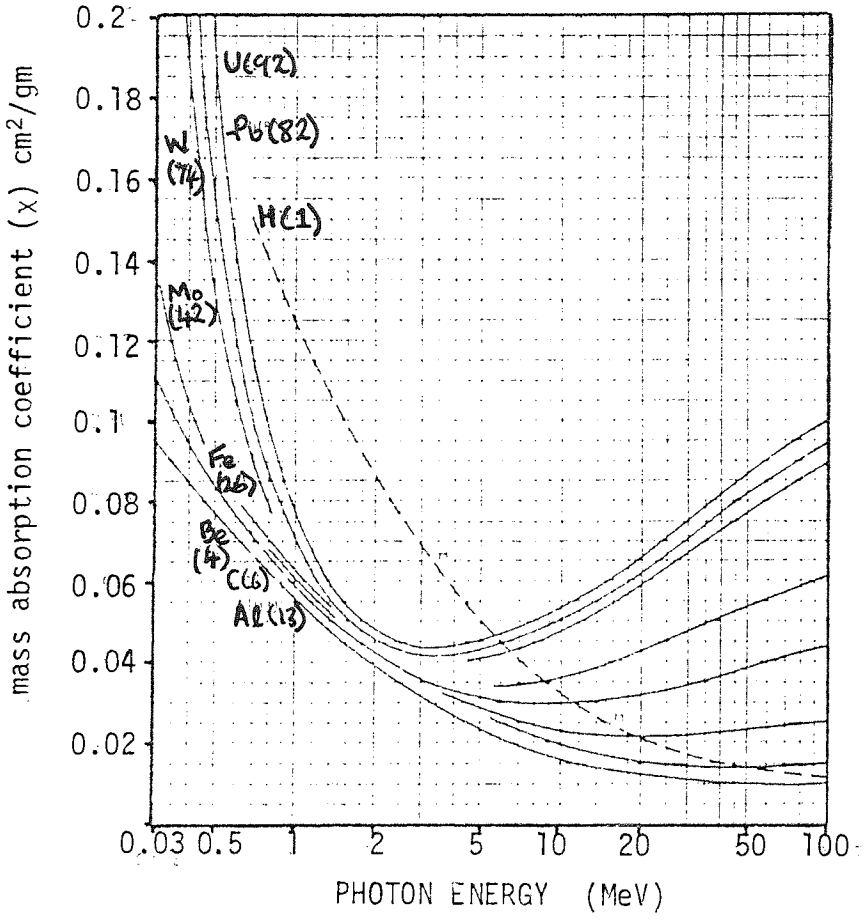

FIGURE 2.8: NARROW BEAM MASS ABSORPTION COEFFICIENTS AS A FUNCTION OF ENERGY FOR A NUMBER OF DIFFERENTIAL ELEMENTS (WHITE (20))

CHAPTER 3

DESCRIPTION OF APPARATUS

3.1 Production of Neutrons

The neutrons were produced using the T(d,n)α reaction. In this process, deuterons were accelerated to 140keV, using a S.A.M.E.S. type J accelerator and made to impinge onto a titanium tritide target. The deuterons were supplied by a 100MHz radio frequency ion source and were extracted using a 0 to + 6kV variable potential, into a beam tube approximately 6m in length. The beam was focussed onto the target by a + 45kV focussing electrode, at the machine end, a quadrupole focussing arrangement designed and described in detail by Baynam[23] and finally a pair of deflector plates at the target end (see Figure 3.1).

The TiT target assembly was insulated from the beam tube by an araldite flange and hence a target current could be measured via a large resistor and ammeter to earth (typically 3μA). The large resistor was chosen to raise the potential of the target to +200 volts, so that any electrons energetically removed from the target by deuterons, were suppressed from back-streaming towards the accelerator. The deuteron beam was defined by a 2 x 30mm copper aperture which was also insulated from the main beam tube. The target itself was rotated by a small electric motor at 60 r.p.m. The titanium tritide layer was 2000nm thick and deposited on a thin copper plate. The target was cooled by circulating water, the copper plate acting as a heat exchanger. At 90° to the beam tube the target assembly provides for a α-detector at 9cm from the target as shown in Figure 3.2.

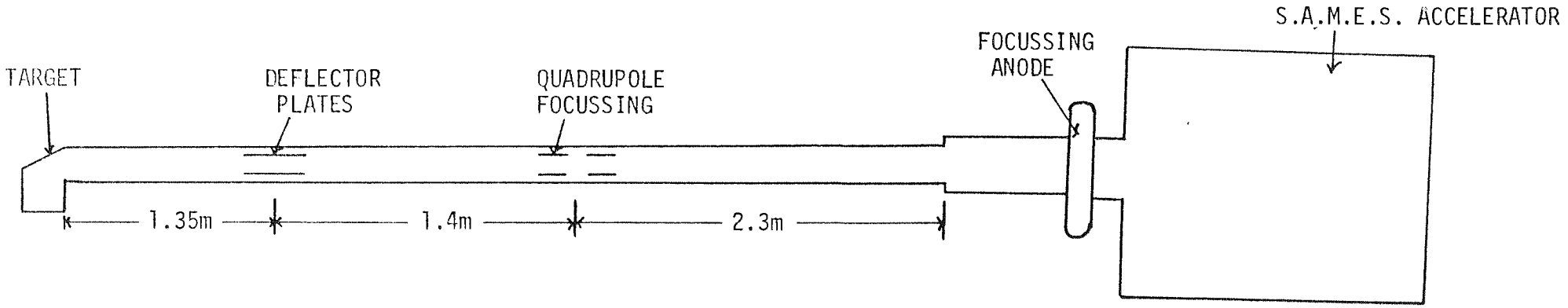

FIGURE 3.1: SCHEMATIC DIAGRAM OF ACCELERATOR

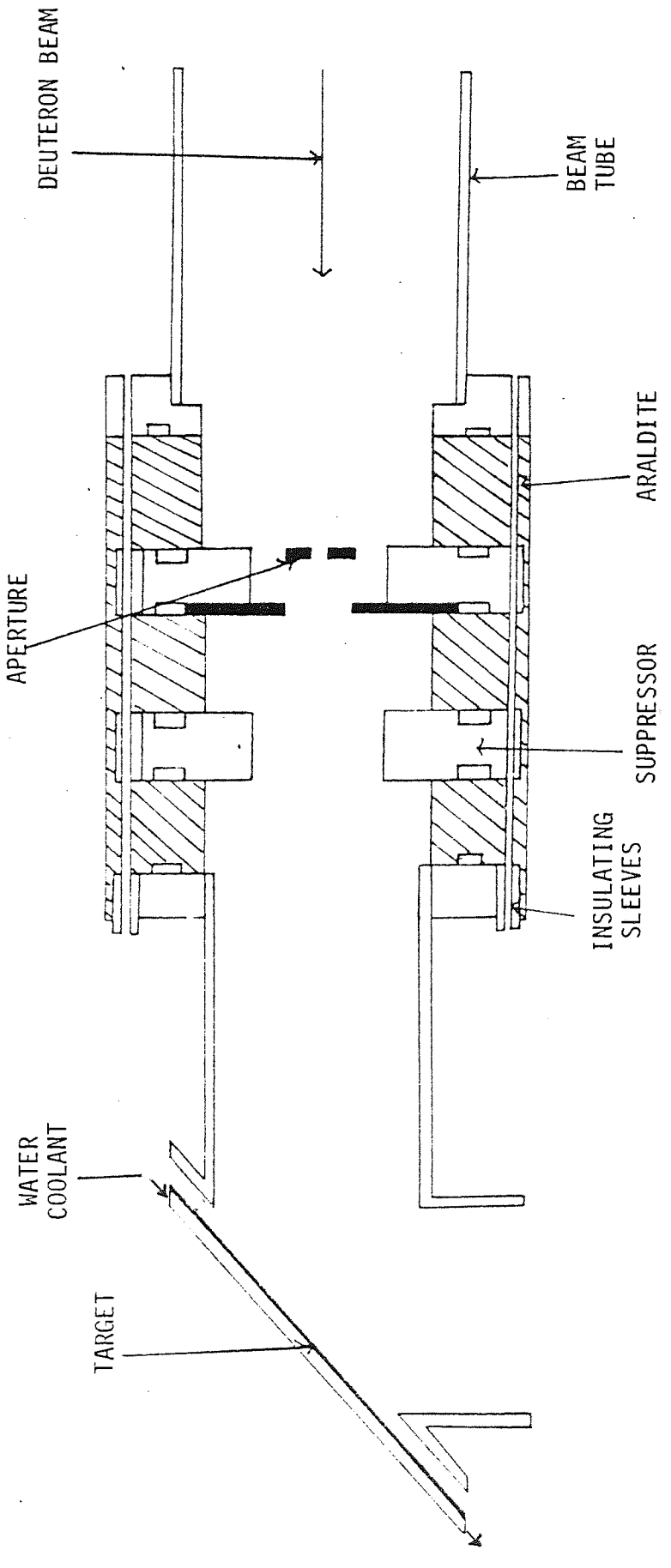

FIGURE 3.2: TARGET ASSEMBLY

3.2 The Alpha Detector

In choosing an alpha detector for present applications, certain basic properties were considered important. Firstly, the detector must have a high alpa particle detection efficiency, for the energy range under consideration. Secondly, a low neutron and gamma ray response was preferable, to minimise background contributions. Finally, a fast response time for nanosecond timing was essential.

Of the detectors available, two were considered to closely fulfil the above requirements. These were the plastic scintillator detectors and the solid state detectors. Both were considered and a choice was made based upon the relative characteristics of each, discussed below.

In the process of manufacture of Si(Li) detectors, Li is drifted under the influence of heat and an electric field, into a p-type silicon extrinsic semi-conductor. The result is a depletion or detection region in a PN junction which is of relatively small volume. For this reason, the response of the detector to neutrons and gamma rays is low. Furthermore, the fast response time ($\approx$1ns) is also ensured with a small detection region. The alpha particles would be detected with 100% efficiency, as they are doubly charged and heavily ionised. However, the Si(Li) detector is susceptible to radiation damage. Using the data from Ref.(24) a 3.5MeV alpha source of 10^7 particles per second at 90mm from the detector, results in a lifetime of only 280 hours, before the junction needs redrifting.

For the latter reason, an NE102A plastic scintillator was used in present work. The scintillator was comprised of low Z elements and was readily available in thin sheets, so that the neutron gamma response was low. The decay time of the scintillator was ≈2ns which was sufficient for present purposes. The main advantage arose from its resistance to radiation damage. According to ref. (25) for a 3.5MeV alpha source, under the conditions quoted above for the Si(Li) detector, the expected lifetime for which the efficiency falls by half its original value is 6×10^4hours.

3.2.1 Design of the alpha detector

The range of 3.5MeV alpha particles in NE102A plastic scintillator, is quoted by the manufacturers as 0.025mm. In the present application, the chosen thickness was 0.5mm to ensure 100% efficiency. To avoid housing the detector inside the vacuum chamber, the scintillator was coupled to a 56 AVP photmultiplier tube via an air tight perspex light pipe, similar to that of O'Neill[26].

It was also necessary to shield the detector from both, scattered deuterons at 90° to the incident beam and β radiation from the build up of activity of the target. The main source of activity arose from beta particles, emitted in the decay of tritium with a half life of 12.3 years. The maximum kinetic energy of which was 18.6KeV and using Marion et al.[27] the range of such beta's in ^{26}Al was 0.002mm.

Deuterons of energy 200KeV have a range of 0.52mgcm^{-2} or 0.002mm in aluminium. The latter result being calculated by scaling proton data of Whaling[28] in which, protons of 100KeV were reported to have a range of 0.26mgcm^{-2} in aluminium.

The chosen thickness of aluminium foil was 0.0044mm which stopped all sources of radiation quoted above. The foil was placed over the face of and in contact with, the NE-102A scintillator. The range of 3.5MeV alpha particles in aluminium was taken from the data of Whaling[28] to be 0.017mm and hence easily passed through the foil.

The angle of acceptance of the alpha detector was defined by an aperture of dimensions 1.09 x 1.89cm. With the detector placed at 90°mm from the target, the latter gave rise to an angular spread in the neutron beam, defined by a half angle of 6° in the vertical plane and 3.5° in the horizontal plane.

3.3 The Gamma ray Detector

Of the detectors available for gamma ray spectroscopy, the two most widely used are the NaI(Tl) scintillation detector and the Ge(Li) solid state detector. The properties of these are discussed below.

Ge(Li) detectors are manufactured by diffusing Lithium into p-type germanium, at a temperature of about 50°C and an applied electric field. The resulting PN-junction is reverse biased using a typical operating voltage of 3kV. The detection region is the depletion region between the N- and P-type materials. Any ions formed here, by the incident radiation, are quickly swept away and the resulting signal collected across a large resistor (typically 10MΩ) and amplified. Because of this method of detection, the Ge(Li) detector exhibits a very high resolution and is the main advantage in using this detector. In general, for the 0.662MeV photopeak from the ^{137}Cs source, the resolution is 0.5% for a 30cm^3 detection volume. As is shown in the diagram from ref. (29) overleaf, the resolution of the Ge(Li) detector is about 20 times better than that for NaI(Tl). The main limitation in the energy resolution is due to the fluctuation in the production of ion pairs in the depletion region, resulting in the so-called Fano factor. The Fano factor is defined as the ratio of the number of ion pairs produced per MeV of radiation to the mean square of the variance in yield per MeV of radiation. The full width at half maximum is then given by

$$FWHM = 2.35\sqrt{\varepsilon E F} \qquad (\text{in MeV})$$

F = Fano factor
E = Energy of incident gamma ray
ε = average number of volts required to produce an ion pair

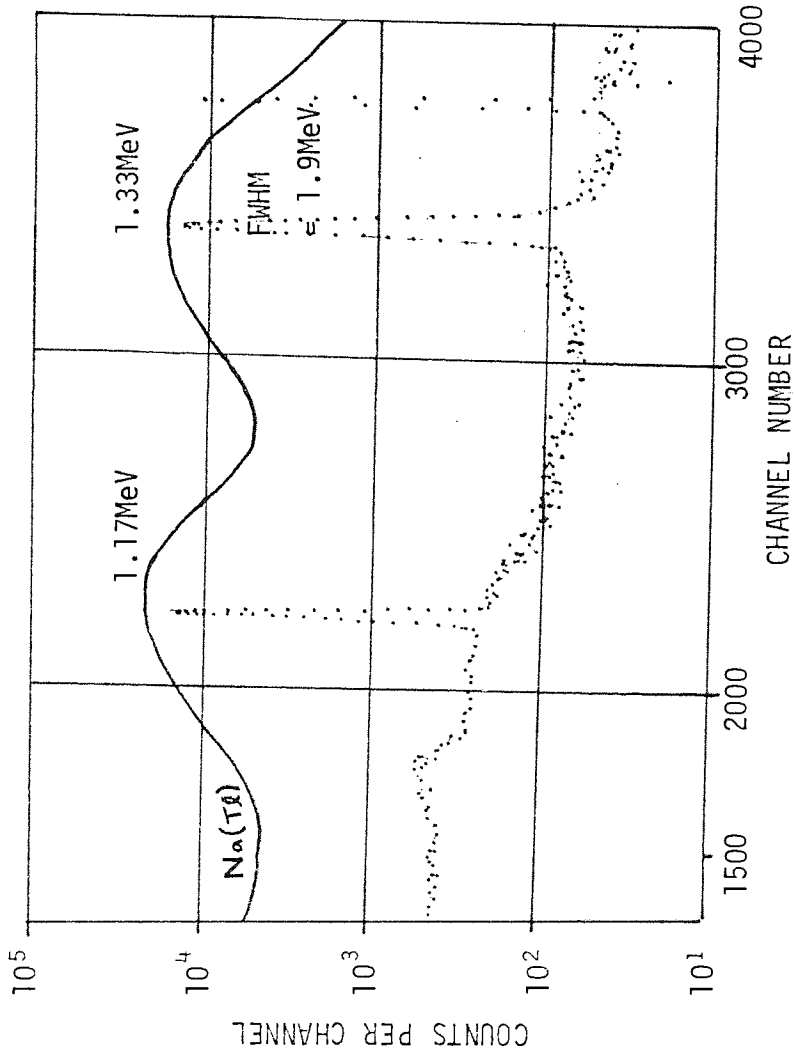

FIGURE 3.3: COBALT 60 GAMMA RAY SPECTRUM FROM Ge(Li) AND NaI (Tl) DETECTORS

Since the detection region is small then it is inherent that the response time is also very good (≈20ns). In fact, the smaller the depletion region the better the response time. However, a trade off between efficiency and response time must meet somewhere along the line.

The Ge(Li) detector responds to both slow and fast neutrons. For slow neutrons, below 0.5MeV, the main reaction is (n,γ) in Ge $\approx$ 2.45 barns/nucleus according to ref.(30). There are three isotopes of Ge: ^{70}Ge (20.6%), ^{74}Ge (36.5%) and ^{76}Ge (7.7%). In radiative capture the isotope ^{70}Ge (n,γ) cross-section is 0.06 barns/nucleus and gives activated ^{71}Ge which decays by electron-capture with a half life of 11 days. The main activity results from ^{74}Ge (n,γ) with a cross-section of 0.16 barns/nucleus and ^{75}Ge the product nucleus which decays by β^- emission with a half life of 85 mins.

To summarise the main reaction caused by fast neutrons in the 0.5-20MeV energy range, Ge contains many closely packed levels and because of this, many gamma rays of different energies are emitted. The main reactions in this region are (n,α), $(n,n'\gamma)$, (n,2n) and (n,p).

The (n,α) and (n,p) produce unstable products resulting in activity from the nuclei ^{70}Ga, ^{72}Ga and ^{74}Ga. These all decay initially by β^- emission followed by gamma ray emission with half lives of 21 mins, 14 mins and 8 mins respectively.

For the (n,α) reaction ^{69}Zn and ^{71}Zn are the product nuclei which decay by β^- emission with half lives of 5.5mins and 2.5 mins respectively.

Scattering of recoil protons also occurs but this is not a major problem.

The main problems with using a Ge(Li) detector are, firstly, because of the small energy gap in the band structure of the junction, it is necessary to keep it at liquid nitrogen temperatures all the time (77K). Also the detector has an inherently low efficiency, because of the small detection region employed. Finally, fast neutrons produce damage in the crystal structure, i.e. displacement of atoms from their equilibrium position, leaving vacancies and interstitial atoms. The result, after a period of time the crystal loses its efficiency and needs redrifting. The ORTEC specification of maximum exposure is 10^8n/cm^2. This means that with 50 neutrons per second incident on the junction over a flight path of 50cm, accounting for a 10% loss in intensity due to shielding, the expected lifetime would be 200 hours and redrifting is expensive and uneconomical.

The NaI(Tl) gamma ray detector is a scintillator device which also relies upon doping for improved efficiency. When the photons are incident upon the NaI(Tl) crystal, the effect is to remove electrons from the valence band and place them in the conduction band. On de-excitation, the electrons release photons. The effect of thallium is to introduce an impurity level half-way between the conduction band and the valence and this effectively doubles light output when the electron returns to the valence band.

The actual NaI(Tl) crystal itself if hygroscopic and deliquescent and hence must be stored in a vacuum. For this reason it is unsuited to particle detection. A typical photon

output per MeV of radiation is about 20,000 photons. This however, depends upon factors such as doping, uniformity and optical transference properties.

To amplify the signal obtained from the NaI(Tl) scintillator, a photomultiplier tube is used. The photons produced impinge onto a photo-cathode, which is coated with a photo-electric material such as SbCsO. The latter converts photons into electrons with an efficiency which is typically 10 percent. The resultant photo-electrons produced by the photo cathode are then accelerated through a series of dynodes. Each dynode, made from a material such as Be Cu, multiplies the number of electrons by a factor of about six at each stage. The voltage per stage is typically 150V. At the final stage of the photomultiplier tube, the resultant signal is collected at the anode. The signal is taken across a large resistor and sent to an amplifier via a decoupling capacitor. In general the gain of the amplifier obeys $G \alpha V^n$ where n = 8 for a 14 stage tube.

NaI(Tl) can be manufactured as very dense crystals (ρ = 3670kgm^{-3}) and since ^{127}I has such a large atomic number then, as a gamma ray detector, the efficiency will be high, since gamma ray absorption in matter depends upon these properties. Another factor contributing towards a high efficiency is the fact that the NaI(Tl) crystal can be manufactured in relatively large bulk size. Typical detection volume would be 3" x 3" diameter crystal.

The resolution of the detector depends upon the following main factors:

i) Excitation and ionisation along the track of the radiation within the crystal

ii) conversion of the energy of excitation into light energy by fluourescence

iii) transfer of light through the crystal and onto the photocathode of the photomultiplier tube

iv) absorption of light at the photocathode with emission of photo-electrons

v) electron multiplication at successive dynodes of the photomultiplier tube.

For gamma ray energies above a few KeV the resolution varies according to the inverse of the square root of the gamma ray energy according to:

$$\left(\frac{\Delta E}{E}\right)^2 = A + {}^{B}/_{E}$$

where

ΔE = Full width at half maximum of the photopeak

E = Energy of gamma ray incident on detector

A and B are constants

A further broadening of the full width at half maximum has been reported by Zerby et al.[31]. In this work it has been shown that a further non-linear response must be taken into account and the true equation for energy resolution should be:

$$\left(\frac{\Delta E}{E}\right)^2 = A + {}^{B}/_{E} + X(E)$$

where $X(E) = R_I^2$

R_I = The effective intrinsic line width, as it is termed, and is given by $R_I = (R^2 - R_p^2)^{\frac{1}{2}}$, where

R = The full width at half maximum of the total absorption peak, and

R_p = Full width at half maximum due to the photomultiplier

tube alone as investigated in ref 32) where they found R_p = 4% for the 0.662MeV peak from ^{137}Cs.

For both the references, the results indicate that in general, the lower the incident gamma ray energy the greater the effect of intrinsic broadening. For a line width resolution of 7.8% from ^{137}Cs spectrum, 4.9% is the contribution from the photomultiplier tube, 4.6% from transfer process and 4% from intrinsic broadening. The origin of intrinsic broadening is believed to be concerned with the probability of formation of an energy carrier, depending on the specific loss of energy of the incident photon.

The response time of the crystal is governed by both the activator, thallium and the temperature. The general expression giving the number of photons per unit time produced in the crystal is:

$$n(t) = \frac{N}{\lambda_D - \lambda_R} \left[\exp\left(\frac{-t}{\lambda_d}\right) - \exp\left(\frac{-t}{\lambda_R}\right) \right]$$

N = Number of photons emitted in the scintillator

λ_R = rise time constant

λ_D = dead time decay constant

Of the latter constants, the most important is the decay time constant which has a typical value of $\simeq 0.34\mu s$ (i.e. large compared with $\lambda_R \simeq 60ns$) as quoted from Eby[33] and Nicholson et al.[34]. This value is large compared with the Ge(Li) detector, but with fast electronics this problem can be overcome.

The neutron response of the NaI(Tl) crystal is governed by four main reaction types:

i) Radiative capture (n,γ)

ii) Inelastic scattering $(n,n'\gamma)$

iii) Charged particle emission (n,α) (n,p)

iv) $(n,2n)$ reactions.

The slow neutron response occurs in the energy range 0.1eV-0.5MeV. Cross-sections for this region are typically (from Barnb ɔok[35]):

Cross-section tabulation for constitutent elements in NaI(Tl):

ELEMENT	ENERGY	
	0.025eV	0.1MeV
^{23}Na	0.525 barn/nucleus	1.3 barns/nucleus
^{127}I	7.0 barn/nucleus	0.43 barns/nucleus
Tl	3.5 barn/nucleus	-

The major effect is that of ^{127}I which becomes ^{128}I on capture of a neutron. The spectrum for this reaction is continuous with a max. pulse height at 6.71 MeV which is the binding energy of a neutron in ^{128}I. The sodium accounts for less than 10% of these reactions.

Capture of neutrons results in a build up of activity in the crystal which comes mainly from the beta decay of ^{128}I to ^{128}Xe. This reaches saturation in approximately three half lives ≈ 75 mins. It has also been shown that (n,γ) reactions are significant only up to 1MeV neutron energies. Studies of $(n,n'\gamma)$ made by Loef et al.[36] in the energy range 0.52 to 3.15MeV reveal further build up of activity mainly due to ^{127}I.

More significantly, at higher neutron energies in the 14MeV region, (n,2n) reactions dominate along with (n,α) and (n,p) reactions. Cross-section for the respective reactions are taken from the barn book[35]: (En = 14.5MeV)

ELEMENT	(n,2n)	(n,α)	(n,p)
^{127}I	1.3 barn/nucl.	1mb/nucl.	230mb/nucl.
^{23}Na	20mb/nucl.	180mb/nucl.	38mb/nucl.

Long lived activity is induced by these reactions. For example, the I^{127} (n,2n) reaction produces I^{126} which decays to te^{126} by β^+ emission and β^- emission to Xe^{126} with half life of 13 days. Long half lives as such cause a slow build up of activity in the crystal, however, the crystal has an excellent resistance to radiation damage and hence does not, as in the case of Ge(Li) detectors require returning to the manufacturers at regular intervals.

For the present work the NaI(Tl) detector was employed. The main reasons for this choice lie in the relatively high efficiency of this detector as opposed to the Ge(Li) detector (i.e. about a factor of five between the efficiency of a $30cm^3$ Ge(Li) detector and a 3 x 3 NaI(Tl) detector). Since in the present application the gamma ray cross-sections are in the millibarn region, then high efficiency was essential for realistic spectra accumulation times. Furthermore, high resolution was not an essential priority for the work to be undertaken here and in view of this fact, the inherently high resolution of the Ge(Li) detector was not needed. Finally in using the NaI(Tl) detector, the efficiency remains constant throughout the work,

owing to its durability in withstanding neutron radiation damage.

3.3.1 Description of detector

The NaI(Tl) scintillator used was a Nuclear Enterprises 76.2 x 76.2mm crystal. This was coupled to a 56AVP photomultiplier tube via a perspex light pipe. The quoted time spread for the tube was <0.5ns. Its construction consisted of a 14 stage dynode chain in which equal voltages were applied to the first five dynodes and increasing voltages to the last nine. Parallel fed capacitors were used across the last four stages in order to stabilise the dynode potential as recommended by manufacturer (see diagram - Figure 3.4).

A Mu-metal shield was incorporated to shield the dynodes from the effect of the earth's magnetic field. It has been shown in Engstrom et al.[37] and Conner et al.[38] that variations in even weak magnetic fields, produce changes in gain of the photomultiplier tube. Since the detector used in this work was not fixed with respect to the earth's magnetic field, then shielding was essential.

The operating voltage was typically 1800 volts (-ve) with a dynode chain current of typically ~2.7mA. Two signals were taken, from the anode to supply the timing line and the second, from the 13th dynode of the photomultiplier tube, via a 50Ω resistor, for the energy line.

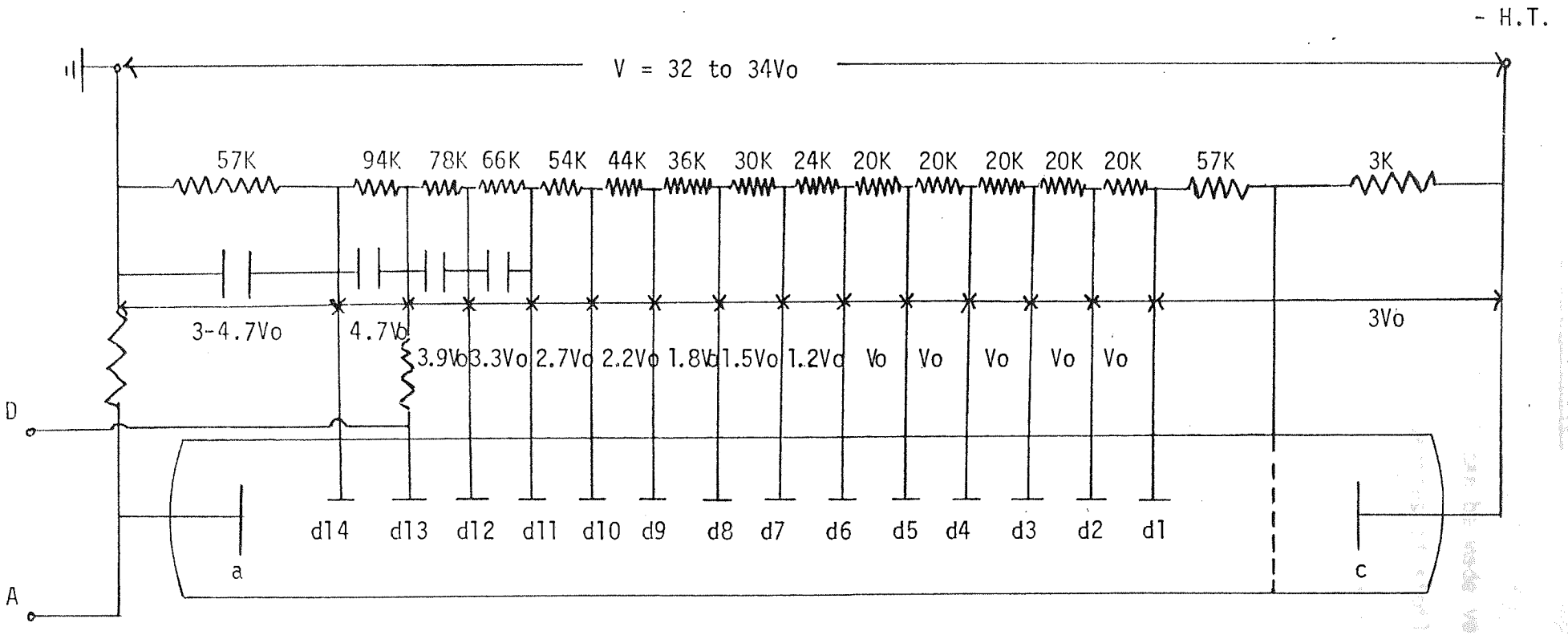

FIGURE 3.4 DYNODE RESISTOR CHAIN USED FOR THE 56-AVP PHOTOMULTIPLIER TUBE USED IN THE GAMMA RAY DETECTOR

3.3.2 Efficiency of the gamma ray detector

Unlike other scintillators, NaI(Tl) can be made very accurately, such that the variation in properties of similar volumes of crystal, is very low. As a result of this, there is much literature available on the properties of standard sized NaI(Tl) detectors[39] [40] from which efficiency measurements may be compared.

There are a number of ways of defining efficiency of which the two most general definitions are:

1. The absolute total gamma ray efficiency $\varepsilon_{Abs}(E_\gamma)$

$$\varepsilon_{Abs} = \frac{\text{No. of pulses recorded (Total area under pulse height)}}{\text{No. of radiation quanta emitted by source}}$$

2. The intrinsic total gamma ray detection efficiency $\varepsilon Int(E_\gamma)$

$$\varepsilon Int(E_\gamma) = \frac{\text{Number of pulses recorded}}{\text{No. of radiation quanta incident on detector}}$$

Both of the above efficiencies depend upon the detector properties and geometry. They are related by the equation:

$$\varepsilon Int = \varepsilon_{Abs} \frac{4\pi}{\Delta\Omega}$$

$\Delta\Omega$ = solid angle subtended by the detector at the gamma ray source.

In gamma ray spectroscopy however, because of Compton degradation and absorption within the detector, it is more useful to define two similar efficiencies, that are related directly to the photopeak of the pulse height spectrum:

i) $\varepsilon p\text{-}abs = \frac{\text{Number of full energy events in photopeak}}{\text{Number of quanta emitted by source}}$

ii) $\varepsilon p\text{-}int = \frac{\text{Number of full energy events in photopeak}}{\text{Number of radiation quanta incident on the detector}}$

To measure the efficiency of the NaI(Tl) detector experimentally, it is necessary to define another factor called the peak to total ratio:

$$X = \frac{\varepsilon p\text{-}abs}{\varepsilon_{Abs}}$$

The latter was determined for the 0.662MeV peak from ^{137}Cs and the 1.28MeV peak for ^{22}Na source. In both cases the results agreed to within 3% of other workers Connel[42], Heath[39], Al-shalabi[40]. Figure 3.5 shows the overall agreement, between results for the peak to total ratio.

The total gamma ray efficiency $\varepsilon_{Abs}(E_\gamma)$ was calculated using the product of the fraction of incident gamma rays penetrating the detector window and the fraction of interactions within the crystal:

$$\varepsilon_{Abs}(E_\gamma) = \exp(-\mu_A X_A)\left[1 - \exp(-\mu_c X_c)\right]$$

The entrance window was made of aluminium with a thickness X_A quoted as 280mg/cm^2 by the manufacturers. X_c was taken as 76.2mm, the crystal thickness. The total linear absorption coefficients μ_A and μ_c for aluminium and NaI respectively were taken from Ref (41).

The density of the NaI(Tl) crystal was quoted as 3760Kgm^{-3} by manufacturers and was necessary in calculatingthe total linear

absorption coefficient from the tabulated total Mass absorption coefficients. The actual peak efficiency was then found using the values of Figure 3.5 and the equation:

$$\varepsilon_{p\text{-}Abs} = X\varepsilon_{Abs}$$

Figure 3.6 shows the overall photopeak efficiencies.

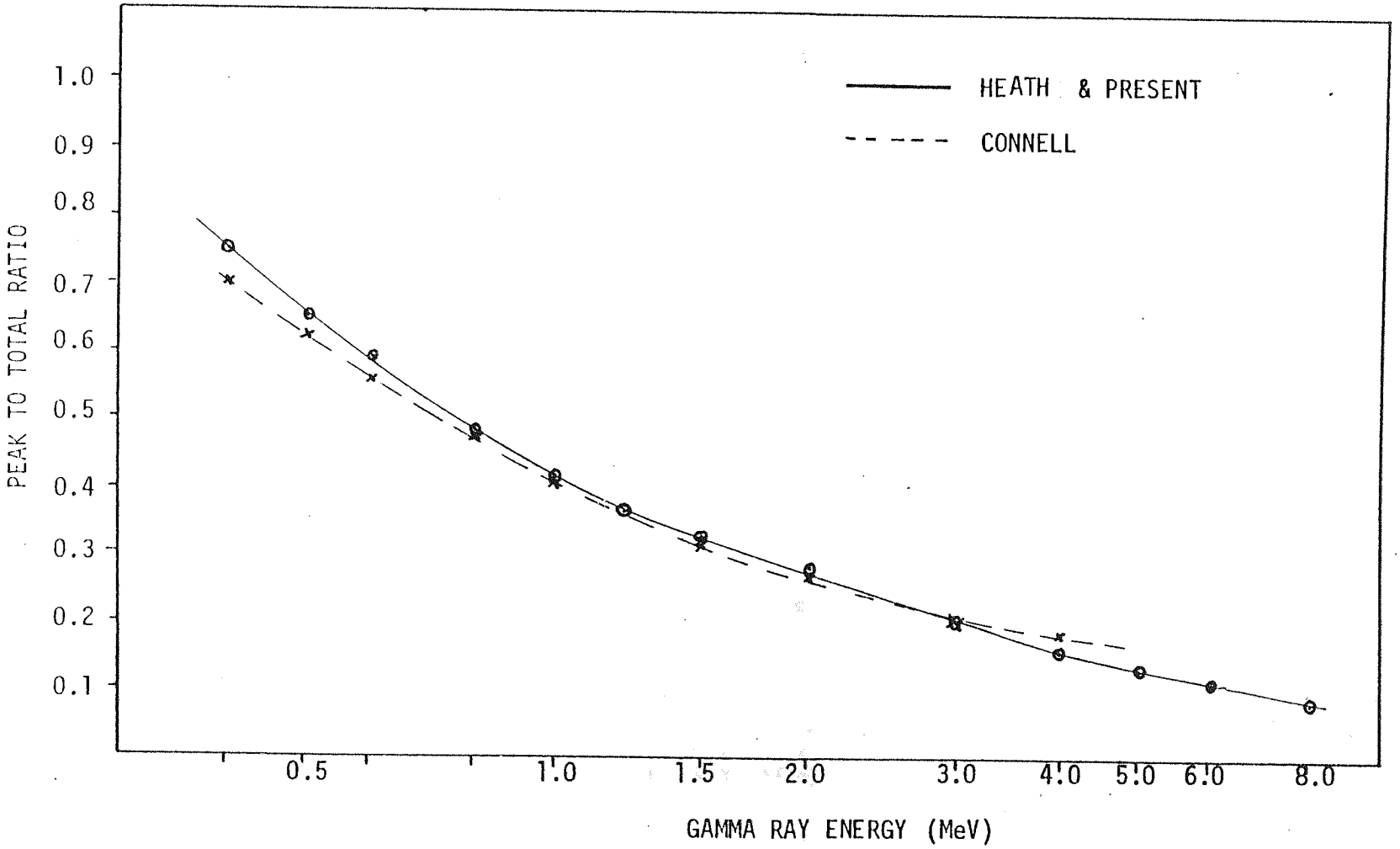

FIGURE 3.5 PEAK TO TOTAL RATIO AS A FUNCTION OF ENERGY FOR THE 762 x 762mm NaI(Tl) DETECTOR

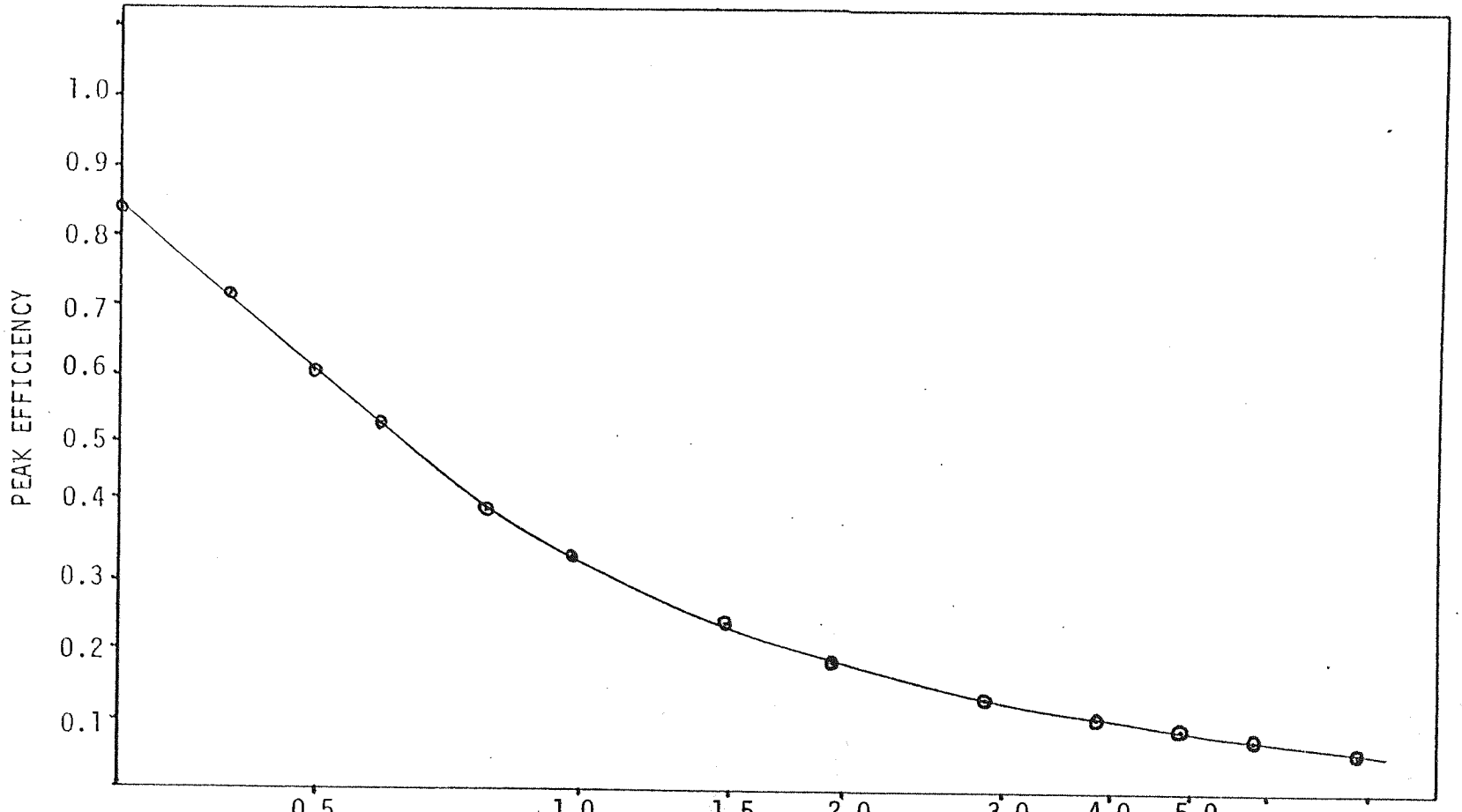

FIGURE 3.6 EFFICIENCY OF NaI(Tl) DETECTOR AS A FUNCTION OF ENERGY

3.4 Shielding of the NaI(Tl) detector

Construction of the NaI(Tl) detector shield has been described in detail by Connel[42]. Briefly, the design of any such shield, where closed geometry is being used, should take into account the following important properties:

i) Moderation of fast neutrons
ii) Absorption of subsequently moderated slow neutrons
iii) Absorption of secondary gamma radiation.

The actual shield used is shown in Figure (3.7) and consists of three concentric cylinders designed to achieve the considerations outlined above. The fast neutrons were moderated with paraffin wax, whose chemical formula was of the form $C_n H_{2n+2}$. The main source of energy loss here, was elastic scattering from the hydrogen atoms. Gamma rays of energy 4.43MeV were emitted by inelastic scattering to excite the carbon nuclei. However, the cross-section for this reaction was very low compared to that of elastic scattering. A further source of gamma rays produced in the paraffin wax, was due to thermal neutron capture of hydrogen emitting 2.23MeV gamma rays. Absorption of subsequently moderated neutrons was achieved using a layer of boric oxide. The boron has a thermal neutron cross-section of about 3800 barns/nucleus, varying as the inverse of velocity of the neutron, to 6 barns/nucleus at 10^4eV. The main absorption reaction was due to (n,α) and the product nucleus $^{7}_{3}Li$ gave a 0.474MeV gamma ray.

All secondary gamma rays were then absorbed in the lead shield layer. Lead is ideal for this purpose, since it has a high density and high atomic number.

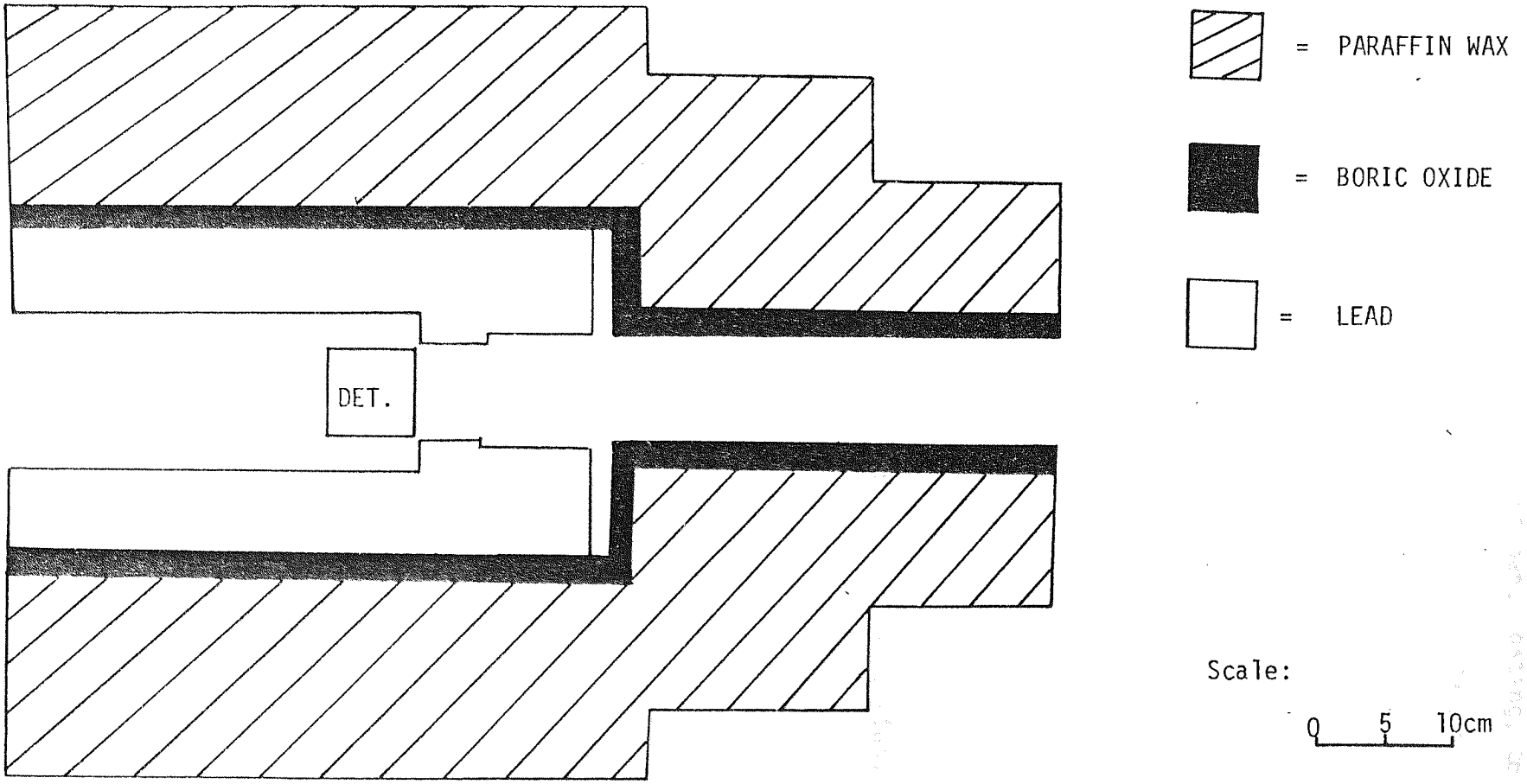

FIGURE 3.7 CONSTITUENTS OF GAMMA RAY DETECTOR SHIELD

3.5 Description of the Electronics

The electronic system is summarised in Figure 3.8. The spectrometer relies upon time of flight coincidence gating, to separate neutrons from gamma rays. Negative pulses from the anodes of both the gamma ray detector and the alpha detector supply the time of flight circuit which will be discussed in section 3.5.1. The time of flight circuit provides pulses to open the linear gate only when a gamma ray arrives along the linear line. The signal for the linear line is taken from the 13th dynode of the 56 AVP photomultiplier tube. These positive pulses then pass through an ORTEC 113 all transistor amplifier, which has a high input impedance (~1MΩ) and a variable output impedance. Since the gamma ray detector was placed in a separate room to the control room and electronic apparatus, the variable output impedance of the preamp, was used to match the lengthy (~10m) coaxial cable, to the rest of the circuit. This was achieved by setting the output impedance to 50Ω, which was the nominal impedance of the cable. Since the pre-amp was non-inverting with a gain of unity, output pulses were amplified and shaped using an ORTEC-485 linear amplifier. This provided approximately Gaussian shaped positive pulses to the linear delay. The linear delay was also a non-inverting amplifier with a gain of unity (Nuclear enterprises) and was used to equalise the delay time in both, linear line and time of flight line, so that gamma rays arrived at the linear gate (ORTEC-426) at the same time as it was opened by the timing circuit. Resulting gamma ray spectra were accumulated in a 100 channel TMC pulse height analyser.

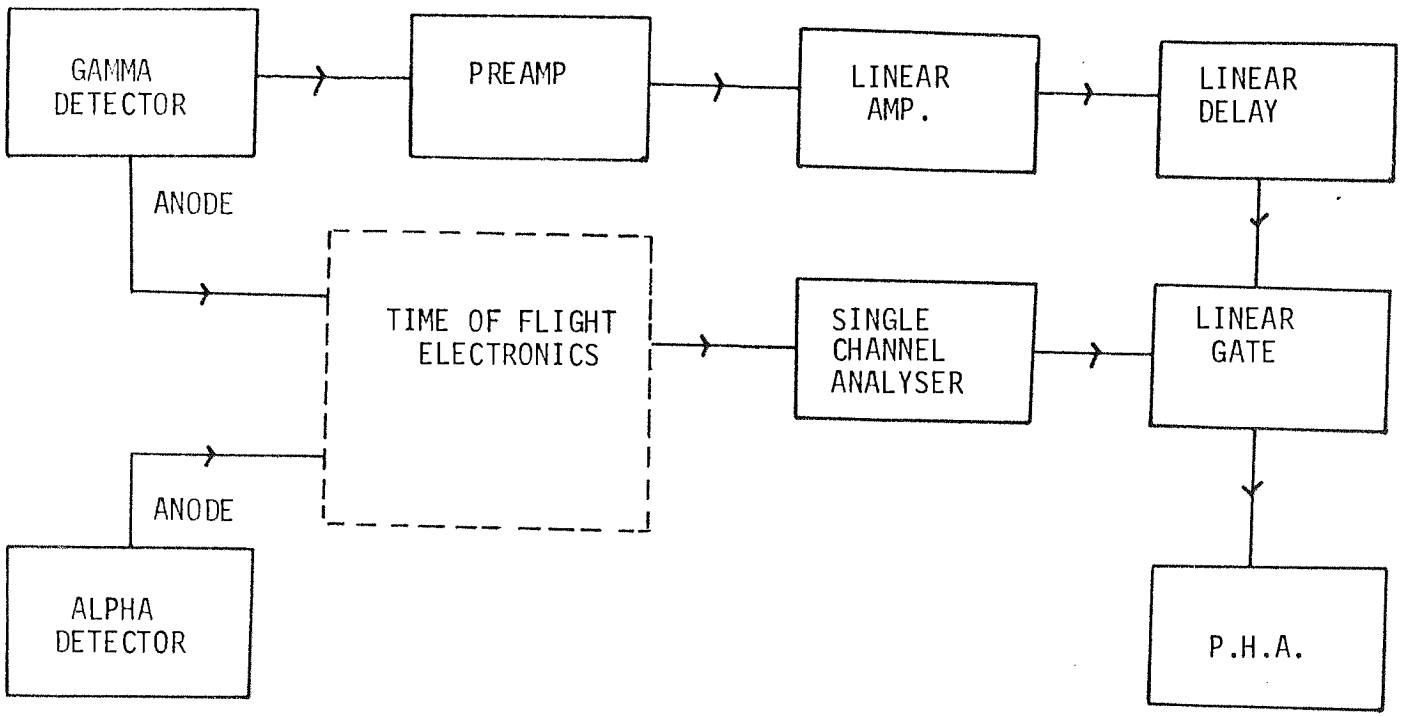

FIGURE 3.8 COMPLETE CIRCUIT FOR GAMMA RAY SPECTROMETER

3.5.1 Time of flight electronics

The time of flight technique employed here is similar to that in refs. 4 and 5. Nanosecond timing resolution is essential since in general, the time difference between a gamma ray and neutron of energy E MeV over a flight path D metres is given by:

$$\Delta t = 72.3\ E^{-\frac{1}{2}} D - D/C$$

C = Velocity of light.

The formula shows that for a 14MeV neutron over a flight path of 85cm, Δt will be about 16ns.

The diagram overleaf (Figure 3.9) shows the electronics used to obtain this kind of fast timing resolution. A reference signal was obtained from the α-particles associated with the production of neutrons in the $T(d,n)^4He$ reaction. The resultant negative pulses, produced at the anode of the photomultiplier tube, were passed to a very fast 100MHz ORTEC 436 amplifier. The input impedance of this amplifier served to match the coaxial cable to the circuit, with a variable discrimination level between 50mV and 500 mV. The discrimination level for the alpha pulses was set using the circuit shown in Figure 3.10. The resultant spectrum is shown in Figure 3.11 for the discriminator set at 125mV. Negative pulses from the 100MHz discriminator were then passed through an ORTEC 416A gate and delay generator, the purpose of which was to delay the alpha pulses with respect to the neutrons and gamma pulses. The output consisted of very fast negative logic pulses with rise times of $\lesssim$ 10ns and widths of about 25ns. These pulses were then sent to the start input of a Nuclear Enterprises time

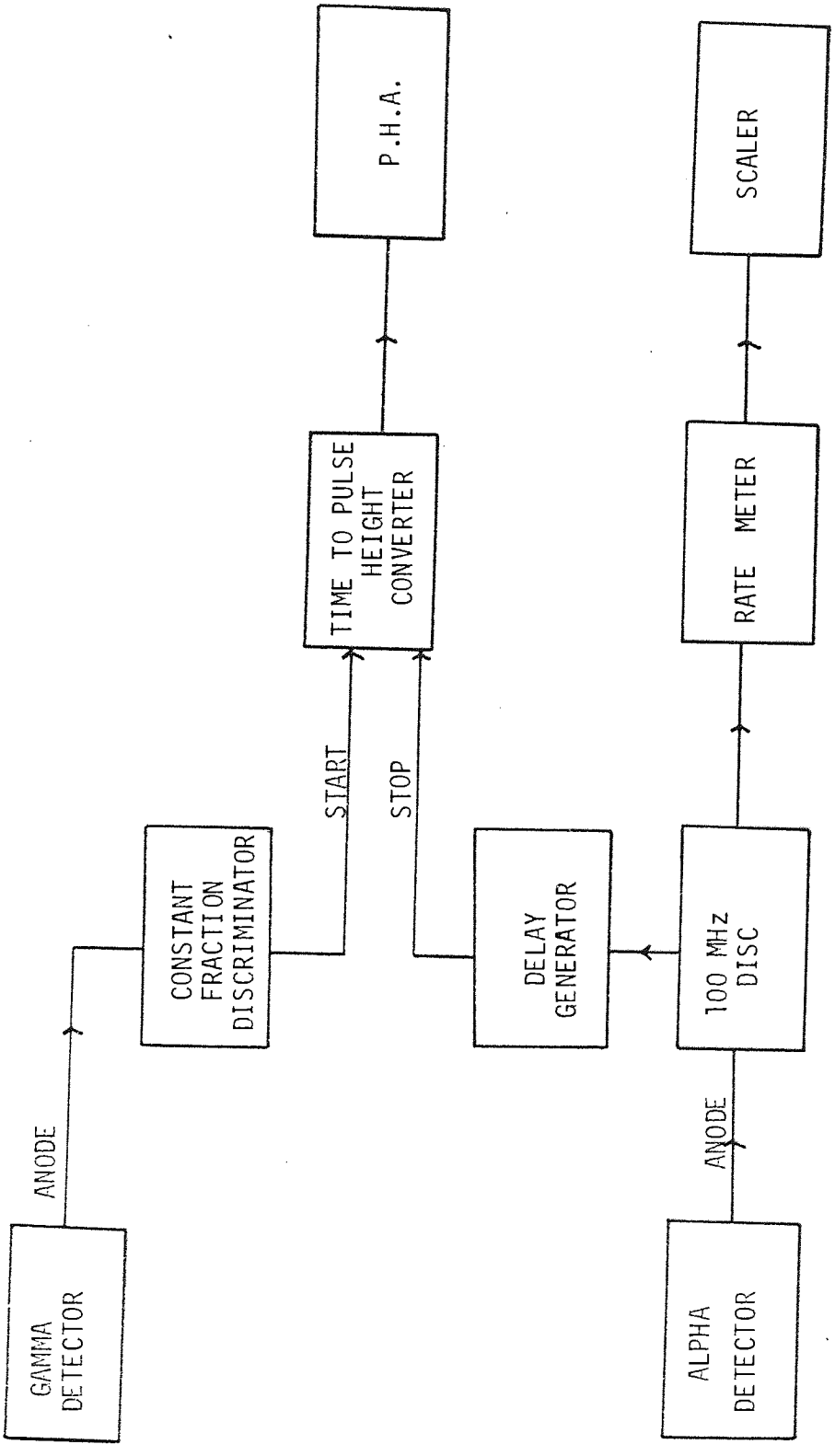

FIGURE 3.9 TIME OF FLIGHT CIRCUIT

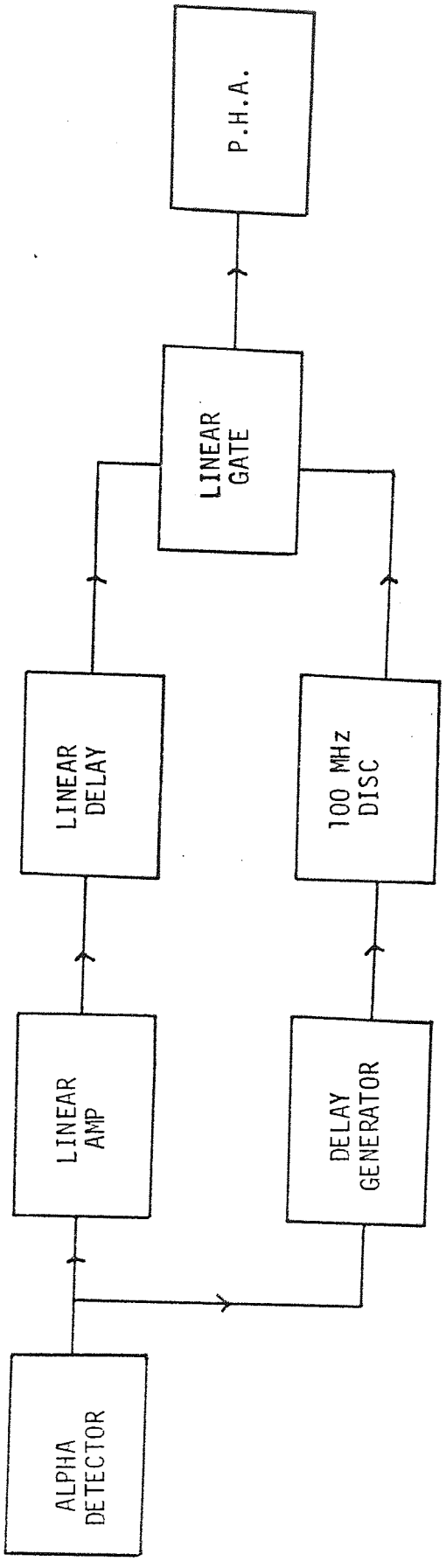

FIGURE 3.10 CIRCUIT FOR SETTING ALPHA DISCRIMINATOR

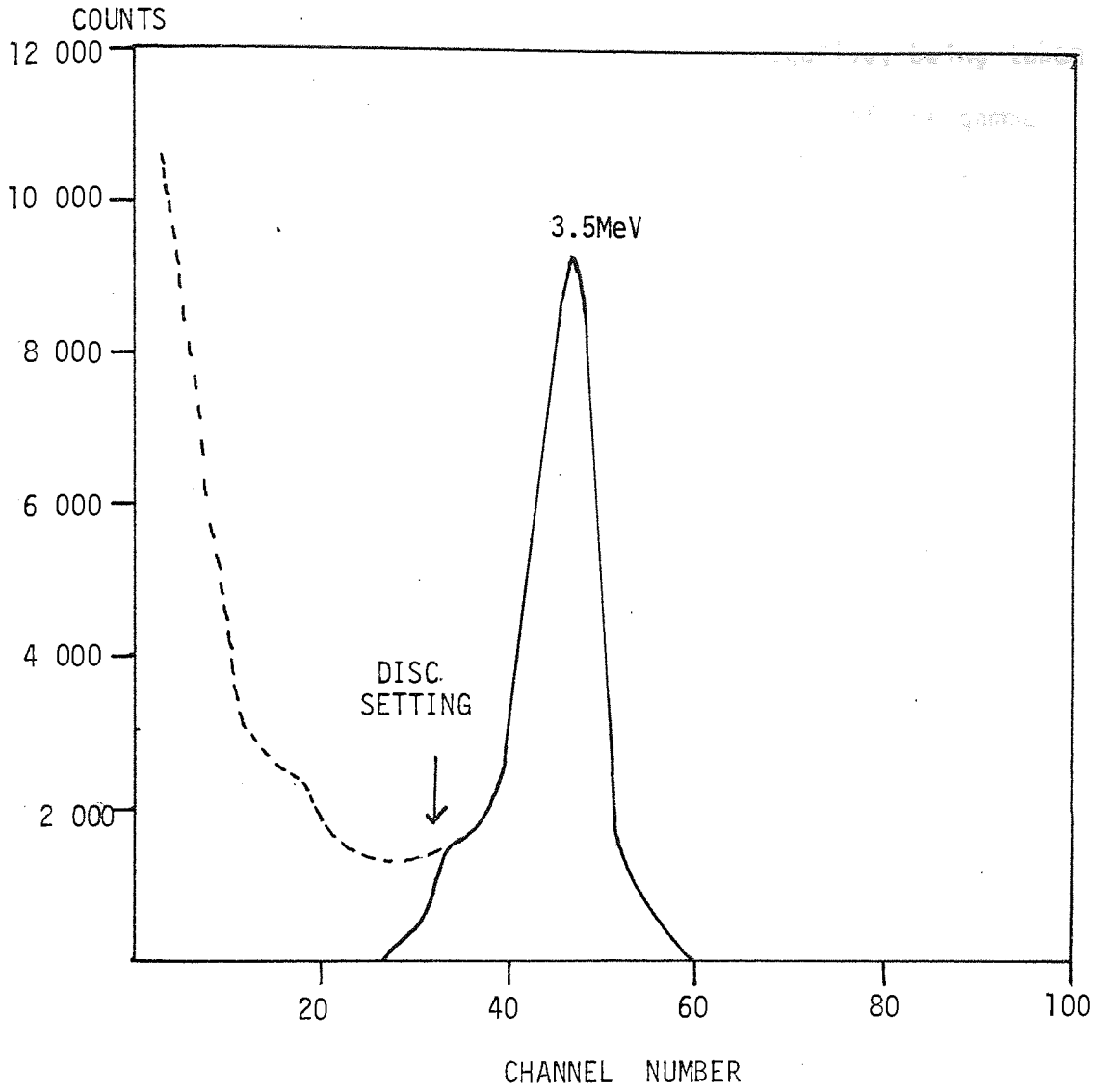

FIGURE 3.11 ALPHA PARTICLE PULSE HEIGHT SPECTRUM

to pulse height converter.

The gamma ray-neutron pulses were also negative, being taken from the anode of the 56 AVP photomultiplier tube of the gamma detector. These pulses were fed to an ORTEC 463 constant fraction discriminator which again had an input inpedance of 50Ω for matching. This unit provided a negative logic pulse for each input pulse. Basically, the input pulse was used to charge a capacitor circuit such that a constant fraction of the total charge, depending on the discriminator setting, would be drawn off and the logic pulse produced would be proportional to this. Discrimination by this method in timing circuits has the advantage that it overcomes the problem of "time walk". This problem will occur when timing from the leading edges of different sized pulses, as illustrated in the following diagram:

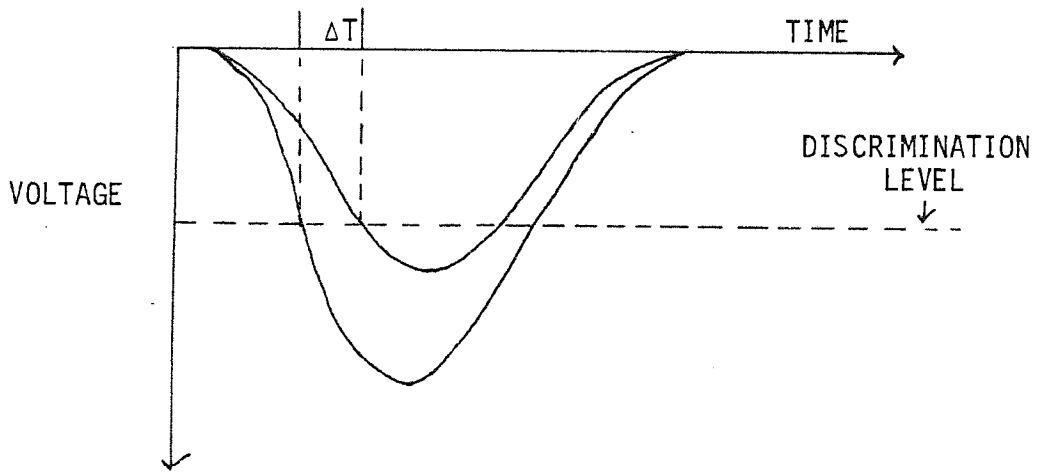

As can be seen, the discriminator level setting introduces the uncertainty ΔT known as time walk. The constant fraction discriminator overcomes this problem, since it considers only a set fraction of the charge produced by the pulses.

The difference in time between the neutron-gamma pulses and the alpha pulses were converted to voltage differences by the

Nuclear enterprises time to pulse height converter. The output was sent to a 100 channel TMC pulse height analyser. Figure 3.12 shows the pulse spectrum for the direct neutron beam at 0° and gives a full width half maximum of 8.4ns. Figure 3.13 illustrates a typical time spectrum, the resolution of the gamma peak being 13ns for a 9cm thick LiF sample with the detector at 45°. The time spectrum also illustrates, how the electronic window of the single channel analyser may be set, to allow only gamma signals to open the gate of the full electronic circuit of Figure 3.8.

3.5.2 Calibration of linear line

Calibration of the linear line was achieved using standard gamma ray sources and the circuit shown overleaf. As can be seen, pulses from the BNC pulse generator were used to simulate those being produced in the actual experiment. The standard sources used are tabulated:

SOURCE	ENERGY (MeV)
^{137}Cs	0.66
^{60}Co	1.17
	1.33
^{22}Na	0.511
	1.28
$^{241}Am/^{9}Be$	4.43

The calibration was found to be linear to within ± 1%. During this process the constant fraction discriminator level was set to 50mV using the 0.511MeV peak from ^{22}Na as a reference.

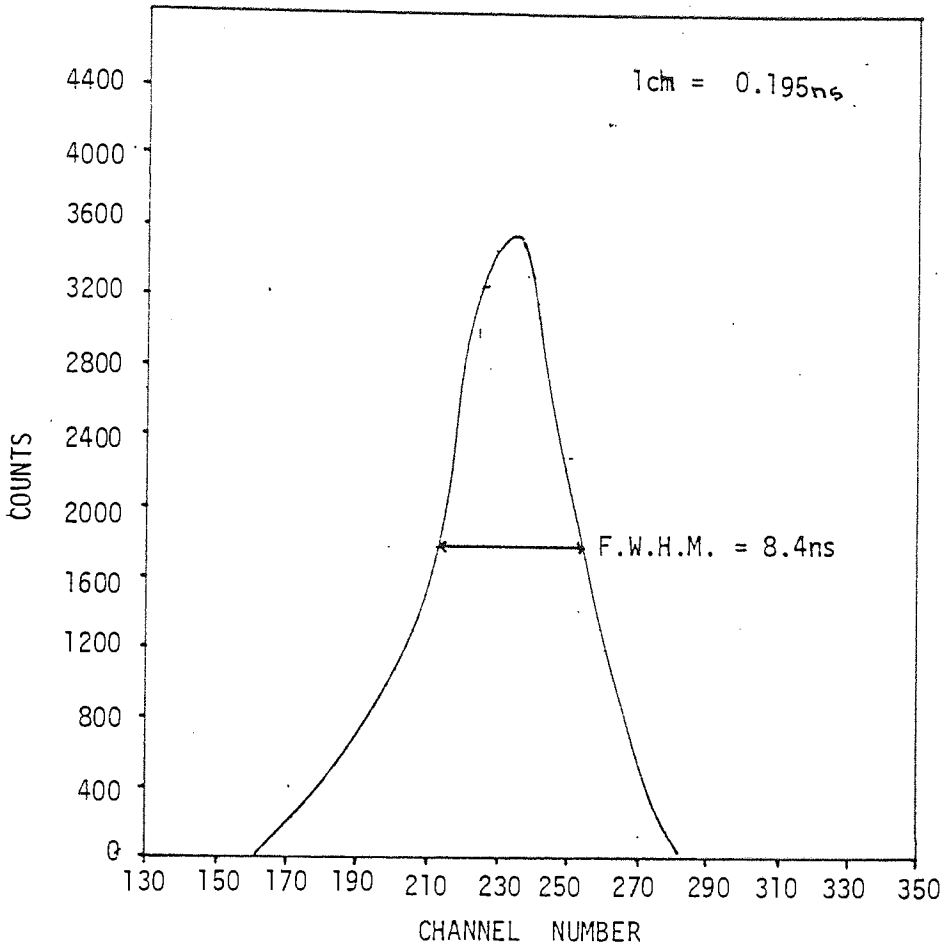

FIGURE 3.12 DIRECT BEAM

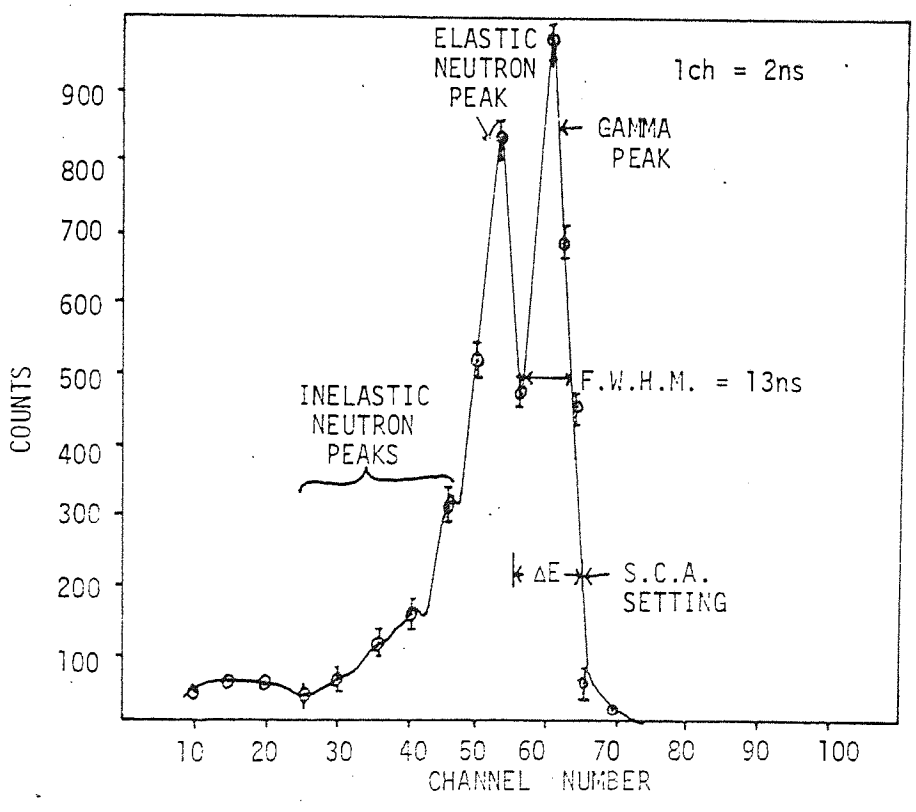

FIGURE 3.13 TIME SPECTRUM FOR LiF (9cm) SAMPLE SHOWING RESOLUTION OF GAMMA PEAK

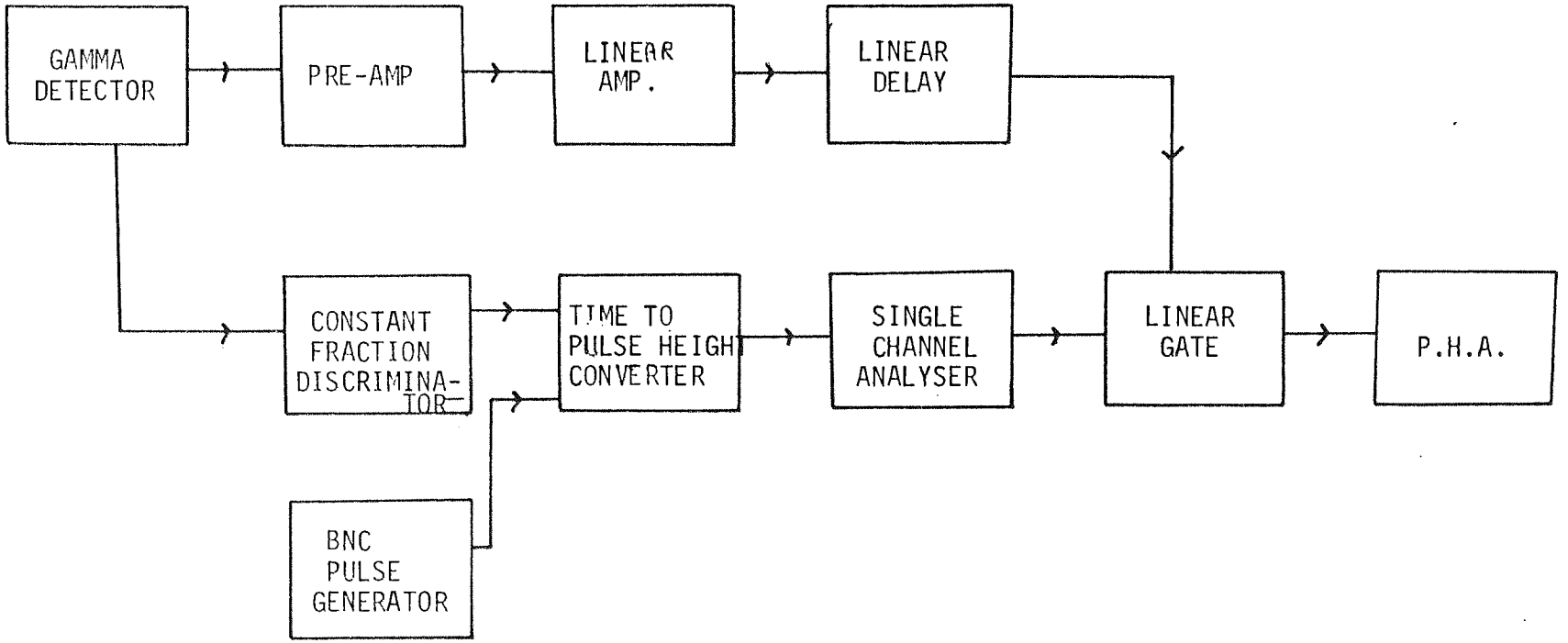

FIGURE 3.14 CIRCUIT USED TO CALIBRATE LINEAR LINE

CHAPTER 4

EXPERIMENTAL PROCEDURE AND RESULTS

4.1 Experimental Procedure

At the beginning of each run it was necessary to switch on all E.H.T. supplies and electronics, for a period of about one hour, to stabilise before any calibration could be made. The S.A.M.E.S. accelerator was also allowed to stabilise so as to produce a constant beam current before each run.

Initially the gamma ray detector was arranged at 0° with no sample in position, and hence the direct neutron beam could be found, using the time of flight circuit. The gate and delay generator were varied to position the neutron peak in about channel number 50 of the 100 channel TMC pulse height analyser. The gamma detector was then moved to 30° scattering angle, for the same flight path (≈85cm) and a sample placed on the sample stand. A time spectrum could then be accumulated and the single channel analyser window set to allow only the gamma ray pulses through the time of flight circuit.

A schematic diagram (Figure 4.1) illustrates the overall laboratory arrangement. Samples were positioned between 25cm and 10cm from the neutron source, for angles between 30° and 90° respectively. These distances were chosen according to how efficiently the shadow bar could be used to shield the detector from the direct neutron source background. In each case the shadow bar was arranged such that, the whole sample was in view through the detector collimator, yet, the tritium target could not be seen, thus preventing any unscattered beam entering the detector.

The next stage was to calibrate the linear line using standard sources in the way described in Section (3.5.2).

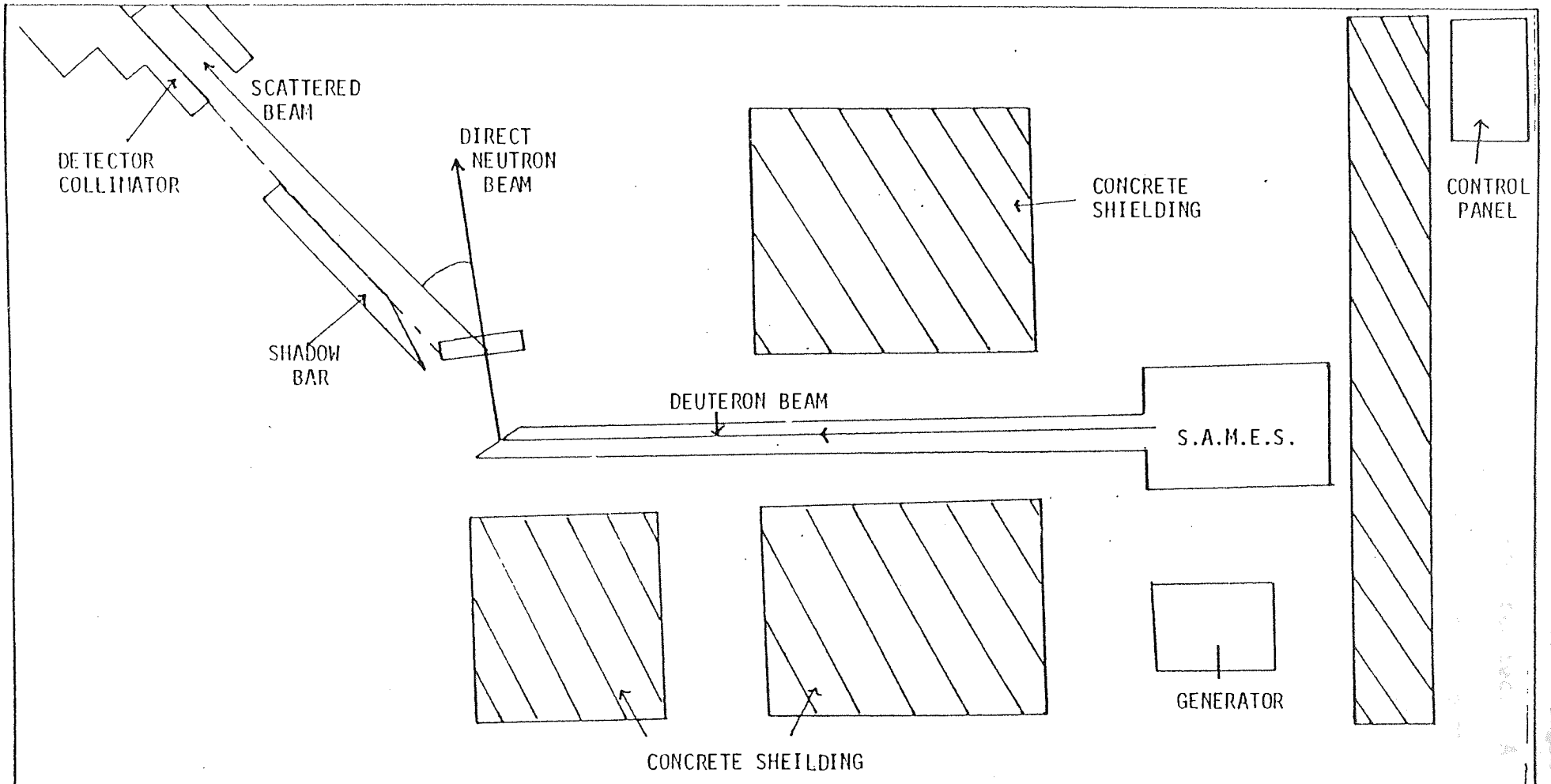

FIGURE 4.1 SCHEMATIC DIAGRAM OF THELABORATORY ARRANGEMENT

During operation the S.A.M.E.S. accelerator was arranged to give a constant incident beam of 60 000 neutrons per sec. A gamma ray spectrum was obtained by accumulating for a preset incident neutron count, with the sample in position and then, using the subtraction mode of the TMC analyser, the random background was subtracted for the same counts with no sample in position. Since the overall random background in the laboratory increased throughout the day, due to a build up in activity, it was found best to accumulate and subtract in approximately half hour intervals throughout the day. For the case of lithium samples, empty aluminium containers were used for the subtraction mode.

It was important to keep the beam constant because the background flux depends upon random coincidence of background detected by the gamma ray detector and the alpha pulses. The background B, is thus proportional to the product of background flux and alpha particle count rate. Both the latter are proportional to the incident neutron flux No, thus

$$B \propto N_o^2$$

since the latter is not a linear relationship the beam must be held at a constant level for both accumulation and subtraction modes so that a true integrated flux may be estimated.

4.2 Differential Cross-section Measurement

In general for a sample of thickness b, with an incident neutron flux No, the total flux of scattered particles is given by:

$$\text{TOTAL FLUX} = No\,(1 - e^{-\Sigma b})$$

where Σ = Total macroscopic cross-section

$(1 - e^{-\Sigma b})$ = Fraction of incident particles interacting.

The total gamma ray yield is then given by multiplying by the fraction of scattered particles that yield gamma rays of interest

$$G = No\,(1 - e^{-\Sigma b})\,\frac{\sigma(n,n'\gamma)}{\sigma_T}$$

σ_T = Total cross-section

$\sigma(n,n'\gamma)$ = Cross-section for gamma ray production.

To find the yield of gamma rays $y(\theta)$ scattered into a specific solid angle, the formula can be made to include the differential cross-section:

$$y(\theta) = No\,(1 - e^{-\Sigma b})\,\frac{1}{\sigma_T}\int_{\Omega}\frac{d\sigma}{d\Omega}\,d\Omega$$

If the integral is over only a very small solid angle $\Delta\Omega$, then the integral may be replaced by the product $\frac{d\sigma}{d\Omega}\,\Delta\Omega$. Rearranging the formula gives:

$$\frac{d\sigma}{d\Omega}(n,n'\gamma) = \frac{y(\theta)\sigma_T}{No\,(1 - \exp(-\Sigma b))\Delta\Omega} \qquad \ldots\ldots\ldots\ldots 4.1$$

For practical purposes a number of correction factors have to be included and these are discussed below.

4.2.1 Gamma ray self absorption factor

Although $y(\theta)$ is the actual number of gamma rays produced in the sample, for an incident neutron flux No, a fraction of these will be self absorbed. To calculate this fraction, consider the diagram overleaf. The fraction of gamma rays absorbed in element dx at an angle θ is given by:

$$dS(\theta,E,x) = \exp(-\mu l)\,\frac{dx}{b}$$

μ = Gamma ray absorption coefficient

from the diagram:

$$l = \frac{x}{\cos\theta} \qquad \therefore \quad S(\theta,E,x) = \frac{1}{b}\int_0^b \exp\left(-\mu x/\cos\theta\right) dx$$

$$\therefore \quad \underline{\underline{S(\theta,E,x) = \frac{\cos\theta}{\mu b}\left[1 - \exp\left(-\frac{\mu b}{\cos\theta}\right)\right]}}$$

By a similar argument, for angles greater than θ_M we have:

$$\underline{\underline{S(\theta,E,x) = \frac{\sin\theta}{\mu W}\left[1 - \exp\left(-\frac{\mu W}{\sin\theta}\right)\right]}}$$

where

$$\theta_M = \tan^{-1}\left(\frac{W}{2b}\right)$$

For a compound such as LiF then:

$$\left(\frac{\mu}{\rho}\right) = \Sigma W_i \left(\frac{\mu_i}{\rho_i}\right)$$

where ρ is the density of the compount and Wi is the proportion by weight of an element in a compound. Thus for LiF:

$$\left(\mu/\rho\right) = \frac{7}{26}\,\mu(\mathrm{Li}) + \frac{19}{26}\,(\mathrm{F})$$

(μ/ρ) values were found from refs.14 and 16.

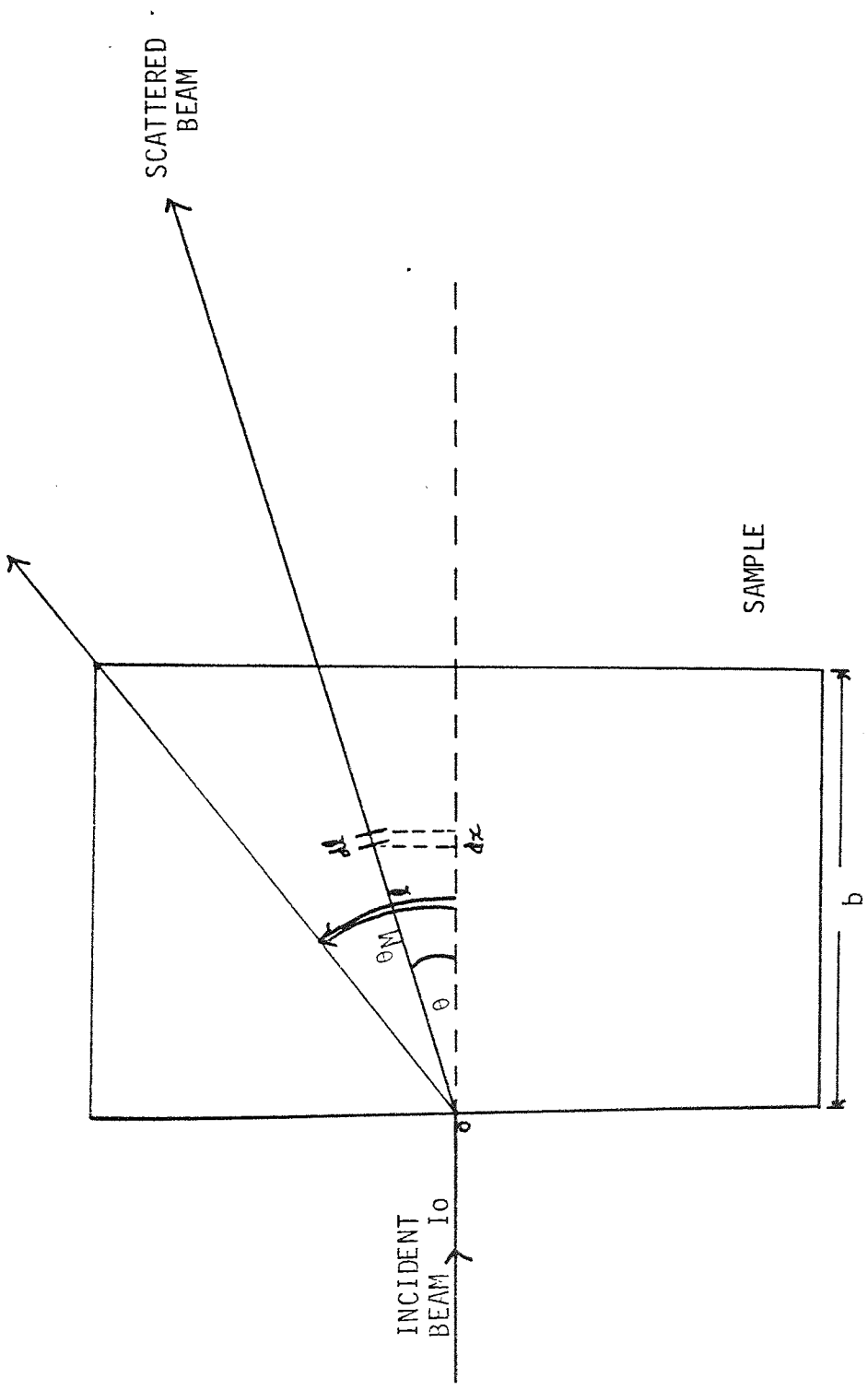

FIGURE 4.2 PLAN VIEW OF SAMPLE FOR CALCULATION OF $S(\theta,E,x)$

4.2.2 Geometry factor correction

The neutron beam has a finite size, being defined by the aperture of the alpha particle detector. From the target the beam has a 6° half angle in the vertical plane and a 3.5° half angle in the horizontal plane. The effect of this is to give an extended gamma ray source within the sample. Since the neutron beam is highly forward peaked, then as a weighted fraction, the effective area A_F emitting gamma rays in the direction of the detector, will depend mainly on the defined neutron beam. Because of the collimation and finite area of the detector face, then for large samples a correction factor had to be made to take into account the fact that, all the gamma rays leaving the sample at a specific angle, did not enter the detector. This factor was calculated by determining the effective area of sample emitting gamma rays in the plane of the detector, in the direction of the detector and dividing this by the area of the detector face, A_d:

$$G = \frac{A_F}{A_d}$$

Figure 4.3 illustrates how A_F is found and hence the geometry factor calculated either by scale drawing or trigonometry. A programme in B.A.S.I.C. language is given in the appendix 1 for calculation of this factor by trigonometry.

4.2.3 Efficiency of the detector

Since the gamma ray detector is not 100% efficient in detecting gamma rays, a correction must be made to the measured counts $P(\theta)$. The efficiency of the detector was discussed in

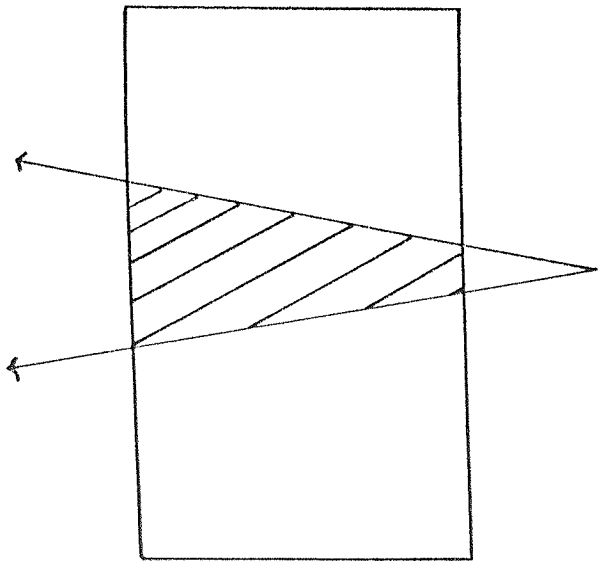

(a) Effective area A_F at 90°

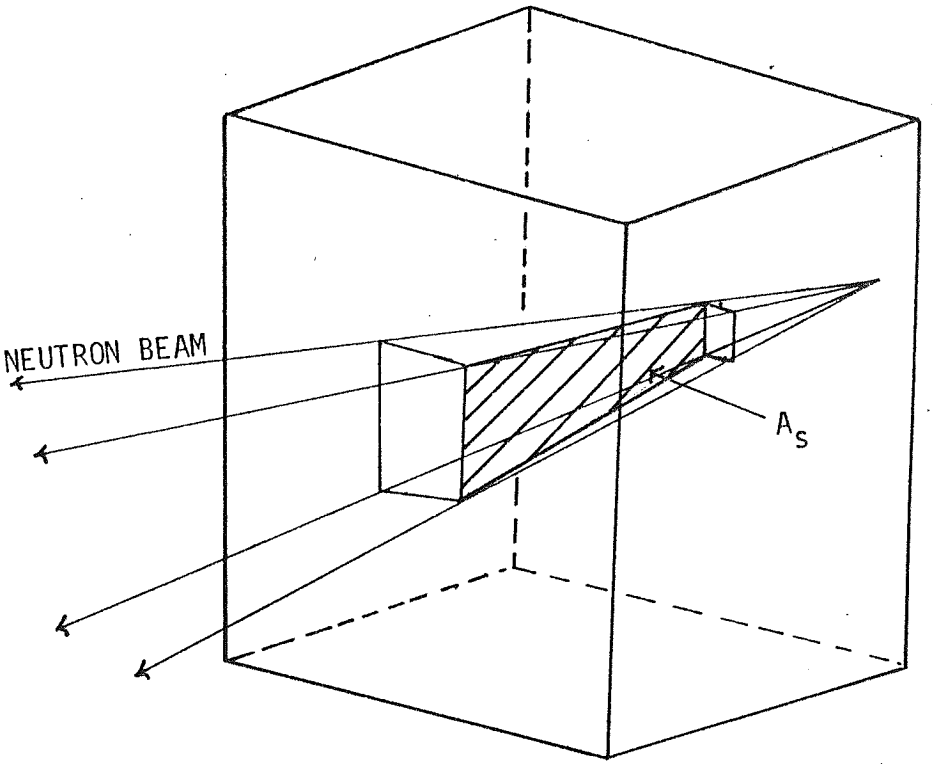

(b) In general the shaded area should be resolved into the plane of the detector

$$A_F = A_S \sin \theta$$

FIGURE 4.3 ILLUSTRATION OF GEOMETRY FACTOR CALCULATION

section (3.3.2). In the case of the lead cross-section measurements an average efficiency over an energy range was determined. The average value was found using Figure 3.6 and the following formula:

$$\bar{\varepsilon} = \frac{\sum_{I=E_k}^{i=E_n} \varepsilon_i}{(E_n - E_k)}$$

where:

$\bar{\varepsilon}$ = Average efficiency between energy Ek and En

ε_i = i_{th} value of efficiency taken between limits E_k and E_n of efficiency curve.

The formula was easily evaluated using a P.E.T. Commodore computer for the energy ranges required.

4.2.4 Background correction factor F_1

The neutron flux is determined by counting the associated alpha particles from the T(d,n)α reaction. However, the measured counts have to be corrected for both prompt and activation background resulting from the excitation of the target assembly materials.

The gamma ray spectrum for the activation background has been investigated by Connell[42] who found photopeaks of energies 0.511, 0.85, 1.81 and 2.12MeV. The main target material constituents are Cu, Zn and Fe and the most probable reaction producing the last three photopeaks is:

$$^{56}Fe\ (n,p)\ ^{56}Mn \xrightarrow{\beta^-} {}^{56}Fe^*$$

The (n,p) reaction has a cross-section of 110mb for 14MeV neutrons and a half life of 2.6hours. However, the gamma rays are produced by subsequent decay of the iron.

The 0.51MeV peak was found to have a half life of 10mins. and was due to annihilation radiation produced by positron emission in the following reaction:

$$^{63}Cu\ (n,2n)^{62}\ Cu \xrightarrow{\beta+} {}^{62}N_i$$

The cross-section for this reaction is high being 550mb.

The correction due to activation background was measured experimentally by monitoring the background throughout the day of a typical run. When the deuteron beam is switched off, the count rate from the alpha detector may be observed, from which it has been found that on average the correction factor is 0.5%. To allow the activation background to reach saturation the machine was allowed to stabilise for a period of about 60mins before each run.

The main correction factor to the neutron flux, was due to fast neutron background, the main source of which was neutrons being scattered at 90° to the incident deuteron beam. This was also measured experimentally by running the machine to give a constant 60 000 alpha's per second and counting for a preset time. This process was then repeated by replacing the alpha detector aperture plate with a solid 1mm thick aluminium plate. The range of 3.5MeV alpha particles in aluminium was given by Whaling[43] to be 0.017mm and hence all alpha particles would be stopped by the 1mm plate. The resulting counts could then be only due to fast neutrons and prompt gamma rays which penetrate

the aluminium. In this way, the total correction factor for background was found to be: $F_1 = 0.945 \pm 0.005$.

4.2.5 Neutron absorption in the target assembly

Neutrons produced in the target pass through 2.5mm to ± 0.03mm of steel and 1.3mm ± 0.03mm of water, according to target manufacturers data, before hitting the actual sample. A correction factor F_2 must be made using cross-section data supplied by K.A. Connell[42] for 14MeV neutrons:

IRON	σ	=	2.32 barns ± 0.05
OXYGEN	σ	=	1.52 barns ± 0.05
HYDROGEN	σ	=	0.64 barns ± 0.05

The correction factor was then found using the formula:

$$F_2 = \exp\left[-\Sigma_{F_e} x_{F_e} - x_{H_2O} (\Sigma_H + \Sigma_O)\right]$$

where

Σ_{F_e} = Macroscopic cross-section for iron

Σ_H = Macroscopic cross-section for hydrogen

Σ_O = Macroscopic cross-section for oxygen

x = Thickness, with subscript giving chemical symbols as for latter.

From this the correction was $F_2 = 0.939 \pm 0.005$.

The latter illustrates the final correction to the cross-section formula 1 and differential cross-sections were found from the new form:

$$\frac{d\sigma}{d\Omega} = \frac{\sigma_T P(\theta) G}{No\ (1-\exp(-\Sigma b))\Delta\Omega\ S(\theta,E,x)\ F_1 F_2 \varepsilon}$$

4.3 Measurement of P(θ)

Typical gamma ray spectra may contain many photopeaks due to the de-excitation of levels within a target nucleus. The complexity of the spectrum, will depend upon the target nucleus level density and the energy of excitation of the incident nucleon. Because of the interaction of gamma rays in matter, each de-excitation will produce a photopeak containing an associated continuous Compton background and maybe two escape peaks, depending on the size of the NaI(Tl) crystal and the incident gamma ray energy. There are a number of methods available for the analysis of such complicated spectra and these will be discussed below.

Graphical stripping is a popular method of analysing such spectra. This method requires the use of a catalogue of standard mono peak gamma ray sources, to obtain the response of the detector, for each gamma ray in the spectrum. By starting at the high energy end of the spectrum, the standard source shape may be fitted as shown in Figure 4.4a. In doing this, the associated counts and background may be estimated in the highest energy peak and this contribution subtracted, as shown in Figure 4.4b. In this manner, the spectrum may be unfolded and each peak analysed. The main problem with this method, is that it depends strongly on the resolution of the detector. Very often, peaks in a complex spectrum will be unresolved, making the fitting process difficult. Furthermore, an extensive catalogue of standard sources is necessary and this is not usually available.

Another, more subjective method, involves estimating the background by eye. This method is reported by Abbandano et al.[44]

and uses the fact that, the sum of Compton backgrounds for a complex spectrum, forms an exponentially shaped background. The background line is drawn in using the valleys of the photopeaks as a guide and the counts above this line are then easily estimated. The main problem with this method, is that it depends heavily on the individual skill and integrity of the analyst. For this reason it was decided to use a less subjective method for present work.

There are many computing methods available for unfolding spectra. Such methods have been reported by Heath[45], Heath et al.[46] and Berger[47]. In general, these methods can be made to give high accuracy, for spectra with well resolved peaks. However, the complexity of the computer programmes involved, depends heavily upon the complexity of the spectrum under analysis. Furthermore, the accuracy of the fitting procedures employed, depends upon the resolution of the spectrometer.

For complicated spectra in which peaks are well resolved, a method due to Covell[48] may be employed. A known fraction of the photopeak of interest, is compared with the same fraction of the photopeak, for a standard source of the same gamma energy. (See Figures 4.5a and 4.5b). Taking the same number of channels either side of a_o for the experimental and standard spectrum cases, one obtains the same fractional area. Both A_1 or A_2 may be calculated using the equation:

$$A_1 = a_o + \sum_{n=1}^{n} A_n + \sum_{n=1}^{n} b_n - (n+\tfrac{1}{2})(a_n+b_n)$$

since the area A_2 bears a constant proportionality to the full area under the peak then:

$$A_2 \quad \alpha \quad \frac{G_2\ t_2\ \Omega\ \varepsilon_2}{4\pi}$$

where

G_2 = Gamma ray source emission rate in disintegrations per second

ε_2 = Efficiency of detector for the standard source photopeak energy

t_2 = Time of accumulation of the standard source spectrum

Ω = Solid angle subtended by the detector at the source.

By the same reasoning, the counts $P(\theta)$, in the photopeak under analysis, will also bear a constant relationship to the fraction A_1:

$$P(\theta) \ \alpha \ A_1$$

dividing the latter equations out gives:

$$P(\theta) = \left(\frac{A_1}{A_2}\right) G_2 t_2 \frac{\Omega}{4\pi} \varepsilon_2$$

A further correction factor may be included if the source available, does not correspond exactly, to the energy of the photopeak under analysis. It can be shown that if the spectrum to be analysed has a peak energy E_1 and the standard source E_2, then the areas A_1 and A_2 will be normalised by multiplying by the ratios of the full width at half maxima, hence:

$$P(\theta) = \left(\frac{A_1}{A_2}\right)\left(\frac{W_2}{W_1}\right) G_2 t_2 \varepsilon_2 \left(\frac{\Omega}{4\pi}\right) \qquad \text{.....4.1}$$

$\left(\frac{W_2}{W_1}\right)$ = ratio of F.W.H.M. for standard source to that of peak in experimental spectrum.

Covell's method relies only upon the digital data output from the pulse height analyser and hence gives an objective method of

spectrum analysis. Furthermore, in the case of LiF spectra, the lithium peak is well resolved from the 1MeV peaks from fluorine, making it an ideal method of analysis for present work. All the parameters in equation (4.1) were readily calculated using a standard ^{137}Cs source to compare the 0.662MeV standard photopeak to the 0.478MeV peak in the LiF spectra. The $(\frac{W_2}{W_1})$ factor was determined using the fact that, the square of the resolution of a NaI(Tl) detector, is very nearly proportional to the inverse of the energy above about 400KeV, as reported by C.D. Zerby et al.[31] Standard sources ^{137}Cs, ^{22}Na and ^{60}Co were used to verify this fact.

In heavy nuclei such as Lead, the nuclear level density is very high and consequently, when excited by 14MeV neutrons, many gamma rays are emitted. The resulting spectra are very complicated and most of the interlevel decay probabilities cannot be found, since peaks cannot be resolved. Under such circumstances, it may be assumed that the spectrum is continuous and an attempt made to determine the total gamma ray production in set energy intervals.

The method of analysis of such spectra is based upon graphical stripping and is illustrated at TID by Nellis et al.[49]
The continuous distribution to the left of a typical photopeak, is more or less flat above about 500KeV. It is possible to establish an empirical relationship between the height of the compton distribution and the counts per channel in the photopeak using the following relationship:

$$\bar{n}_c = \left(\frac{P(\theta)}{\Delta c}\right) K \qquad \text{.....4.2}$$

Δc = width of photopeak at base

$P(\theta)$ = counts in photopeak

$\bar{n}_c$ = average height of distribution to the left of the photopeak

K = constant to be determined.

By using the standard sources ^{137}Cs, ^{22}Na, ^{60}Co and $^{241}Am(\alpha,n)^{9}Be$ the value of K was determined and found to be as given in the following table:

TABLE 4.1:

Tabulation of constants for measurement of P(θ)

ENERGY RANGE (MeV)	K
0.65 - 1	0.85
1 - 2	0.89
2 - 3	0.95
3 - 4	1.0
4 - 5	1.1

P(θ) in eqn. (4.2) was found by approximating the photopeak shape to an isosceles triangle. Δc was found from where the triangle cut the abscissa.

The lead spectra were divided into 0.5MeV intervals. The counts per channel were then estimated in the highest energy interval and equation (4.2) used to obtain the height of the compton distribution to the left of this region. This background was then subtracted in a manner analogous to graphical stripping. The process was repeated until all energy intervals had been analysed.

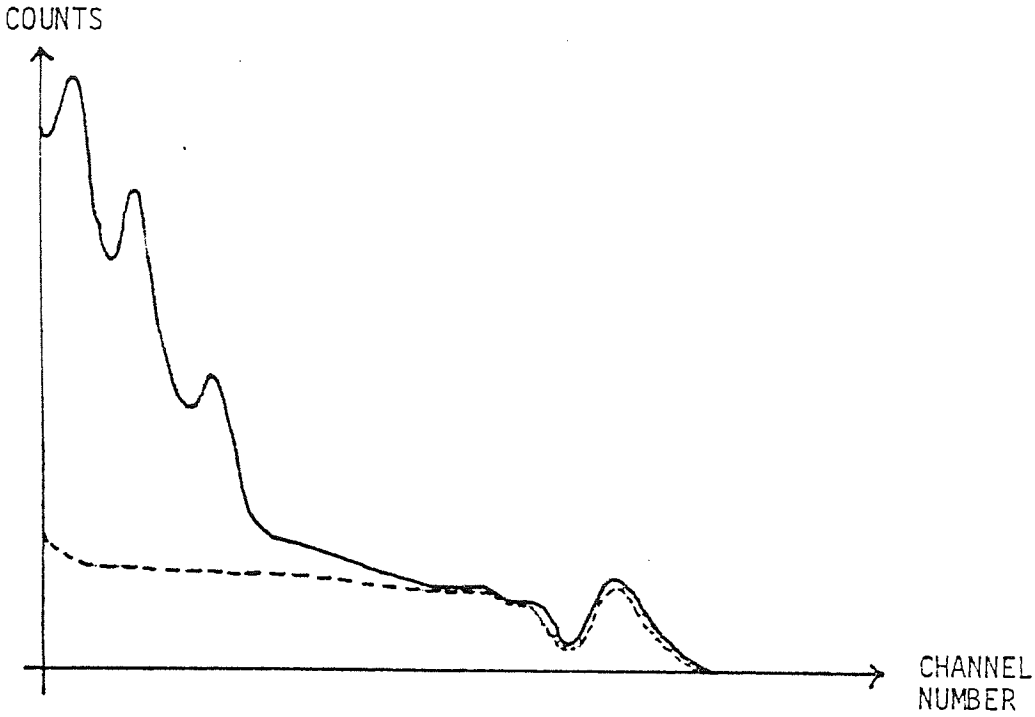

a. FITTING A STANDARD SHAPE AT THE HIGHEST ENERGY GAMMA RAY

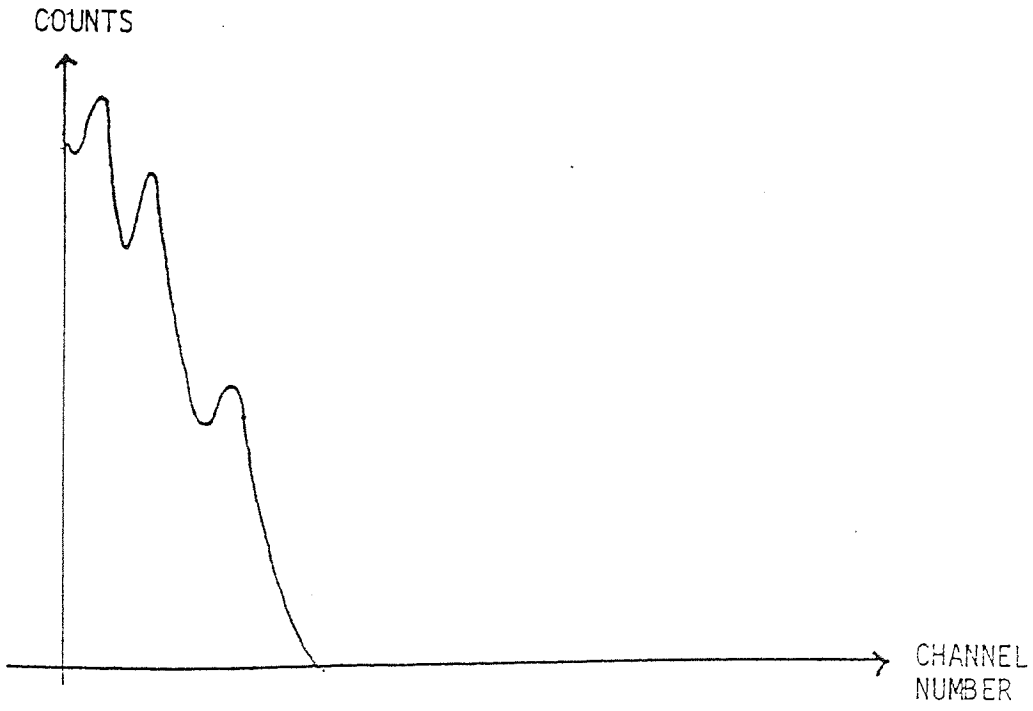

b. HIGHEST ENERGY PEAK STRIPPED OFF

FIGURE 4.4: METHOD OF GRAPHICAL STRIPPING

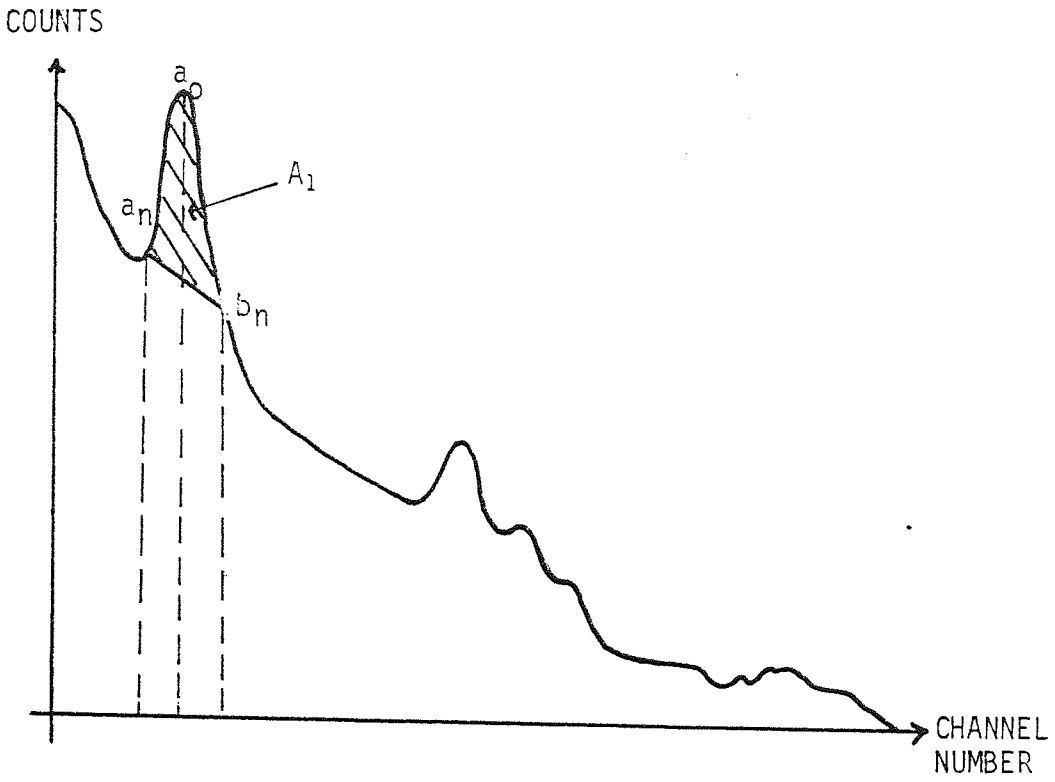

a. SPECTRUM UNDER ANALYSIS

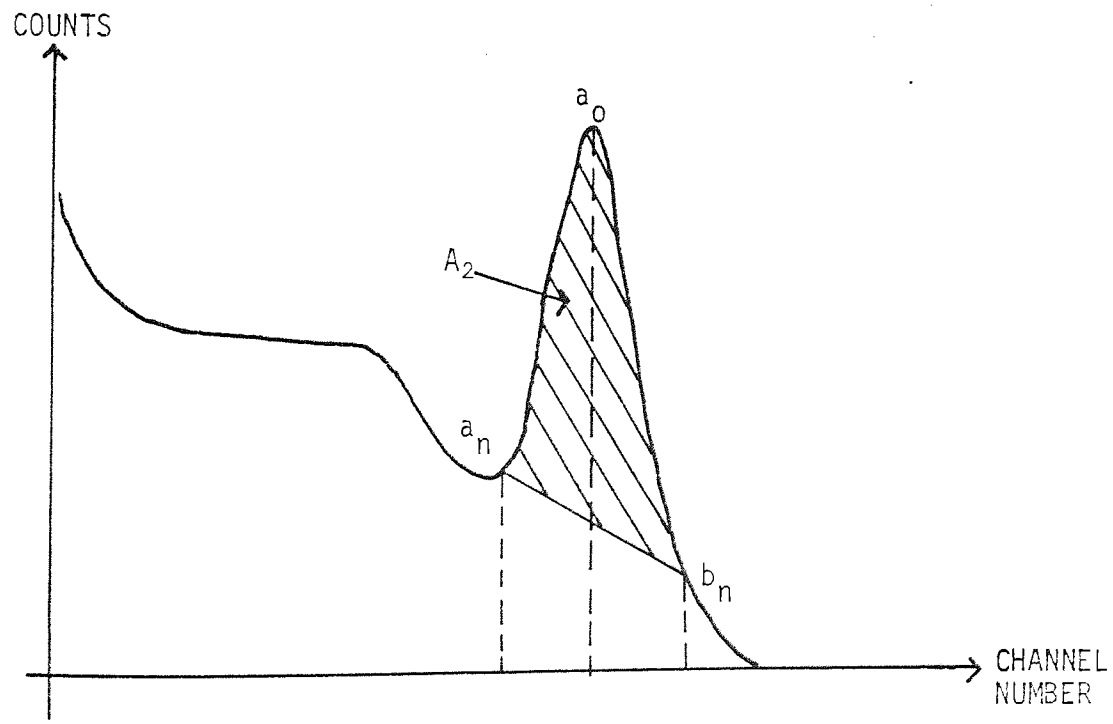

b. STANDARD SOURCE SPECTRUM

FIGURE 4.5 ILLUSTRATION OF COVELL'S METHOD

4.4 Experimental Results Section

The following section contains the experimental results which are both tabulated and illustrated graphically.

The angular distribution data has been fitted to Legendre polynomials of the form:

$$\frac{d\sigma}{d\Omega} = Ao + A_2\cos^2\theta + A_4\cos^4\theta \quad \ldots\ldots\ldots\ldots 4.3$$

This is consistent with the statistical model which predicts the above equation for reactions of the type $A(a,b,\gamma)B$. The fitting procedure and the calculation of error in the coefficient are given in Appendix 2.

Results showing the variation of differential gamma rays production cross-section with sample thickness, have been fitted to an equation of the form:

$$\frac{d\sigma}{d\Omega} = \left(\frac{d\sigma_M}{d\Omega} - \frac{d\sigma_o}{d\Omega} \right) \left(1 - \exp(-\Sigma_T x)\right) + \frac{d\sigma_o}{d\Omega} \quad \ldots\ldots\ldots 4.4$$

where:

$\frac{d\sigma}{d\Omega}$ = Differential gamma ray production cross-section at a thickness x

$\frac{d\sigma_M}{d\Omega}$ = Differential gamma ray production cross-section for a theoretically infinitly thick sample

$\frac{d\sigma_o}{d\Omega}$ = Differential gamma ray production cross-section for a theoretically zero thickness sample

Σ_T = Total Macroscopic cross-section

x = sample thickness.

Derivation of the above equation is given in Appendix 3. The fitted parameters are given in the appropriate tables.

4.4.1 Interpretation of LiF spectra

Figure 4.6 shows a typical LiF spectrum. The only gamma ray emitted from ^{7}Li is due to prompt de-excitation of the 0.478 MeV level shown in the energy level diagram of Figure 4.7, due to T. Lauritsen et al.[50] All other ^{7}Li energy levels decay directly by particle emission when excited with 14MeV neutrons. The 0.478MeV photopeak is the most prominent feature of the LiF spectrum and is well separated from any gamma ray lines emitted from the Fluorine. The most probably gamma rays emitted from Fluorine are shown on the spectrum and have been deduced from the energy level diagram of Figure 4.8 (ref. (51)). Although ^{6}Li is a natural isotope of lithium, its abundance is only 7.42% and no gamma rays due to this were observed.

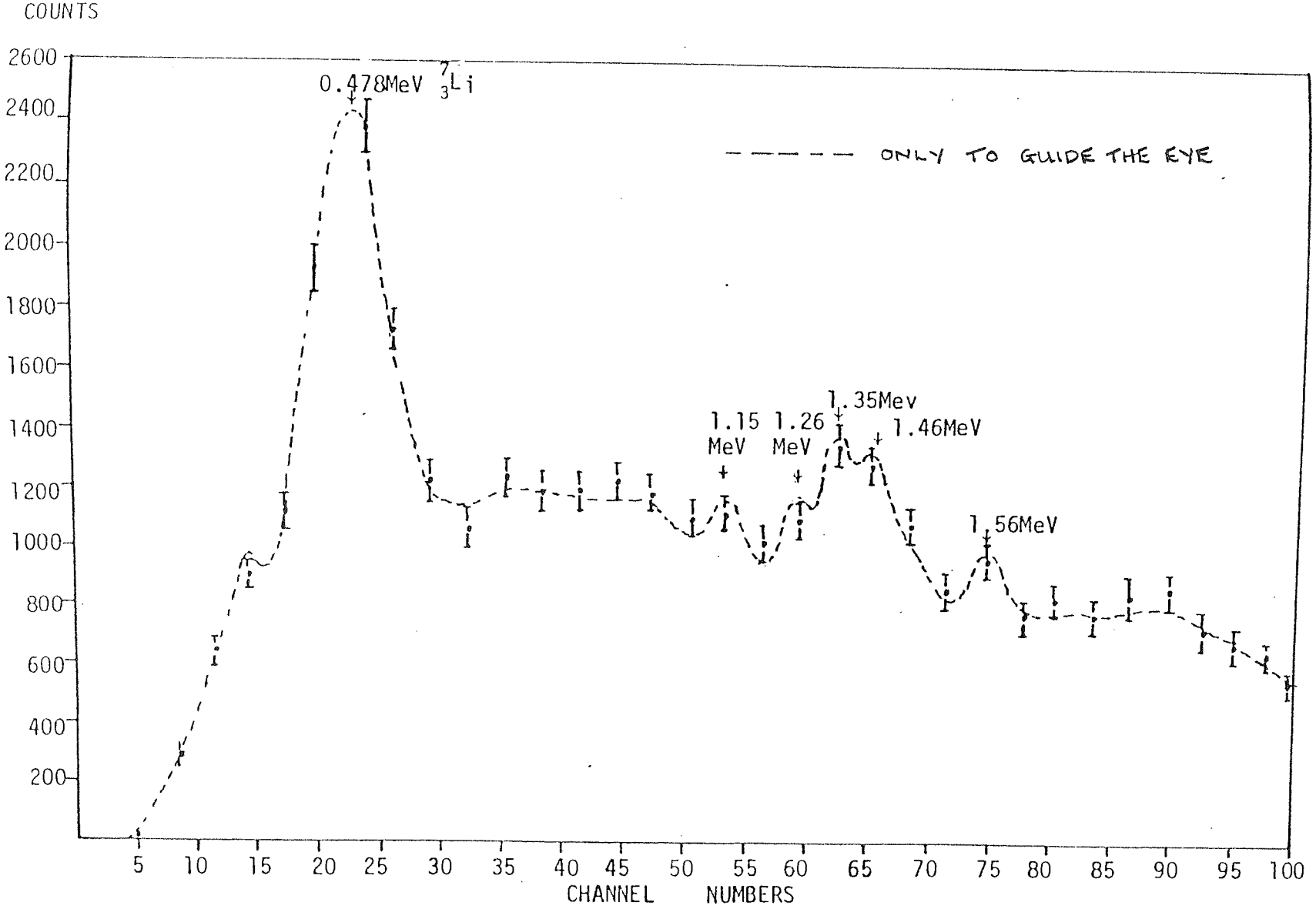

FIGURE 4.6 TYPICAL LiF SPECTRUM FOR 9CM SAMPLE AT 60 DEG.

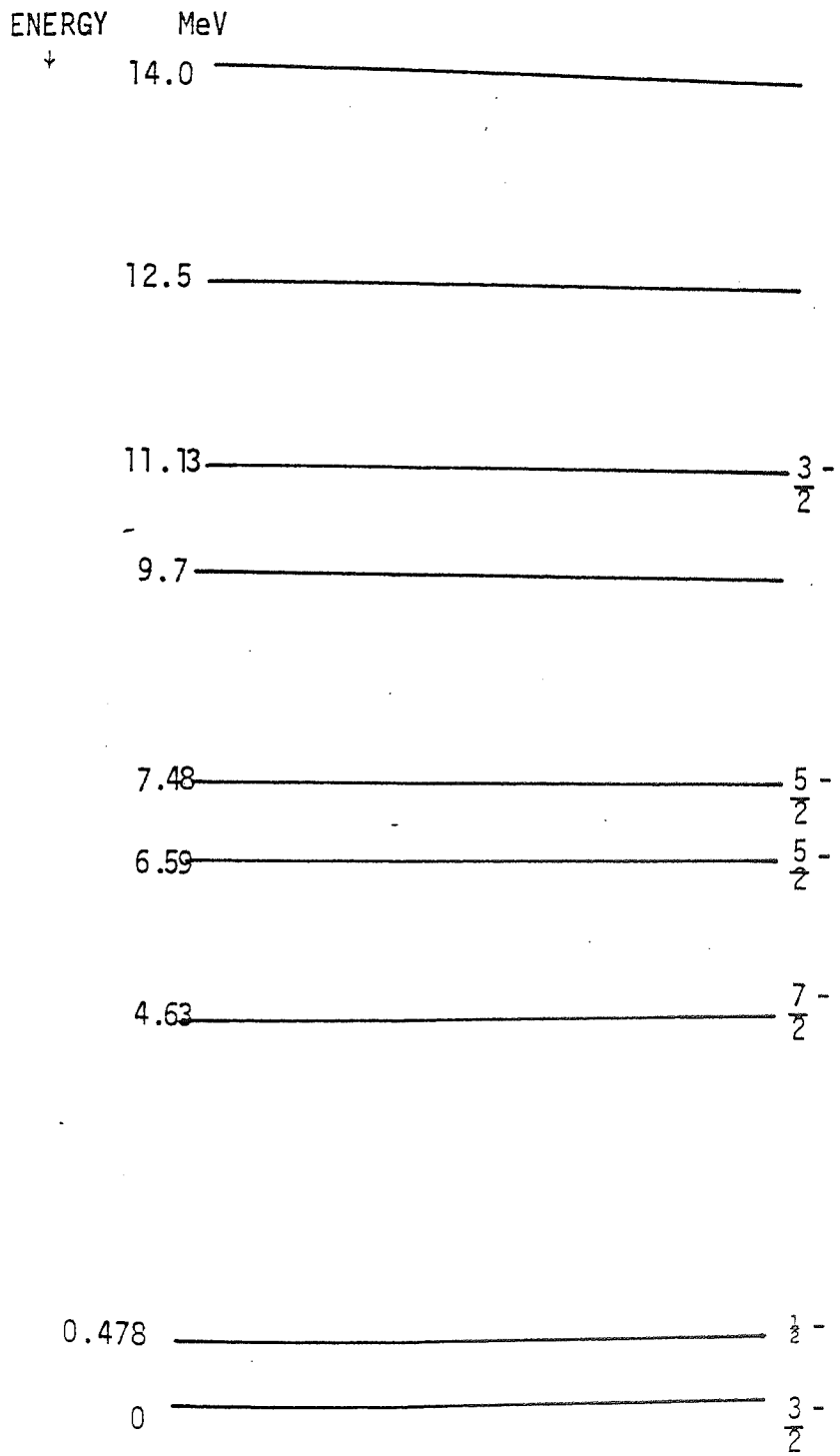

FIGURE 4.7 LEVEL STRUCTURE OF ^{7}Li (Ref. 50)

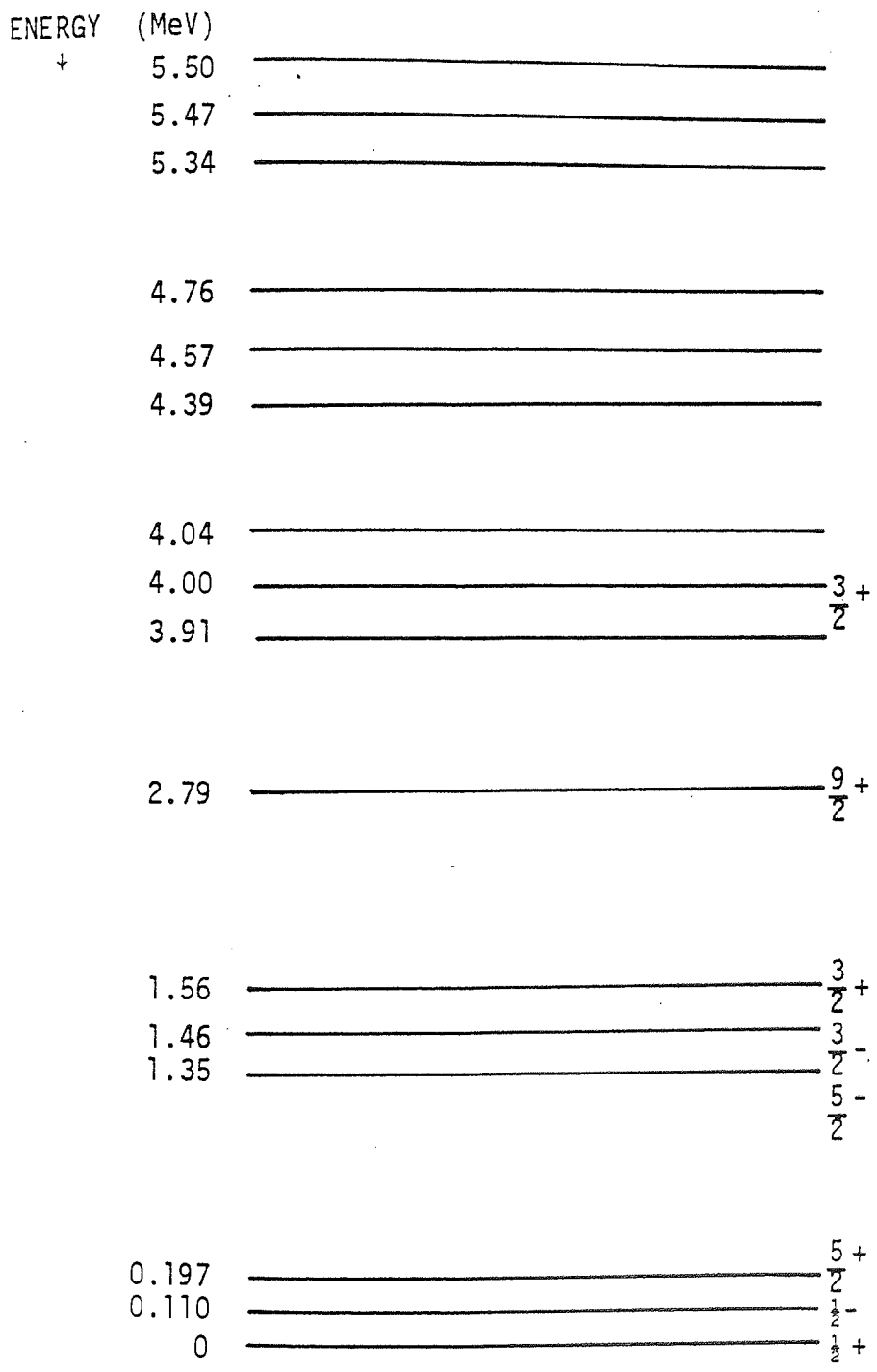

FIGURE 4.8 LEVEL STRUCTURE OF ^{19}F (Ref. 51)

SAMPLE THICKNESS LiF		DIFFERENTIAL CROSS-SECTION A 90° FOR 0.478MeV LEVEL IN ^{7}Li
(cm)	(m.f.p.)	
4	0.31	9.1 ± 1.0
9	0.77	11.2 ± 1.2
13	1.16	14.1 ± 1.6
17	1.42	15.9 ± 1.8
22	1.8	17.2 ± 2.0

FITTING PARAMETERS:

$\frac{d\sigma_M}{d\Omega} = 19.3$

$\frac{d\sigma_o}{d\Omega} = 4.3$

TABLE 4.2 VARIATION OF GAMMA RAY PRODUCTION CROSS-SECTION OF ^{7}Li WITH THICKNESS OF SAMPLE

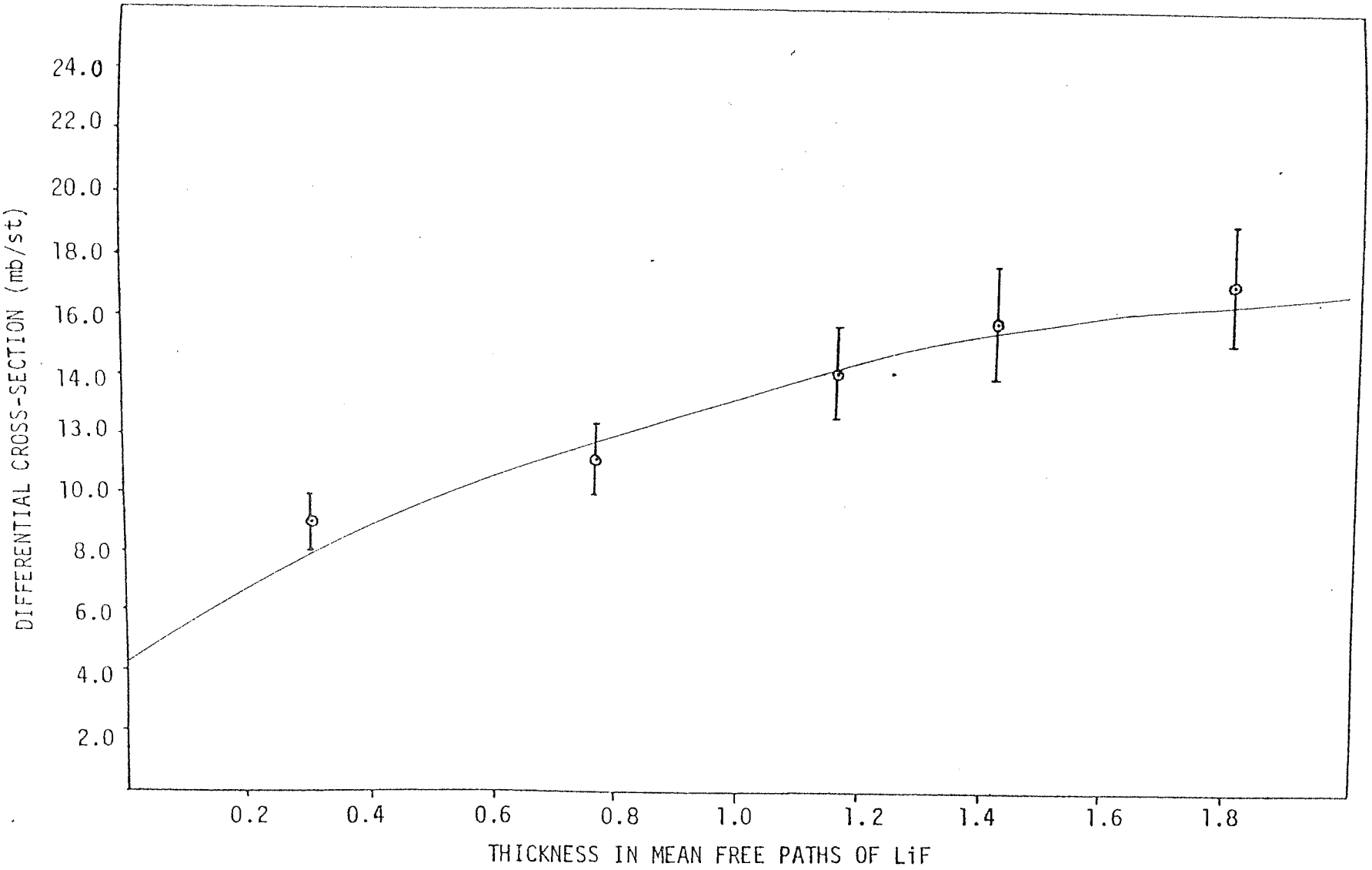

FIGURE 4.9 VARIATION OF MEASURED CROSS-SECTION WITH THICKNESS OF LiF SAMPLE

ANGLE (DEGREES)	DIFFERENTIAL CROSS-SECTION FOR 0.478MeV LEVEL IN ^{7}Li (mb/st)
30	9.1 ± 1.2
45	10.1 ± 1.4
60	9.1 ± 1.2
75	9.3 ± 1.2
90	9.1 ± 1.2

TABLE 4.3 TABULATED EXPERIMENTAL RESULTS FOR 4cm THICK LiF SAMPLE

ANGLE (DEGREES)	DIFFERENTIAL CROSS-SECTION FOR 0.478MeV LEVEL IN ^{7}Li (mb/st)
30	10.5 ± 1.4
45	10.8 ± 1.4
60	11.7 ± 1.6
75	11.4 ± 1.5
90	11.2 ± 1.5

TABLE 4.4 TABULATED EXPERIMENTAL RESULTS FOR 9cm THICK LiF SAMPLES

ANGLE (DEGREES)	DIFFERENTIAL CROSS-SECTION FOR 0.478MeV LEVEL IN ^{7}Li (mb/st)
30	20.2 ± 2.6
45	23.8 ± 2.9
60	20.6 ± 2.8
75	21.4 ± 2.5
90	17.2 ± 2.1

TABLE 4.5 TABULATED ANGULAR DISTRIBUTION FOR 22cm LiF SAMPLES

LEGENDRE COEFFICIENTS	SAMPLE THICKNESS		
	4cm	9cm	22cm
$A_o \pm \alpha_o$	9.2 ± 2.1	11.3 ± 0.8	18.8 ± 5.6
$A_2 \pm \alpha_2$	-1.7 ± 5.6	1.3 ± 1.5	28.5 ±15
$A_4 \pm \alpha_4$	3.9 ± 7.3	-3.2 ± 2.9	-37.5 ±19

TABLE 4.6 LEGENDRE FITTING PARAMETERS FOR LiF ANGULAR DATA

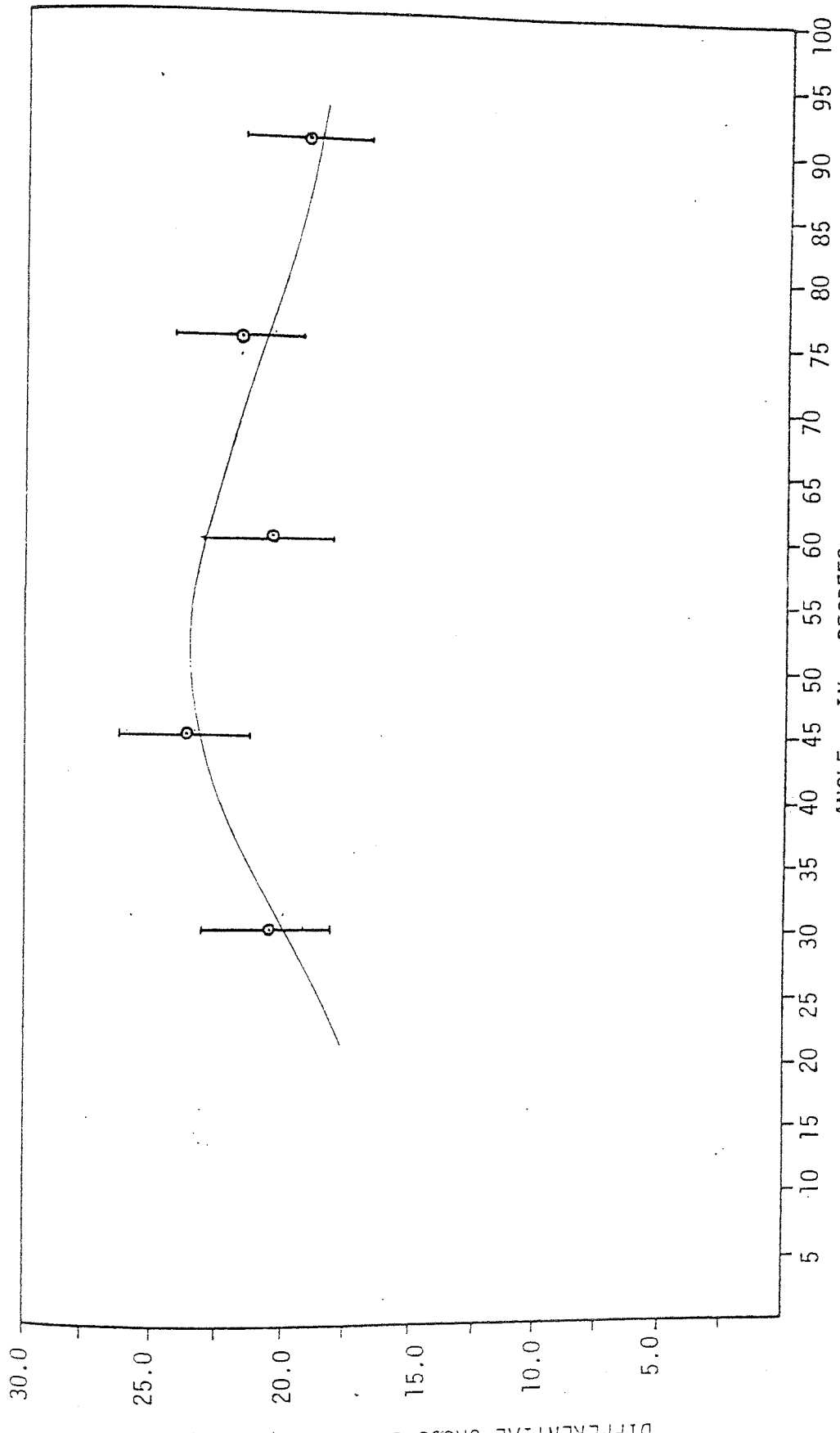

FIGURE 4.10 ANGULAR DISTRIBUTION FOR GAMMA RAY PRODUCTION FROM DE-EXCITATION OF THE 0.478 MeV LEVEL IN ^{7}Li USING 22cm THICK LiF SAMPLES

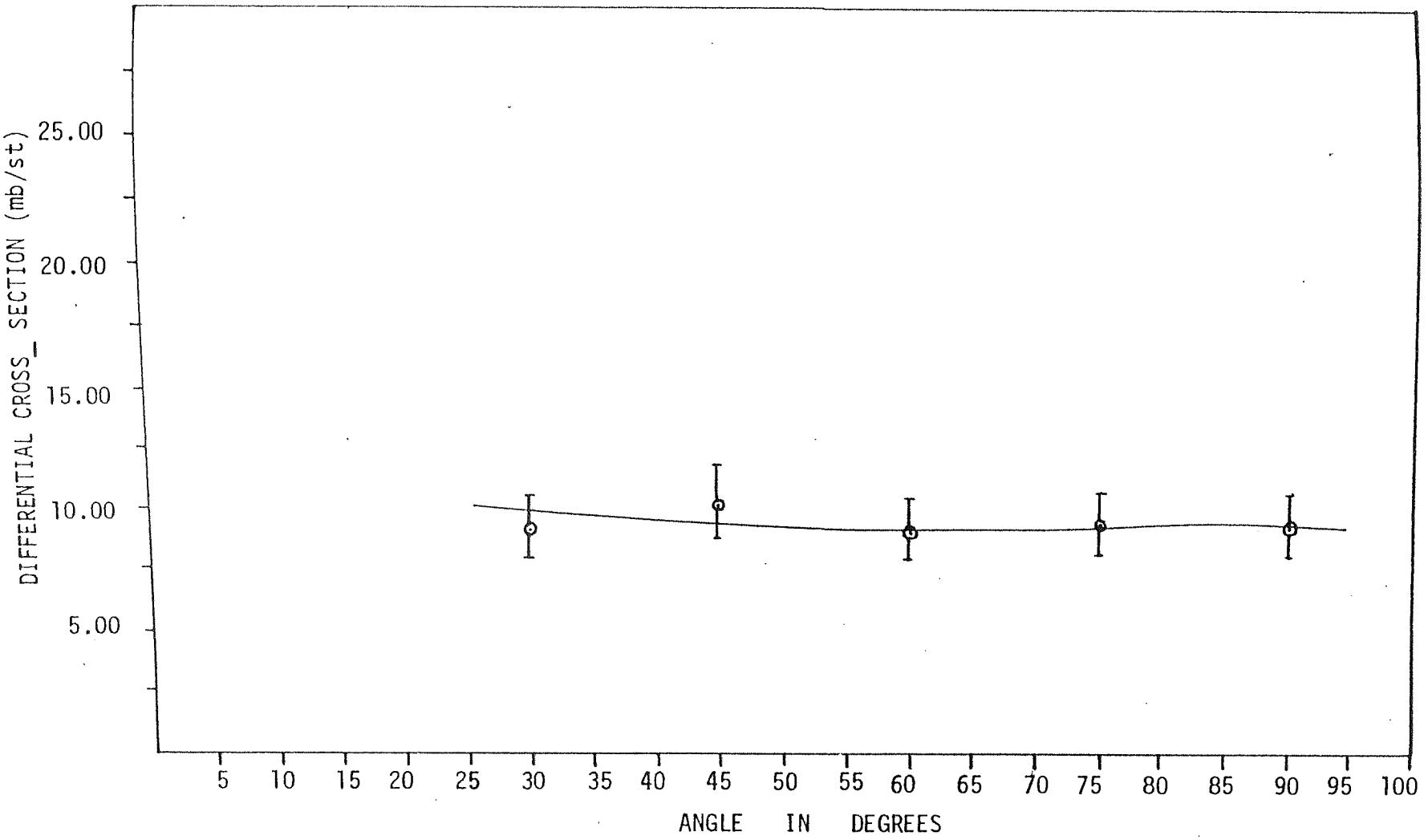

FIGURE 4.11 ANGULAR DISTRIBUTION FOR GAMMA RAY PRODUCTION FROM DE-EXCITATION OF THE 0.478 MeV LEVEL IN ^{7}Li USING 4cm THICK LiF SAMPLES

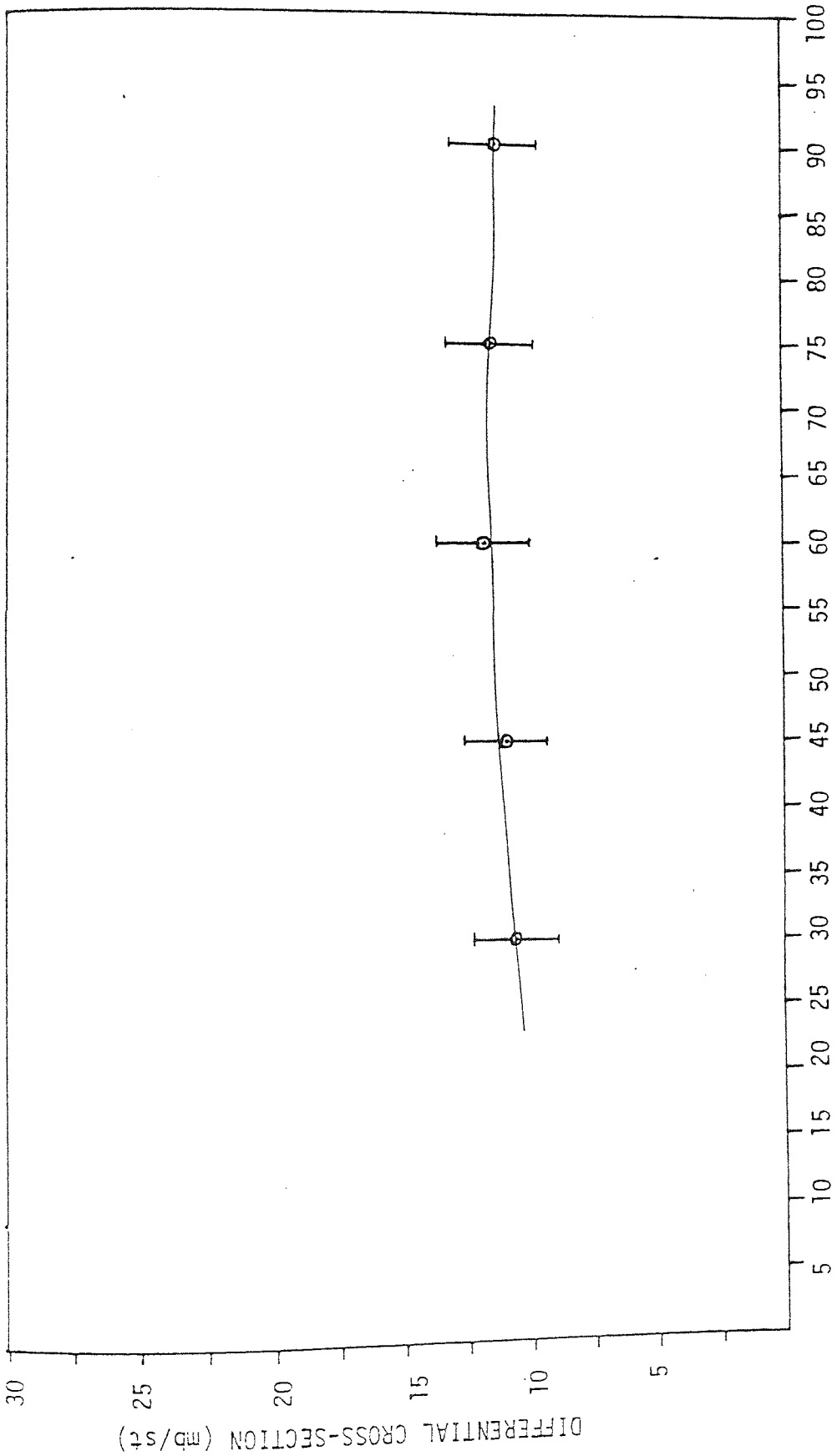

FIGURE 4.12 ANGULAR DISTRIBUTION FOR GAMMA RAY PRODUCTION FROM DE-EXCITATION OF THE 0.478 MeV LEVEL IN ^{7}Li USING 9cm THICK LiF SAMPLES

4.4.2 Discussion of results for LiF

The 0.478 MeV level in ^{7}Li has a threshold of 0.547 MeV and decays by prompt gamma ray emission directly to the ground state. The internal conversion coefficient is negligible and since $\Delta J = 1$ with no parity change for this transition, then magnetic dipole radiation will be emitted. This type of gamma radiation is not in general very directional, having such a low multipole moment and since $J^{\pi} = \frac{1}{2}^{-}$ then $L = 0$ for this level and an isotropic angular distribution would be expected.

In general the results agree with the conclusion as shown in Figures 4.10 - 4.12. Even as the sample thickness is increased, the isotropy remains. The fourth order polynomial fitting is intended for use in interpolating the experimental data.

All other published work concerning the Lithium gamma ray production cross-section assumes isotropy for the 0.478 MeV gamma ray. Results are only available at 90°. For comparison, the 4cm (0.31 mfp) "thinnest" sample used in present work was too thick to exclude multiple scattering. However, Day[9] has shown that multiple scattering is negligible below about 0.2 mean free paths. Hence, by extrapolating the curve of Figure 4.9 to 0.2 mfp's a comparison between present data and other workers may be made. The following table illustrates this:

4.4.3 Comparison of thin sample gamma ray production cross-section at 90°

REFERENCE	$\frac{d\sigma}{d\Omega}$ (mb/st)
MORGAN (52)	5.3 ± 0.6
ORNL (53)	8.0 ± 1.6
ENDF/B AT. 416/(54)	6.0 ± (NO ERROR QUOTED)
PRESENT WORK	6.6 ± 0.9

In general the results agree with each other to within the quoted experimental uncertainties.

The results of ORNL[53] seem a little high in comparison to the average value of 6.5 mb/st. One possible reason, is that thick samples of LiF were used in this work and although corrections were made for multiple scattering, it is possible that these were not enough. However, the experimental uncertainty quoted keeps the result within the range of both the average value and present work. The work of Morgan [52] is a little low compared to the other results. The reason for this is not obvious since the experimental uncertainty quoted is low.

The variation of measured cross-section with sample thickness is dealt with in the theoretical Chapter 5.

4.4.4 Interpretation of Lead Spectra

Lead has four isotopes which are listed below along with the relative abundances of each:

$^{204}_{82}Pb$	1.4%	(2.6 MeV alpha decay $T_{\frac{1}{2}} = 4.42 \times 10^{25}$ sec)
$^{206}_{82}Pb$	23.6%	
$^{207}_{82}Pb$	22.6%	
$^{208}_{82}Pb$	52.3%	

The known energy levels of the three main isotopes are very complicated and are shown in Figure 4.13 taken from Ref. ([55]). As a result of this, when 14MeV neutrons are used to excite natural lead samples, the spectrum of gamma rays contains many unresolved peaks and this is illustrated in the typical gamma ray spectrum for a 15cm sample at 90°. The prominant features of this spectrum are shown in Figure 4.14. The following gives the main decay modes which result in the gamma rays shown in the spectrum.

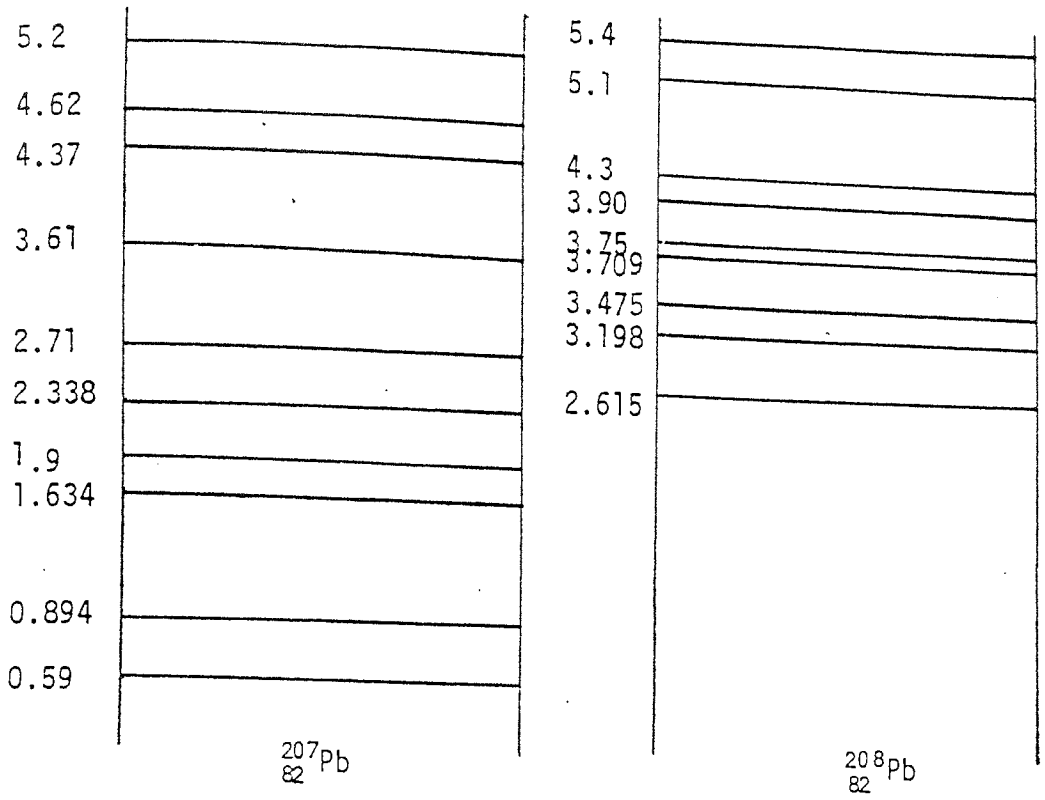

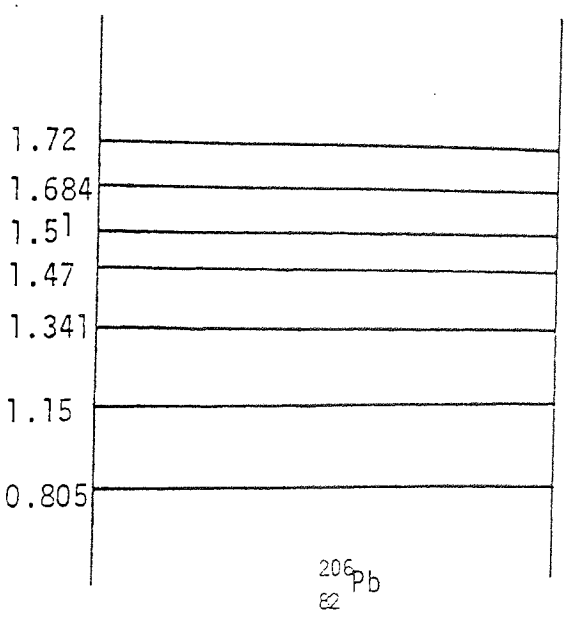

FIGURE 4.13 ENERGY LEVELS IN LEAD ISOTOPES (Ref. 55)

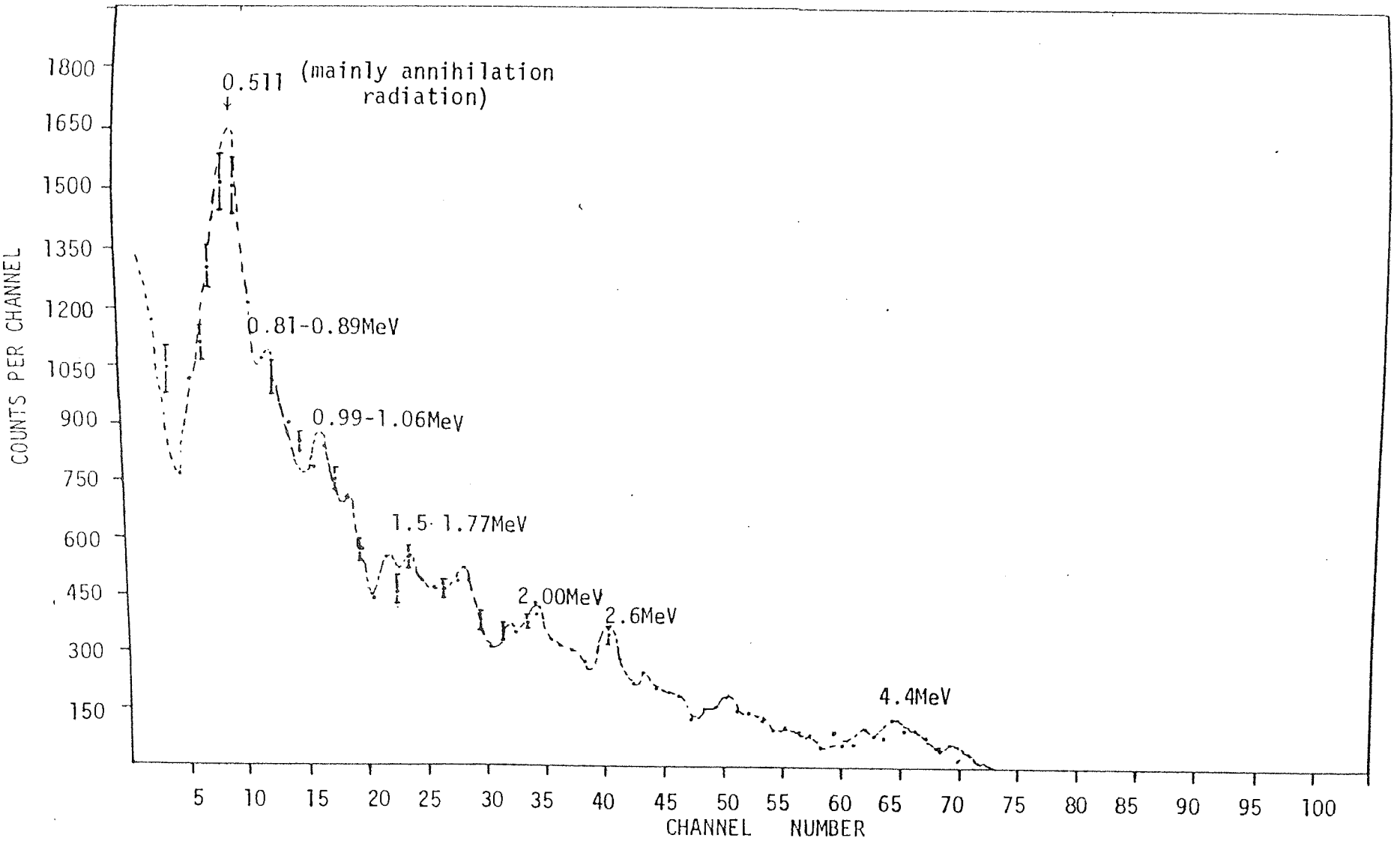

FIGURE 4.14 GAMMA RAY SPECTRUM FROM 15cm LEAD SAMPLE AT 90°

SAMPLE THICKNESS		DIFFERENTIAL CROSS-SECTION AT FOLLOWING ENERGY RANGES (mb/st)				
(cm)	(m.f.p)	0.65 - 1MeV	1 - 2MeV	2 - 3MeV	3 - 4MeV	4 - 5MeV
2.7	0.48	101 ± 16	130 ± 18	118 ± 18	28 ± 8	26 ± 6
5.0	0.89	97 ± 16	179 ± 16	126 ± 16	54 ± 10	26 ± 6
10.0	1.79	140 ± 20	189 ± 14	122 ± 17	81 ± 12	49 ± 8
15.0	2.68	146 ± 18	208 ± 18	145 ± 16	84 ± 10	56 ± 10
20.0	3.57	129 ± 18	230 ± 18	144 ± 16	82 ± 11	58 ± 9
25.0	4.46	148 ± 17	192 ± 17	136 ± 16	85 ± 10	56 ± 8

TABLE 4.7 TABULATED DIFFERENTIAL CROSS-SECTIONS FOR GAMMA RAY PRODUCTION AND ITS VARIATION WITH THICKNESS OF LEAD SAMPLES

ENERGY RANGE (MeV)	FITTING PARAMETERS (mb/st)	
	$\frac{d\sigma}{d\Omega}$	$\frac{d\sigma M}{d\Omega}$
0.65 - 1	60.6	146.7
1 - 2	92.2	214.4
2 - 3	102.5	140
3 - 4	-3.46	92.9
4 - 5	1.5	57.8

TABLE 4.8 FITTING PARAMETERS FOR LEAD SAMPLES

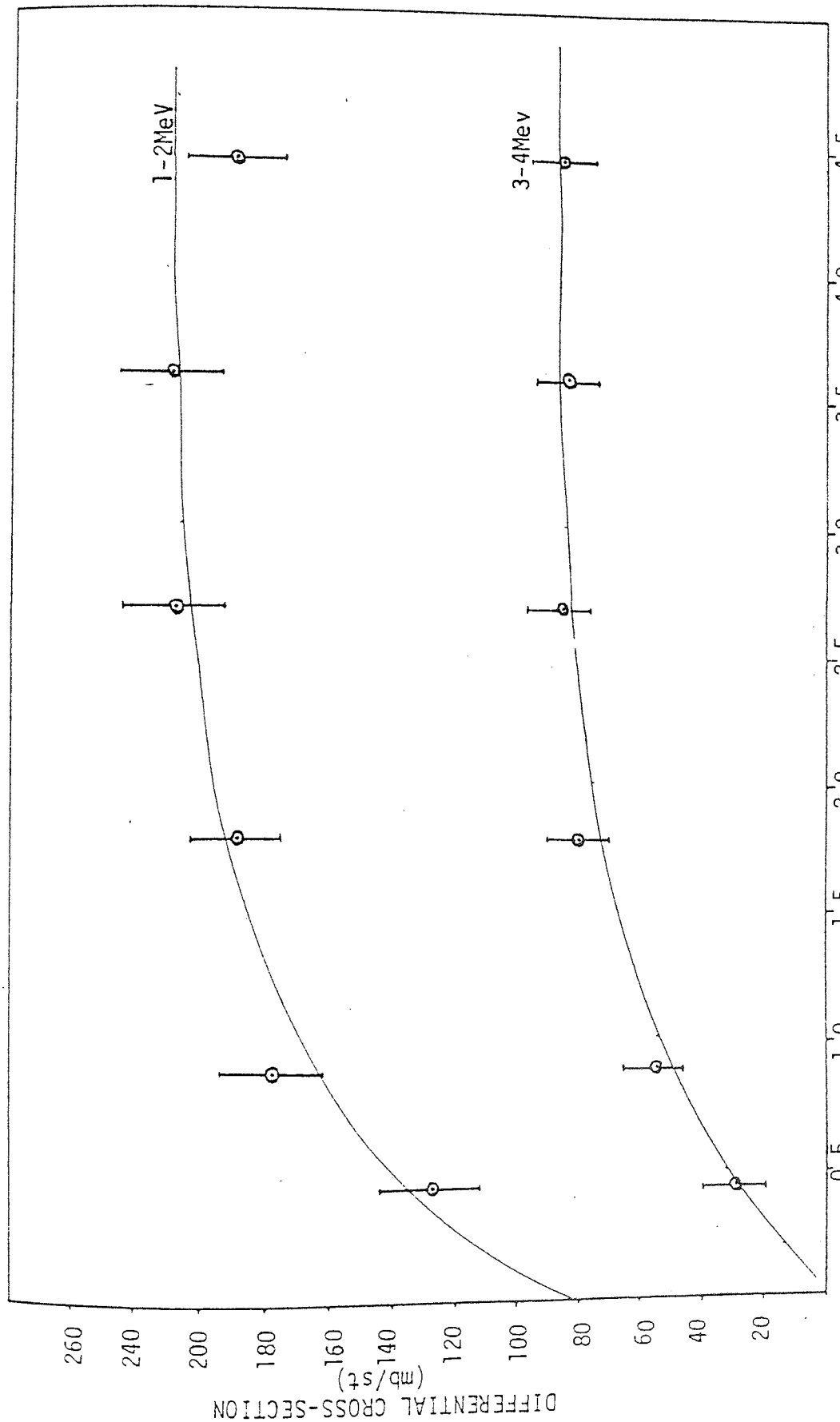

FIGURE 4.15 VARIATION OF MEASURED DIFFERENTIAL CROSS-SECTION WITH THICKNESS OF LEAD SAMPLES FOR THE GAMMA RAY ENERGIES ILLUSTRATED

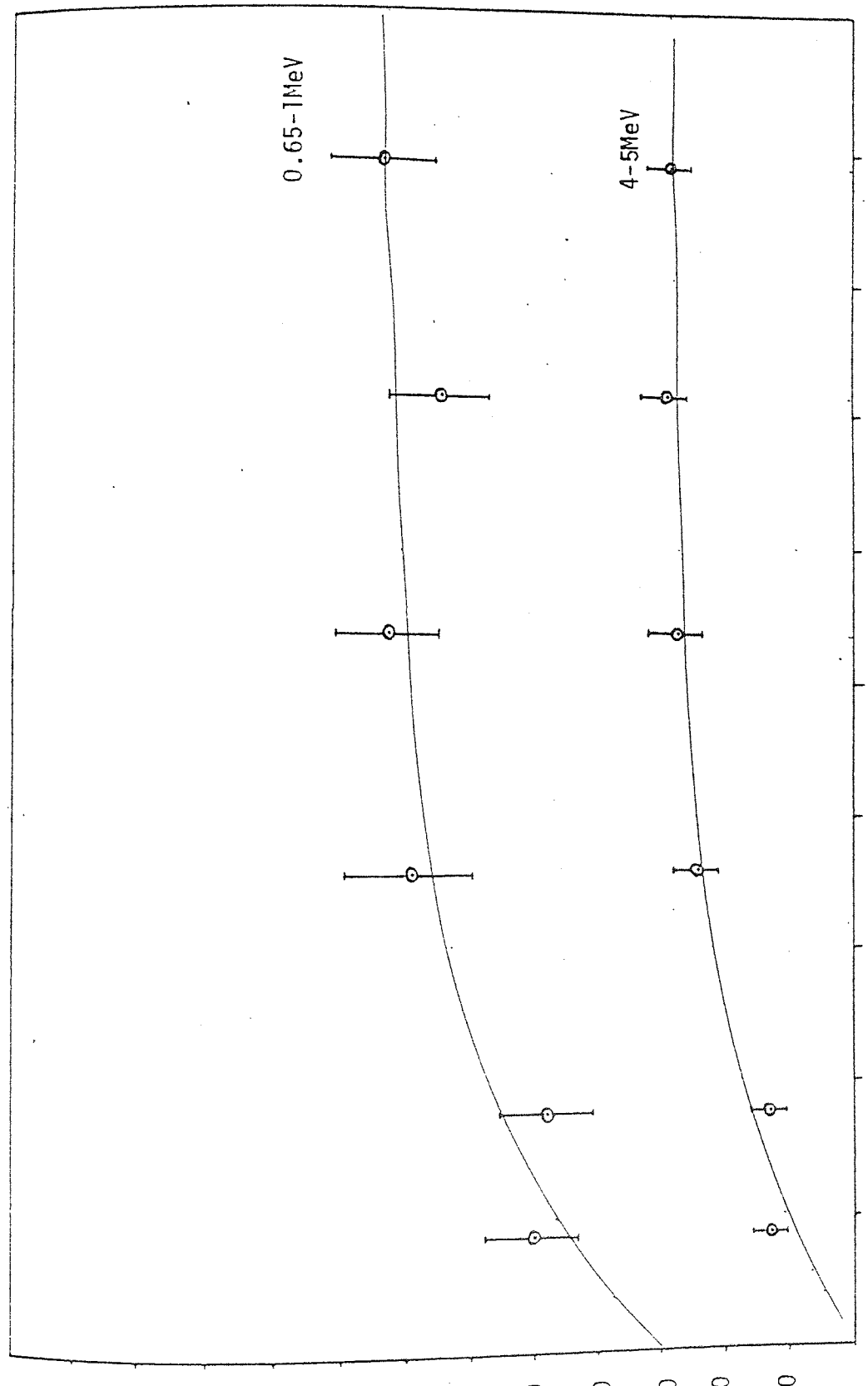

FIGURE 4.16 VARIATION IN MEASURED CROSS-SECTION WITH THICKNESS OF LEAD SAMPLES FOR THE GAMMA RAY ENERGIES ILLUSTRATED

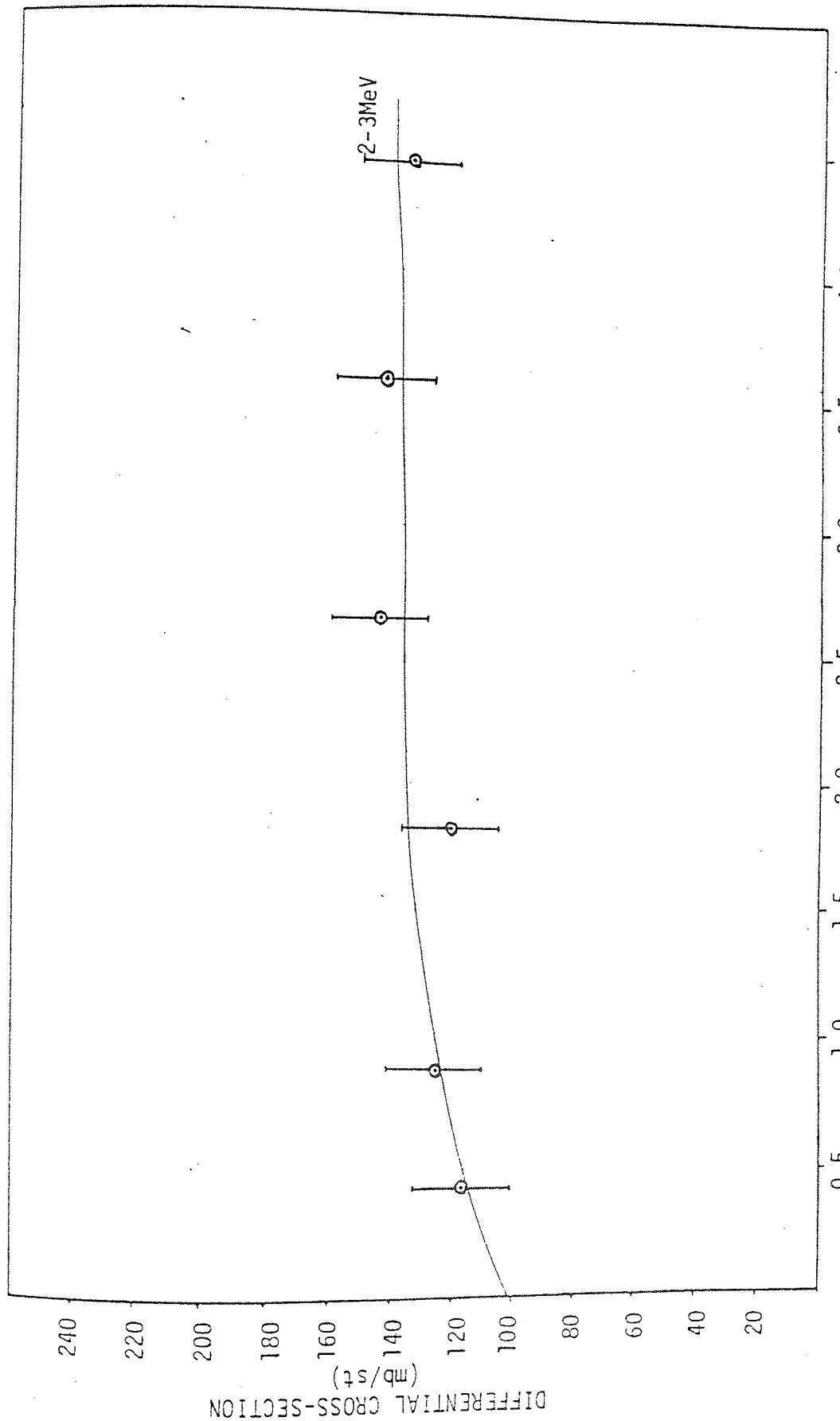

FIGURE 4.17 VARIATION IN MEASURED CROSS-SECTION WITH THICKNESS OF LEAD SAMPLES FOR THE 2.3MeV GAMMA RAY ENERGY GROUP

ANGLE (DEGREES)	DIFFERENTIAL CROSS-SECTION PER MeV (mb/st)				
	0.65 - 1MeV	1 - 2MeV	2 - 3MeV	3 - 4MeV	4 - 5MeV
30	96 ± 10	125 ± 15	107 ± 15	41 ± 6	36 ± 6
45	84 ± 10	120 ± 14	115 ± 16	30 ± 7	23.5 ± 6.5
60	100 ± 10	114 ± 15	127 ± 16	29 ± 6	20 ± 7.0
75	103 ± 12	117 ± 16	90 ± 18	56 ± 7	26 ± 4.0
90	101 ± 16	130 ± 18	118 ± 18	28 ± 8	26 ± 6.0

TABLE 4.9 TABULATED ANGULAR DISTRIBUTIONS FOR GAMMA RAY PRODUCTION IN 2.7cm LEAD SAMPLES

LEGENDRE COEFFICIENTS FOR 2.7cm SAMPLE	ENERGY RANGE				
	0.65 - 1MeV	1 - 2MeV	2 - 3MeV	3 - 4MeV	4 - 5MeV
$A_0 \pm \alpha_0$	104 ± 15	135 ± 4	105 ± 40	41 ± 15	27 ± 3.2
$A_2 \pm \alpha_2$	-54 ± 42	-57 ±	54 ±109	-47 ± 40	-45 ±10
$A_4 \pm \alpha_4$	55 ± 55	87 ±	-63 ±141	60 ± 52	76 ±12
LEGENDRE COEFFICIENTS FOR 10cm SAMPLE	ENERGY RANGE				
	0.65 - 1MeV	1 - 2MeV	2 - 3MeV	3 - 4MeV	4 - 5MeV
$A_0 \pm \alpha_0$	136 ± 15	180 ± 24	117 ± 21	77 ± 8.8	55 ± 19
$A_2 \pm \alpha_2$	-88 ± 40	-108 ± 65	-31 ± 57	-31 ± 24	150 ± 51
$A_4 \pm \alpha_4$	100 ± 52	131 ± 85	40 ± 75	42 ± 30	-136 ± 67

TABLE 4.10 LEGENDRE FITTING PARAMETERS FOR LEAD SAMPLES

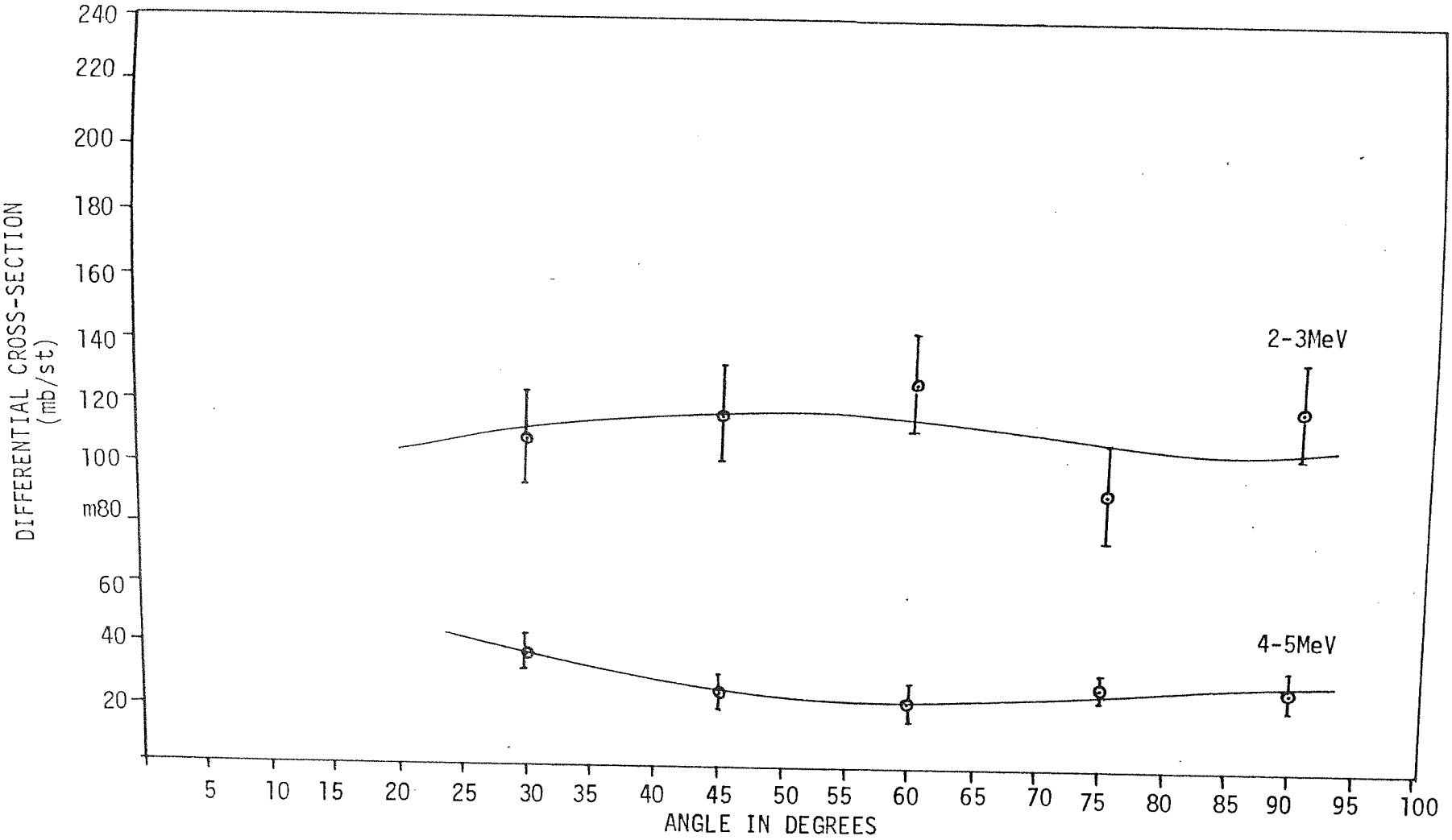

FIGURE 4.18 ANGULAR DISTRIBUTIONS OF 2.7cm THICK LEAD SAMPLES FOR THE GAMMA RAY ENERGY REGIONS SHOWN

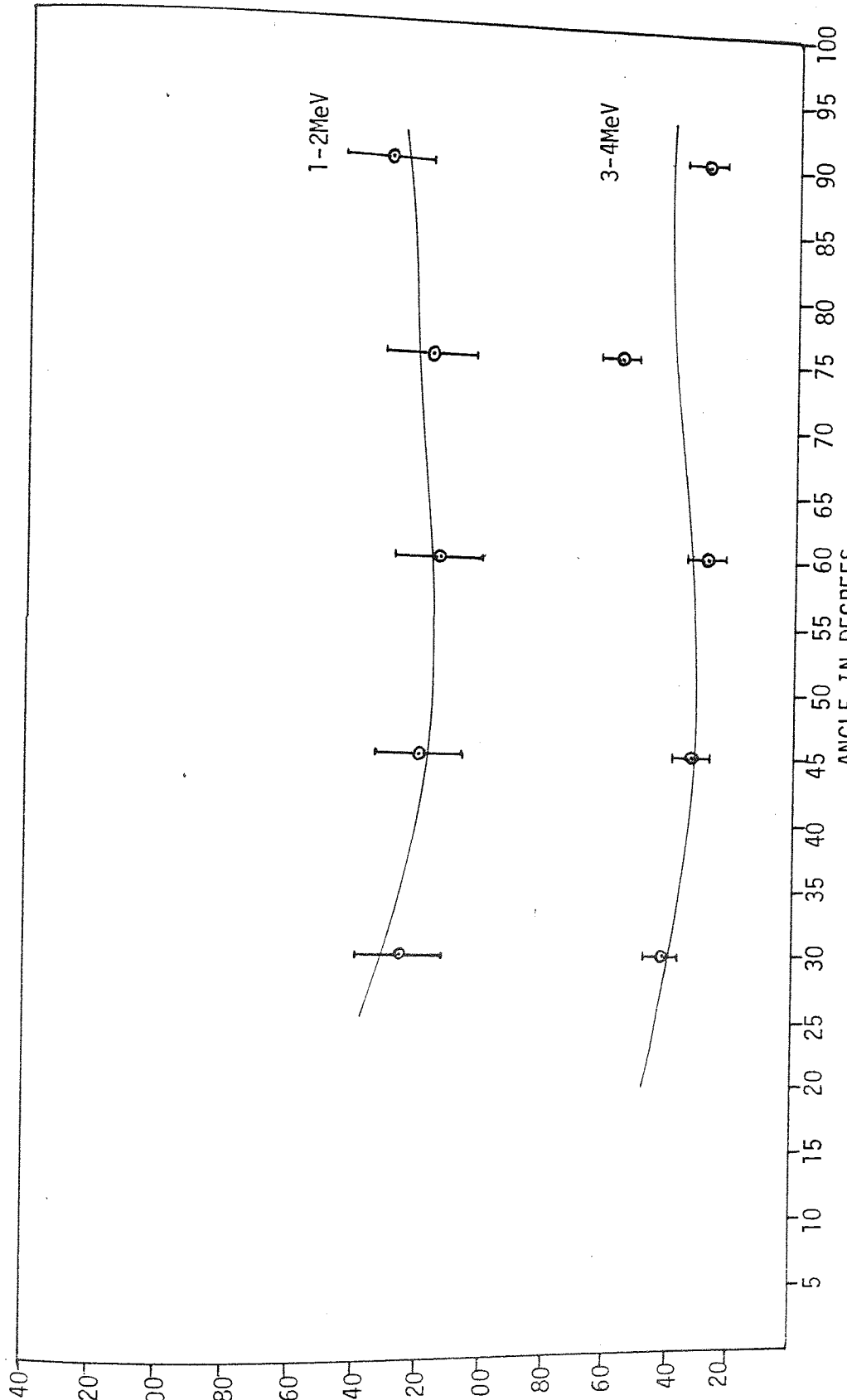

FIGURE 4.19 ANGULAR DISTRIBUTIONS FOR THE 2.7cm LEAD SAMPLE FOR THE GAMMA RAY ENERGY SECTIONS SHOWN

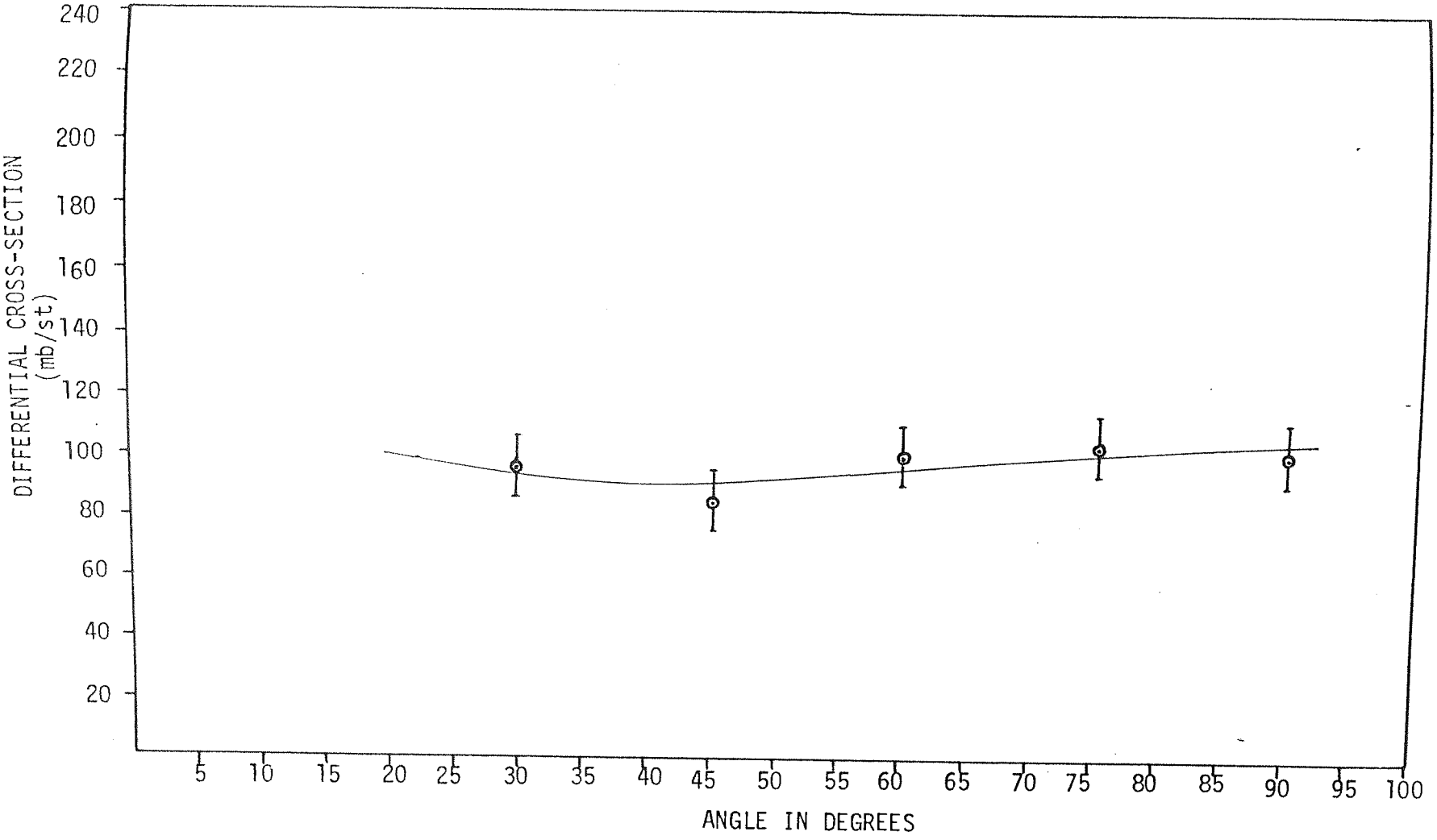

FIGURE 4.20 ANGULAR DISTRIBUTION FOR 2.7cm LEAD SAMPLES FOR THE GAMMA RAY ENERGY GROUP 0.65-1MeV

ANGLE (DEGREES)	DIFFERENTIAL CROSS-SECTION PER MeV (mb/st)				
	0.65 - 1MeV	1 - 2MeV	2 - 3MeV	3 - 4MeV	4 - 5MeV
30	126 ± 18	170 ± 17	115 ± 15	76 ± 12	95 ± 15
45	120 ± 18	163 ± 18	120 ± 16	74 ± 12	88 ± 17
60	113 ± 17	153 ± 15	104 ± 14	68 ± 11	88 ± 16
75	131 ± 20	172 ± 16	112 ± 15	75 ± 12	67 ± 11
90	140 ± 20	189 ± 14	122 ± 17	80 ± 12	49 ± 8

TABLE 4.11 TABULATED ANGULAR DISTRIBUTION FOR GAMMA RAY PRODUCTION IN 10cm LEAD SAMPLES

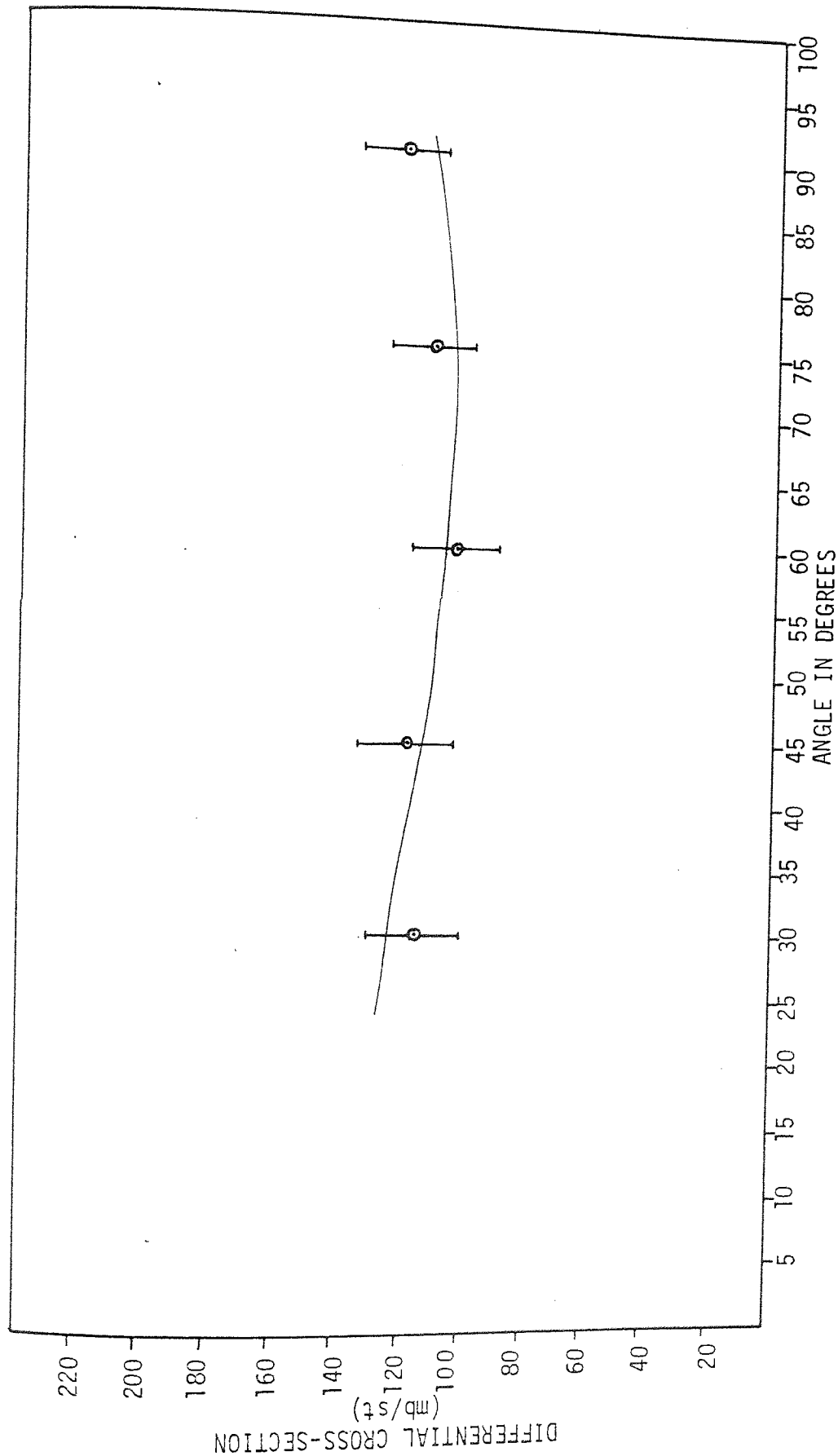

FIGURE 4.21 ANGULAR DISTRIBUTION FOR THE PRODUCTION OF GAMMA RAYS IN THE 2 - 3 MeV REGION FOR 10cm LEAD SAMPLES

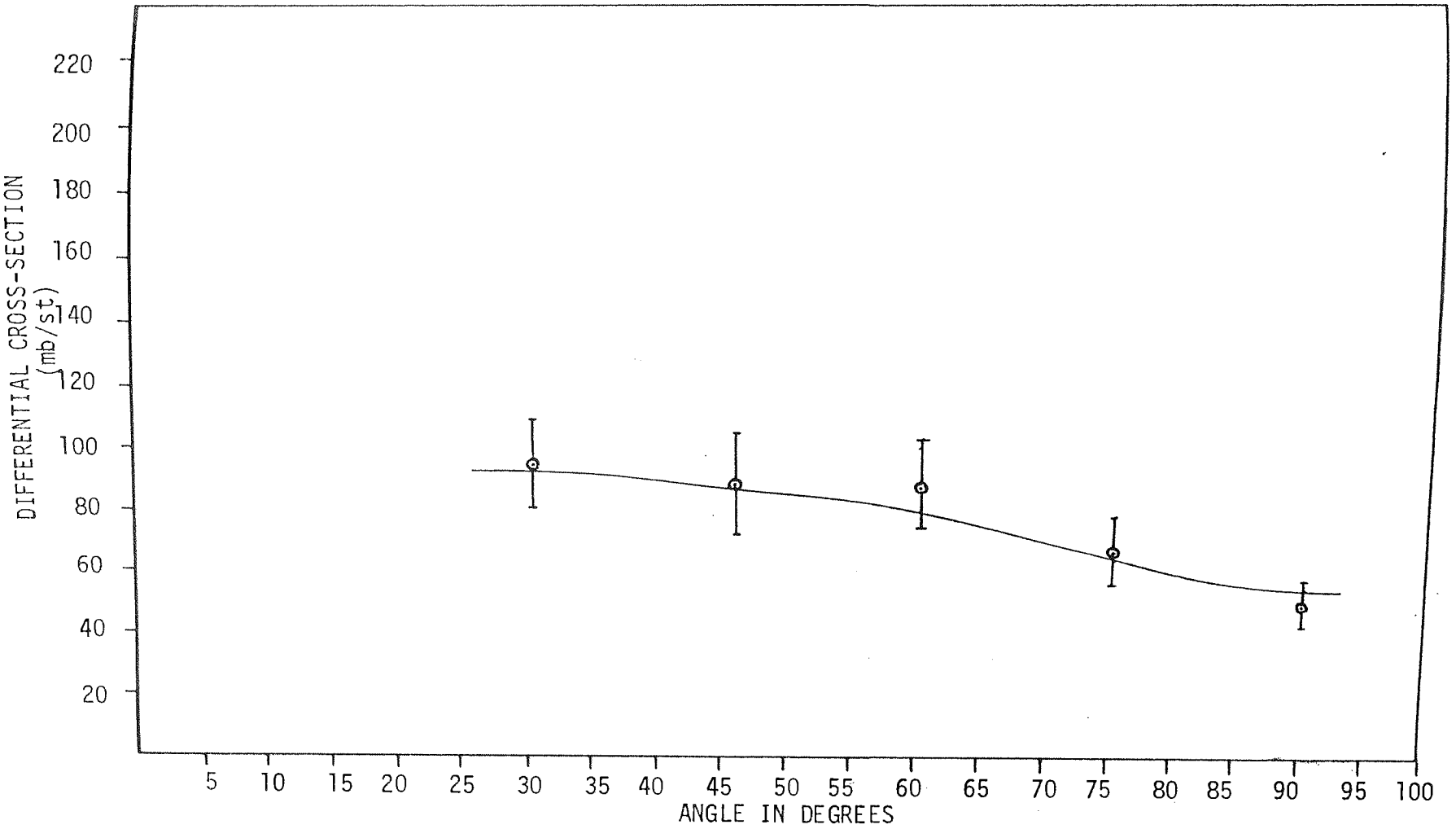

FIGURE 4.22 ANGULAR DISTRIBUTION OF GAMMA RAYS IN THE 4 - 5MeV REGION FOR 10cm THICK LEAD SAMPLES

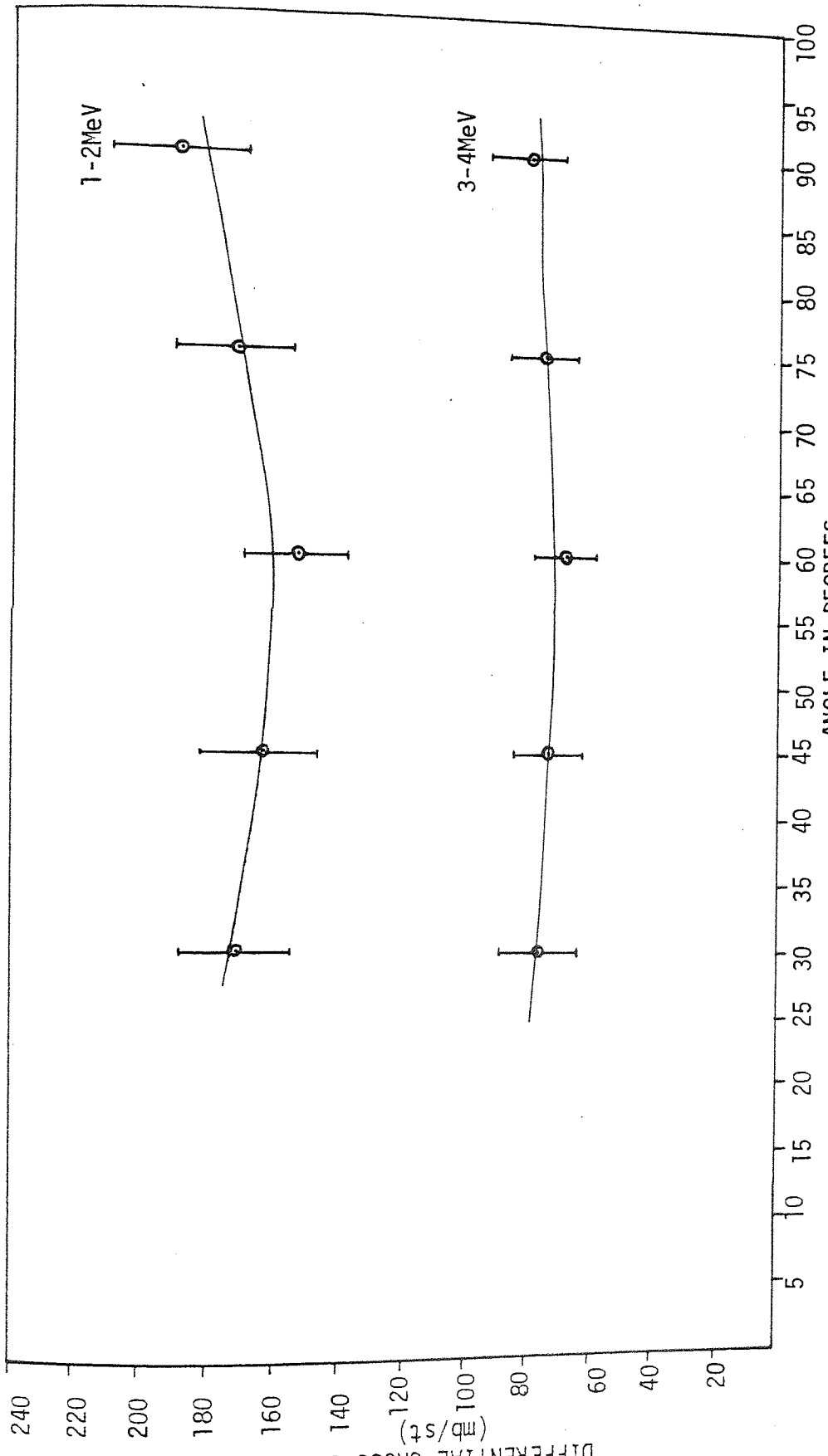

FIGURE 4.23 ANGULAR DISTRIBUTION FOR 10cm LEAD SAMPLES

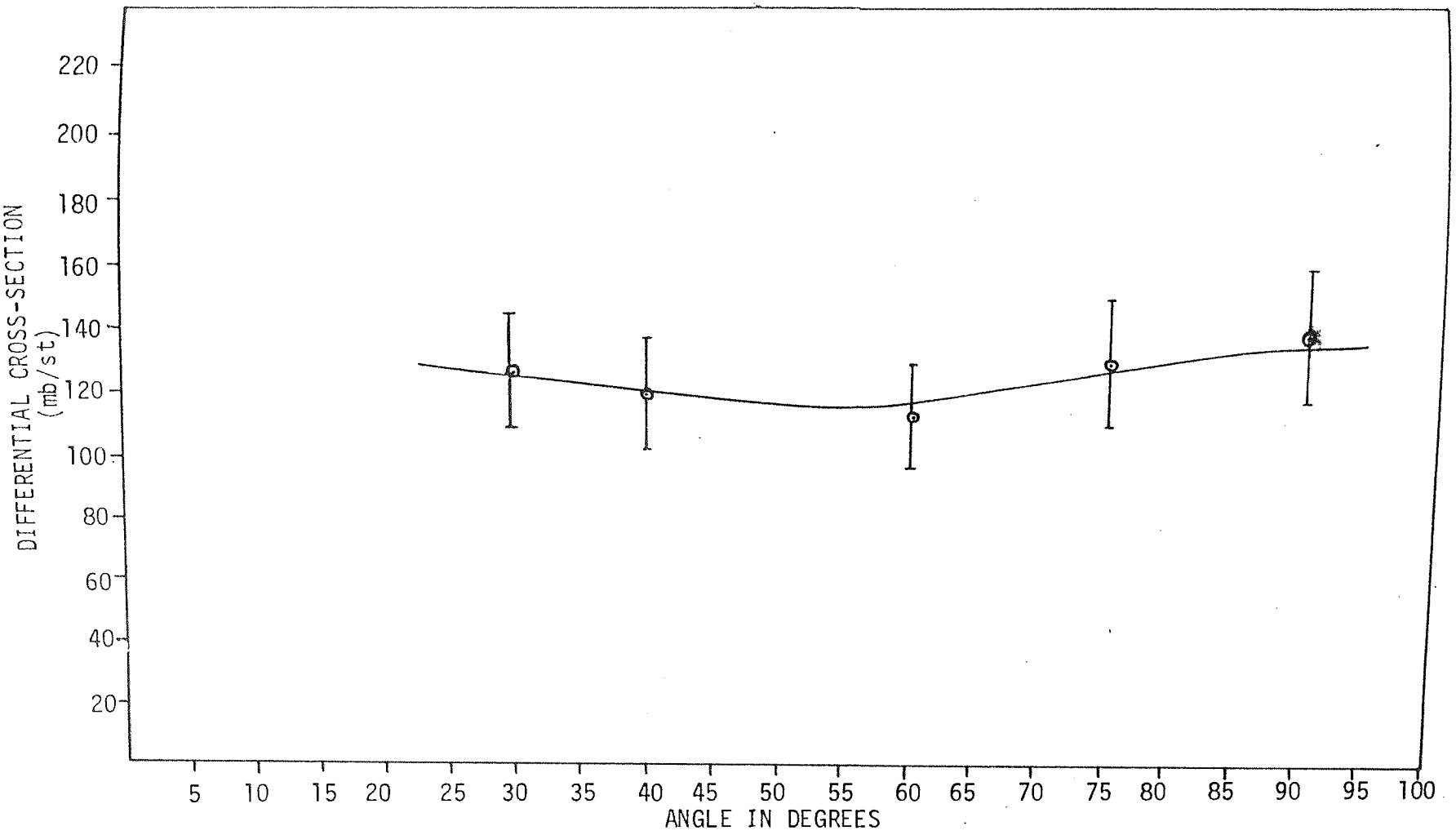

FIGURE 4.24 ANGULAR DISTRIBUTION FOR PRODUCTION OF GAMMA RAYS IN THE 0.65-1MeV REGION IN 10cm THICK LEAD SAMPLES

4.4.5 Discussion of lead results

The complex energy level structure of natural lead makes a theoretical discussion of results very difficult, since for each energy group in which production cross-section was measured, there will be many gamma rays of different multipole moments emitted. Present work indicates that the result of this is to produce isotropic distribution of gamma rays. Anisotropy is observed in the 4 - 5MeV region and this is perhaps expected since in this energy range there would be fewer mixed gamma rays and the higher order spins of the levels would result in higher order multipolarities and thus a more probable anisotropic distribution.

Unfortunately there is very little data available on gamma ray production cross-section from lead, most of the work concentrating on the 2.62MeV gamma emitted from de-excitation of the first level in ^{208}Pb such as refs. (56) and (57).

Engesser et al.[58] has made an attempt to resolve as many gamma rays as possible between 0.5 and 2.62MeV and these results have been summed for each energy region and are shown in the table that follows along with the work of others.

TABLE 4.12 Comparison of data for lead cross-sections

ENERGY RANGE MeV	PRESENT (mb/st)	ENGESSER[58] (mb/st)	SCHERRER[59] (mb/st)	ENERGY RANGE MeV	NELLIS[49] (mb/st)
0.65 - 1	101	90	-	0.85 - 2.84	210
1 - 2	130	85	-	2.84 - 4.09	27.97
2 - 3	118	30	-	4.09 - 5.16	13.26
3 - 4	28	-	-		
4 - 5	26	-	48		
SUM BETWEEN 1 - 5 MeV	302		334		278

The results of Engesser et al.[58] are expectantly lower than present results since only resolvable peaks were measured and summed. Comparison between present data and other workers is best made by considering the total gamma production cross-section between 1 and 5MeV in which all results agree with each other to within ± 10% of an average value of 305mb/st.

The effects of multiple scattering will be dealt with in the next chapter.

Experimental uncertainties

In the formula for $\frac{d\sigma}{d\Omega}$ section 4.3.5 nearly all the quantities involved are of a statistical nature with errors mainly due to counting statistics. It is common to evaluate the errors by adding in quadrature according to the general formula:

$$\text{ERROR } (\%) = \pm \sqrt{\frac{\alpha_1^2}{N_1} + \frac{\alpha_2^2}{N_2} + \cdots \frac{\alpha_n^2}{N_n}} \times 100$$

where α_n is the experimental uncertainty in the quantity N_n. All the errors have been calculated in this manner and are illustrated in the appropriate tables.

CHAPTER 5

METHODS OF ANALYSING MULTIPLE SCATTERING

5.1 Methods of analysing multiple scattering

In gamma ray production cross-section measurements, as the sample thickness is increased, the probability of multiple scattering is also increased. The result is an effective increase in the measured cross-section, due to the extra gamma rays produced by further reactions for a constant neutron flux.

Analysis of how the effective cross-section varies with thickness of sample is often very difficult because of complicated geometry and variation of neutron cross-sections with energy and angle of scatter. Some of the more recent methods will be discussed below.

In the work by Day[9] using cylindrical geometry, a beam of neutrons incident along the z-axis is scattered by iron samples of various thicknesses. Analysis was made by considering the gamma ray yield from the first and second interactions, given by:

$$Y_1 = N_0 \left(1 - e^{-\mu d}\right) \frac{\sigma in}{\sigma_T}$$

$$Y_2 = K_2 \frac{\sigma in}{\sigma_T} \cdot \frac{N o d}{V} \cdot \iint e^{-\mu z} \, n \, \frac{d\sigma}{d\Omega}(\theta) \left(1 - e^{-\mu l}\right) dV d\Omega$$

where

N_0 = Number of incident neutrons

σ_T = Total neutron cross-section

σin = Total inelastic scattering cross-section

μ = Total neutron attenuation coefficient

n = Number of scatterer nuclei per unit volume

$\frac{d\sigma}{d\Omega}$ = Differential cross-section for gamma ray under consideration

d = scatterer thickness

l = neutron path length from first scatter point to surface of sample

K_2 = fraction of neutrons that produce an elastic event after the first scatter.

The integral was evaluated using a computer and the Gaussian integration formula. From the ratio of Y_2/Y_1 it was then possible to estimate the effect of even higher order scatters by using the assumption that the ratio of the probability of the ith + 1 collision to the probability of the ith collision is constant (P_{i+1}/P_i). The total gamma ray yield would then be given by:

$$Y = \sum_{i=1}^{n} Y_i = N_o \frac{\sigma in}{\sigma_T} \sum_{i=1}^{n} K_i P_i$$

$$= N_0 P_1 \frac{\sigma in}{\sigma_T} \sum_{i=1}^{n} K_i a^{i-1}$$

where: $a = P_{i+1}/P_i$ = constant

$N_0 K_i$ = Number of neutrons that can produce an event in the ion collision

The experimental results and theoretical variation in cross-section, for excitation of the 0.845MeV level in ^{56}Fe using 2.6MeV neutrons, with thickness of sample, are shown in Figure 5.1. However, the assumption made in using this method is that the total macroscopic cross-section does not change appreciably with energy of neutron. This assumption may be true for the case in question, however, it would not be true for very thick samples, since the energy degradation of the incident neutrons would be large and the total macroscopic cross-section varies overall as the inverse of

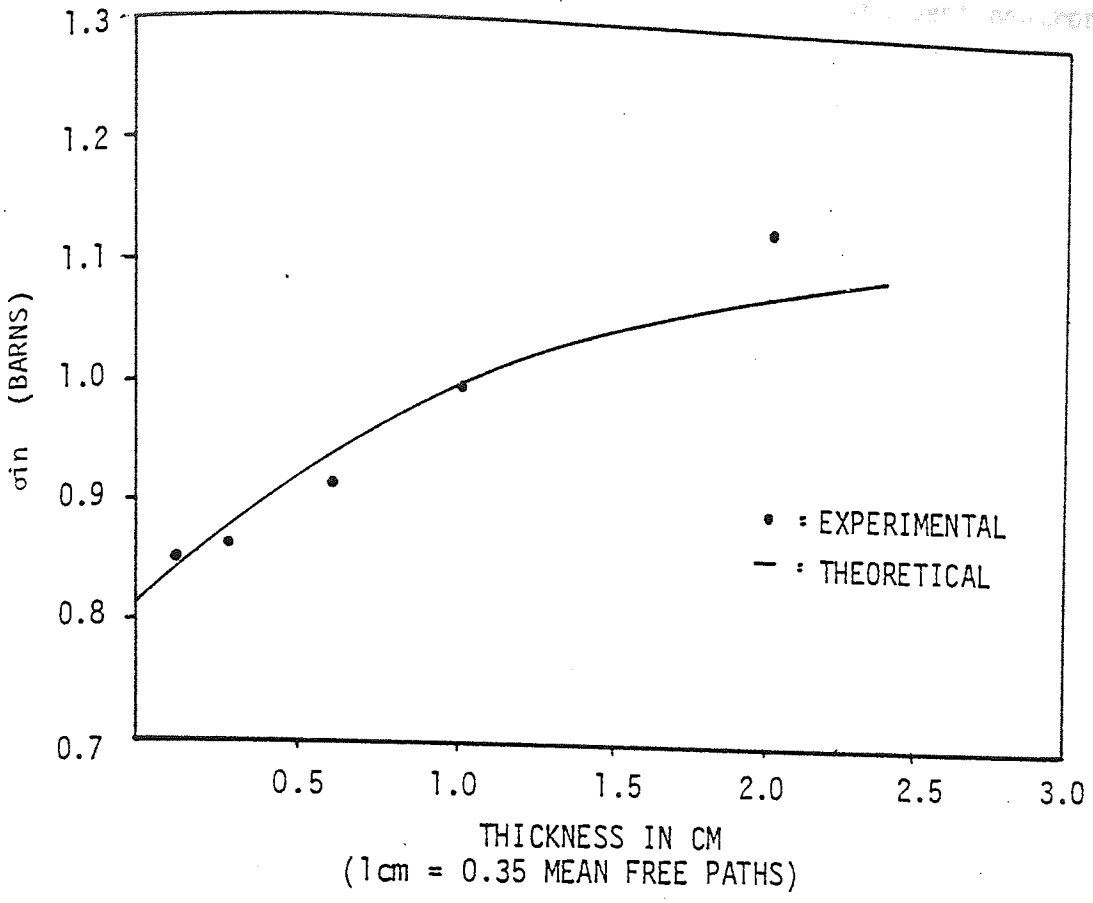

FIGURE 5.1 EFFECT OF MULTIPLE SCATTERING ON MEASURED CROSS-SECTION BY DAY (9) USING 2.6MeV NEUTRONS TO EXCITE THE 0.845MeV LEVEL IN IRON SAMPLES.

velocity. Furthermore, nuclear level density, incident neutron energy and atomic number would affect these assumptions.

Other analytical methods of measuring the effect of multiple scattering have been reported by Westard et al.[60], Al-shalabi[40] Cranberg et al.[61] and Anvarian[62]. In all cases simplifications had to be made in order to estimate the increase in yield and with the exception of Day[9], the approximations made would not give accurate quantitative results over a large range of mean free paths. Even the results of Day are shown over only 0.8mfps. Particularly interesting are the results of Al-shalabi[40] on iron and concrete using 14MeV neutrons. This work shows the effect of multiple scattering on angular distribution and uses Fermi-age theory as a basis of analysis. Although the theoretically predicted results do not give quantitatively accurate results, the shape of the angular distributions is predicted well.

5.2 Monte Carlo methods

Practical problems which employ the Monte Carlo method require the use of large computing facilities with the capability of random number generation and large virtual storage space. Although the principle of Monte Carlo may be used in many applications it is particularly suited to neutron transport problems. Usually, a number of source neutrons are considered to travel through a system and the individual neutron histories traced. Random numbers are used to determine the sequence of events in each neutron's life history in a manner which will be discussed.

Consider the problem of a beam of neutrons incident upon a sample of thickness h as shown below:

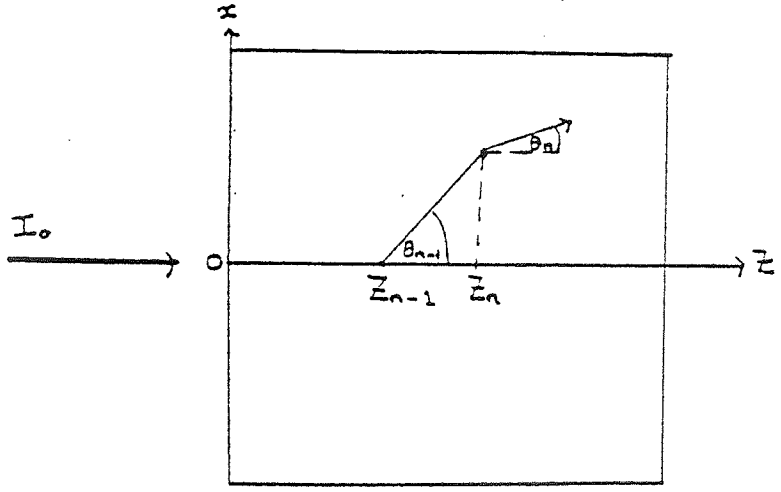

FIGURE 5.2: A simple Monte Carlo problem

It is assumed that there is a line source of monoenergetic neutrons E_o, of intensity I_o, so that the initial direction cosine is known and that no fission takes place, such that:

$$\Sigma_T = \Sigma_e + \Sigma_c + \Sigma_{in}$$

Σ_T = total macroscopic cross section

Σ_e = total macroscopic cross section for elastic scattering

Σ_{in} = total macroscopic cross section for inelastic scattering

Σ_c = total macroscopic cross section for capture

The problem of tracing the neutron histories may be divided into a number of discrete sections as given by Schriedner[63].

5.2.1 Path Length

In this section of a computer programme, a random number is generated to determine the first interaction point Z_o. This is achieved by using the path length distribution law:

Probability of interaction at Z_o = $\gamma = e^{-Z_o \Sigma_T(Eo)}$

where

γ = random number generated.

From the above, Z_o is found:

$$Z_o = \frac{-\log_e \gamma}{\Sigma_T(Eo)}$$

Hence, by generating random numbers path lengths throughout the sample may be found using the more general expression:

$$Z_n = Z_{n-1} - \mu_{n-1} \frac{\log_e \gamma}{\Sigma_T(Eo)}$$

$n = 1, 2, 3$ ....etc.

$\mu_{n-1} = \cos\theta_{n-1}$ defined in the diagram and will be defined later.

On calculation of a particular coordinate Z_n conditions are set up and tested in the programme:

(i) If $Z_n - h > 0$ Then the neutron has escaped plate

(ii) If $Z_n < 0$ neutron has been reflected

(iii) If $0 \leq Z_n \leq h$ the neutron has interacted at Z_n

IF either conditions (i) or (ii) are obeyed then the neutron history is terminated. If condition (iii) is obeyed then the history continues into the next section.

5.2.2 Reaction Type

Since the cross-sections are of the form

$$\Sigma_T = \Sigma_e + \Sigma_{in} + \Sigma_c$$

then the probabilities for elastic, inelastic and capture are defined by:

$$\frac{\Sigma_e}{\Sigma_T} \; ; \quad \frac{\Sigma_{in}}{\Sigma_T} \; ; \frac{\Sigma_c}{\Sigma_T}$$

These probabilities can be considered as lengths of a line between 0 and 1:

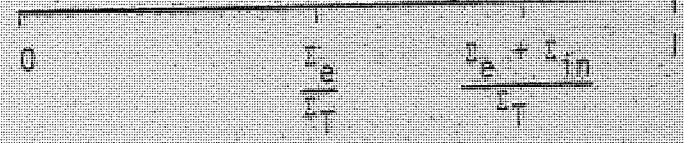

To find the particular reaction a collision point, another random number is generated and tested against the following conditions:

(i) If $\gamma \leq \frac{\Sigma_e}{\Sigma_T}$ ELASTIC SCATTERING OCCURS

(ii) If $\frac{\Sigma_e}{\Sigma_T} < \gamma \leq \frac{\Sigma_e + \Sigma_{in}}{\Sigma_T}$ INELASTIC SCATTERING OCCURS

(iii) If $\frac{\Sigma_e + \Sigma_{in}}{\Sigma_T} < \gamma \leq 1$ NEUTRON IS ABSORBED

If condition (iii) is observed then the neutron history is terminated. In the cases of conditions (i) and (ii) the problem proceeds to the next section of the programme. Consider elastic scattering:

5.2.3. Elastic Scattering

Elastic scattering is defined by the random variables $\hat{\theta}$ and χ in the centre of mass system. $\hat{\theta}$ is the scattering angle and χ is the azimuthal angle. They are defined:

$$0 \leq \hat{\theta} \leq \pi \qquad 0 \leq \chi \leq 2\pi$$

Using the laws of conservation of momentum we see that

$$\cos\psi = \frac{A\cos\hat{\theta} + 1}{\sqrt{A^2 + 2A\cos\hat{\theta} + 1}}$$

$$E_n = E_{n-1}\left(\frac{A^2 + 2A\cos\hat{\theta} + 1}{(A+1)^2}\right)$$

$$\mu_n = \mu_{n-1}\cos\psi + \cos\chi\sqrt{(1-\mu_{n-1}^2)(1-\cos^2\psi)}$$

ψ = scattering angle in lab frame, with respect to the incident neutron beam

A = Atomic mass of target nuclei

μ_n = Direction Cosines

If scattering is isotropic in the centre of mass frame

then $\hat{\theta}$ and χ are easily found by generating two more random numbers and using the equations:

$$\text{Cos } \hat{\theta} = 2\gamma_1 - 1 \qquad \chi = 2\pi\gamma_2$$

If scattering is not isotropic then, isotropy is assumed for χ and the fact that the probability density function is proportional to the differential elastic scattering cross-section as follows:

$$2\pi \int_{-1}^{\mu} \sigma_e(\hat{\theta}) d\mu = \gamma \sigma_c$$

$\sigma_e(\hat{\theta})$ = differential elastic scattering cross-section in C.O.M. frame for $\hat{\theta}$

From the latter expression cos $\hat{\theta}$ may be found and hence all the other variables.

5.2.4 Inelastic scattering

Inelastic scattering is more complicated and one method of dealing with the problem is to assume that the energy distribution of the scattered particles is Maxwellian. This is usually true for heavy nuclei and the probability density function is proportional to $E'e^{E'}/T$ where $T = a\sqrt{E}$.

E = Energy of particle before scattering

E' = Energy of inelastically scattered particles

a = Constant depending on the properties of the material

To obtain E' one may use the formula:

$$1 - e^{-E'/T}(1 + E'/T) = \gamma\left[1 - e^{-E/T}(1 + E/T)\right]$$

which may be written:

$$e^{-y}(1 + y) = \varepsilon \quad \ldots\ldots\ldots\ldots\ldots\ldots\ldots\ldots\ldots\ldots (5.1)$$

where

$$y = E'/T$$

$$\varepsilon = 1 - \gamma\left[1 - e^{-E/T}(1 + E/T)\right]$$

Equation (5.1) has a unique positive root when $0 < \varepsilon < 1$. This root may be computed using an iteration method which proceeds by initially choosing an arbitrary value for $y^{(0)} > 0$ then:

$$y^{(s+1)} = \log_e (1 + y^{(s)}) - \log \varepsilon$$

From this, y may be found and hence the energy of the scattered particle.

Assuming inelastic scattering is isotropic then by considering the unit vector in the direction of the neutron velocity before scattering:

$$\omega = \omega_1\hat{i} + \omega_2\hat{j} + \omega_3\hat{k}$$

$$\omega_1^2 + \omega_2^2 + \omega_3^2 = 1$$

In spherical coordinates:

$$\omega_1 = \sin\theta\cos\varphi \; ; \quad \omega_2 = \sin\theta\sin\varphi \; ; \quad \omega_3 = \cos\theta$$

If ω'_1, ω'_2, and ω'_3, θ' and φ' define the scattered neutron, then it can be shown that

$$\cos\theta' = \cos\theta\cos\psi + \sin\theta\sin\psi\cos\chi$$

$$\sin(\varphi' - \varphi) = \frac{\sin\psi\sin\chi}{\sin\theta'}$$

$$\cos(\varphi'-\varphi) = \frac{\cos\psi - \cos\theta\cos\theta'}{\sin\theta\sin\theta'}$$

Expressions for the new cartesian coordinates in terms of the old are:

$$\omega_3' = \omega_3\cos\psi + \sin\psi\cos\chi\sqrt{1-\omega_3^2}$$

$$\omega_2' = \frac{1}{(1-\omega_3^2)}\left[\omega_2(\cos\psi - \omega_3\omega_3') - \sin\psi\sin\chi\,\omega_1\sqrt{1-\omega_3^2}\right]$$

$$\omega_1' = \frac{1}{(1-\omega_3^2)}\left[\omega_1(\cos\psi - \omega_3\omega_3') - \sin\psi\sin\chi\,\omega_2\sqrt{1-\omega_3^2}\right]$$

where as before

χ = Azimuthal angle of scattering

ψ = Angle between ω and ω'

If scattering is isotropic then a random number may be generated to find:

$$\cos\theta' = 2\gamma - 1$$

Then by taking two random numbers the following condition may be employed:

If $(2\gamma_1 - 1)^2 + \gamma_2^2 \geq 1$

Then reject this pair and proceed with another pair until $(2\gamma_1 - 1)^2 + \gamma_2^2 < 1$ then

$$\cos\varphi' = \frac{(2\gamma_1 - 1)^2 - \gamma_2^2}{(2\gamma_1 - 1)^2 + \gamma_2^2} \qquad \sin\varphi = \frac{2(2\gamma_1 - 1)\gamma_2}{(2\gamma_1 - 1)^2 + \gamma_2^2}$$

Then finally:

$\omega_1' = \sqrt{1-\cos^2\theta'}\cos\varphi$; $\omega_2' = \sqrt{1-\cos^2\theta}\sin\varphi$ and $\omega_3' = \cos\theta'$

5.3 More General Methods

The latter methods employed to solve elastic and inelastic scattering serve as an example of how Monte Carlo problems are solved in this particular application. In general however, especially with inelastic scattering, theoretical formulae for energy distributions and angular distributions rely upon approximations. If it were the case that one had to rely upon these in the Monte Carlo method, then one might as well use analytical methods throughout. However, much cross-section data has been generated and it is possible to use the known probabilities for first scatter events to predict successive events.

If for example, it has been found in section 5.2.2 that a neutron has undergone inelastic scattering at a point in the sample. The angular distribution for such an event may be known and stored on magnetic tape as a series of legendre coefficients. If the distribution is divided up into a number of discrete angular regions, the probability for scattering into a certain region is proportional to the area under the angular distribution curve for this angular range. In fact by normalising the angular distribution, the actual probabilities may be determined. The angle into which an inelastic neutron is scattered is then found by the same principle as in the "reaction type" section. That is to say, since the sum of the probabilities is equal to unity, then they may be managed on a line between 0 and 1. A random number is then generated to see which region it falls into and hence the associated angle is known.

In a similar manner, the variation in cross-section with energy may be divided into energy groups and the probability for

scattering down into lower groups may be found. There will also be a probability of upscattered neutrons into a higher energy group if fission occurs as shown by Dickinson et al.[64]. However, this is not of concern in the present application.

The above illustrates how the energy and angle of a scattered neutron is determined in more modern computing codes using the Monte Carlo Method. Although in principle, any reaction may be catered for, using this technique requires a large library of stored cross-section data for each reaction type, at different neutron energies. The M.O.R.S.E. code chosen for present work uses this principle and will be discussed in more detail in section 5.6.

5.4 Terminating Neutron Histories and the Method of Statistical Weights

The history of a neutron may be ended by either escaping from the sample, being captured, reaching a pre-determined energy cut off or by a method known as Russian Roullete. The latter method necessitates the use of statistical weights.

In general, when the trajectory of a particle is modelled, it is necessary to introduce random variables $\varepsilon_1, \varepsilon_2, \varepsilon_3 \ldots\ldots\ldots \varepsilon_N$ with associated probability density functions $P_1(x)$, $P_2(x)$, $P_3(x)$ $\ldots\ldots P_N(x)$ respectively. The trajectories are then found from the mean value of a third function $f(\varepsilon_1\ \varepsilon_2\ \varepsilon_3 \ldots\ldots \varepsilon_N)$. Suppose at each state instead of using the random variable ε_k, we use η_k with another probability density function $\hat{P}_k(\eta)$. Then another trajectory could be found and the averaged function would be given by:

$$f(\eta_1, \eta_2, \eta_3 \ldots\ldots \eta_N)\ \frac{P_1(\eta_1)P_2(\eta_2)\ldots\ldots P_N(\eta_N)}{\hat{P}_1(\eta_1)\hat{P}_2(\eta_2)\ldots\ldots\hat{P}_N(\eta_N)}$$

From which we see that the statistical weight of a particle is altered according to the rule:

$$\omega_k = \omega_{k-1}\ \frac{P_k(\eta_k)}{\hat{P}_k(\eta_k)} \qquad \text{where } \omega_0 = 1, \quad k = 1 \text{ to } N$$

In the most general Monte Carlo programmes the weighting procedure is useful when the weight of a particle falls below a certain predetermined value and Russian Roullete is involved. In this a random number is generated and if a particle has a lower weight than this number, its history is termined. If not, the particle is given a larger weight and allowed to carry on its journey.

To give a clearer understanding of weights consider its application to more modern computing codes. Each neutron incident on a given sample is assigned a weight usually unity. Then, as the particle makes its track through the sample, at each collision it is multiplied by the non-absorption probability. For example, if the non-absorption probability is 0.6 and if one takes a 1000 neutrons then on average after the first collision 400 will be absorbed. However, using weights there will still be 1000 neutrons each with a weight of 0.6 after the first collision.

After each collision the weight is tested using a random number and if the weight of a particle is less than a value ω_n, then Russian Roullete is played and the neutron is assigned a new value $\omega_A > \omega_n$ or is 'killed'. If the weight of a neutron becomes too high then it is split into two neutrons each of lower weight ω_H. At any instant the neutron will be left to track if its weight lies in the region $\omega_n < \omega_A < \omega_H$.

Russian Roullete does not in any way bias the calculations since, a neutron whose weight falls below a certain value $\omega < \omega_n$ has a survival probability ω/ω_A. If a random number γ is generated such that $\gamma < \omega/\omega_A$ the neutron continues its history with weight ω_A. Otherwise if $\gamma < \omega/\omega_A$ the neutron is killed with a weight of zero. Hence, from the theory of probability that the probability of an event A or B happening is given by A P(A) + A P (B) = Probability of event), then the expected weight after a collision involving Russian Roullete would be:

$$\left(\frac{\omega}{\omega_A}\right) \omega + \left(1 - \frac{\omega}{\omega_A}\right) . 0 = \omega$$

In the M.O.R.S.E. code,[10] because of the large number of applications and general versatility of the programme, statistical weights are used to increase its efficiency. It also leads to more accurate predictions in parameters such as the neutron multiplicity factor in fission reactor core calculations.

5.5 Computing techniques in neutron transport problems

Tracing the history of a neutron and its associated scattered particles through a sample involves the computation of a "family tree" for the neutron which may become very complex if fission occurs and the region size is large. Two methods of storage and computation of trees are available at present.

The first is called, processing by generations. This is suitable for long branches which are not very 'branching'. This means that from the particles of one generation, all the particles of the next generation are calculated and stored for calculation of the next generation. As a result only two generations need be stored at any one time.

The second kind of processing is called lexicographic processing of trees. This is suitable for short but highly branching trees. In this method, calculation is carried out along a particular branch until the end is reached. The computation then moves back one step and the last branch is eliminated from the memory by being output. The two methods are illustrated in Figure 5.3.

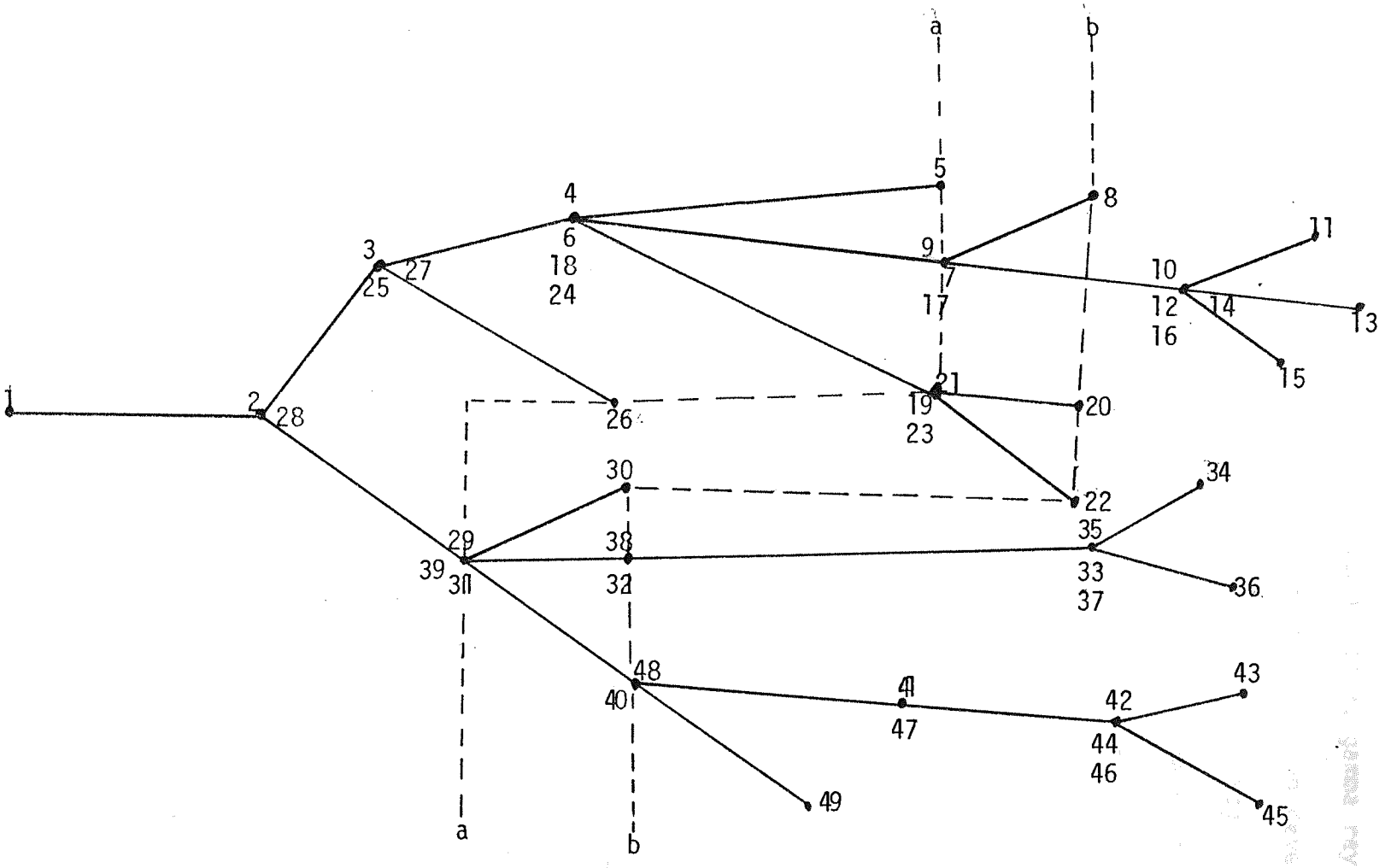

FIGURE 5.3 Numbers indicate lexicographic technique

Dotted lines indicate a possible computation by generations

5.6 The M.O.R.S.E. Code

The M.O.R.S.E. Code (Multigroup Oak Ridge Stochastic Experiment) is a programme which is used to solve the neutron transport problem in three modes for neutrons only, gamma rays only and neutron-gamma ray scattering. The programme has been developed over a period of about twenty years, mainly at Oak Ridge Laboratory, although in recent years changes have been made at Harwell (U.K.A.E.). Because of this the programme has become very large and versatile and only a summary of the main subroutines and overall programme can be given here. For full details the M.O.R.S.E. manual[10a] should be consulted. The programme can be divided into six main sections.

5.6.1 User

The main subroutine in this section is called SCORIN and this deals with general information about the user. Accounting and bookkeeping can be dealt with here.

5.6.2 Source

This section contains specific information about the neutron source to be used in a simulated experiment. It has the capability of providing any combination of monoenergetic, mixed energy, isotropic, or anisotropic neutron sources. If the source were chosen to be of mixed neutron energy, then the input requires the user to define the desired energy groups as taken from the cross-section library. Provision is also made for biasing each source neutron energy group using weights, so that a distribution or

effective beam profile may be obtained. The source is defined and normalised to a standard 1 neutron/second batch. Input into theprogramme would be the number of neutrons per batch and the number of batches to be run. Typically one would take 1000 neutrons per batch and 30 batches. A restart option is then available if by this time the statistics are not good enough.

For present work, a monoenergetic 14MeV (average for group) point source was chosen to be about 20cm from the sample, with all neutrons incident along the z-axis, normal to the face of the sample.

5.6.3 Cross-Section

This section reads in the main subroutines XSEC, JINPUT and READSG. The function of these is:

XSEC - Sets aside parameters necessary for storage

JINPUT - Mixing parameters for data. This requires a knowledge of the densities of various elements that might be present in a compound sample

READSG - Reads the actual cross-sections.

The group cross-sections are stored on a library tape DLC 37F ANISN cross-sections in this case, formulated from the ENDF/B-IV data. To access the cross-sections for a particular medium, element identifiers are called for which are defined as a number on the ANISN tape. Furthermore, the P-order of the Legendre polynomials for each element is asked for as input. Altogether there are 100 neutron groups and 21 gamma ray energy groups and these

are defined in Tables 5.1 and 5.2. The cross-sections are stored in a 124 X 121 matrix in the form shown in Figure 5.4. For the present work, within the group the gamma ray scattering corresponded to the compton scattering probabilities and were set to zero, since the Compton flux contribution was not required for the ultimate flux evaluation.

The Legendre polynomials are converted into angles and probabilities of scattering at those angles by using the angular distribution as a weight function:

$$\int_{-1}^{+1} f(\mu)\,\omega(\mu)\,d\mu = \Sigma f(\mu_i)\omega_i$$

where:

$f(\mu)$ is any polynomial of order 2N-1 or less.

$\omega(\mu)$ is the angular distribution for scattering cosine μ

μ_i is a set of discrete cosines

ω_i is the probability of scattering at these cosines

To find μ_i and ω_i that satisfy the above equations it is necessary to define a set of orthogonal polynomials:

$$\int_{-1}^{+1} Q_i Q_j\,\omega(\mu)\,d = N_i \delta_{ij}$$

N_i is the normalisation coefficient. The moments of the angular distribution determine the orthogonal polynomials.

The probabilities are obtained by:

$$\omega_i = \sum_{K=1}^{k=n-1} \frac{Q_k^2(\mu_i)}{N_i}$$

TABLE 5.1

100-Group Neutron Structure

Group	Energy Range (eV)		Group	Energy Range (eV)	
1	1.4918E 07*	1.3499E 07	51	8.6517E 04	6.7380E 04
2	1.3499E 07	1.2214E 07	52	6.7380E 04	5.2475E 04
3	1.2214E 07	1.1052E 07	53	5.2475E 04	4.0868E 04
4	1.1052E 07	1.0000E 07	54	4.0868E 04	3.1828E 04
5	1.0000E 07	9.0484E 06	55	3.1828E 04	2.4788E 04
6	9.0484E 06	8.1873E 06	56	2.4788E 04	1.9305E 04
7	8.1873E 06	7.4082E 06	57	1.9305E 04	1.5034E 04
8	7.4082E 06	6.7032E 06	58	1.5034E 04	1.1709E 04
9	6.7032E 06	6.0653E 06	59	1.1709E 04	9.1188E 03
10	6.0653E 06	5.4881E 06	60	9.1188E 03	7.1018E 03
11	5.4881E 06	4.9659E 06	61	7.1018E 03	5.5309E 03
12	4.9659E 06	4.4933E 06	62	5.5309E 03	4.3074E 03
13	4.4933E 06	4.0657E 06	63	4.3074E 03	3.3546E 03
14	4.0657E 06	3.6788E 06	64	3.3546E 03	2.6126E 03
15	3.6788E 06	3.3287E 06	65	2.6126E 03	2.0347E 03
16	3.3287E 06	3.0119E 06	66	2.0347E 03	1.5846E 03
17	3.0119E 06	2.7253E 06	67	1.5846E 03	1.2341E 03
18	2.7253E 06	2.4660E 06	68	1.2341E 03	9.6112E 02
19	2.4660E 06	2.2313E 06	69	9.6112E 02	7.4852E 02
20	2.2313E 06	2.0190E 06	70	7.4852E 02	5.8295E 02
21	2.0190E 06	1.8268E 06	71	5.8295E 02	4.5400E 02
22	1.8268E 06	1.6530E 06	72	4.5400E 02	3.5358E 02
23	1.6530E 06	1.4957E 06	73	3.5358E 02	2.7537E 02
24	1.4957E 06	1.3534E 06	74	2.7537E 02	2.1445E 02
25	1.3534E 06	1.2246E 06	75	2.1445E 02	1.6702E 02
26	1.2246E 06	1.1080E 06	76	1.6702E 02	1.3007E 02
27	1.1080E 06	1.0026E 06	77	1.3007E 02	1.0130E 02
28	1.0026E 06	9.0718E 05	78	1.0130E 02	7.8893E 01
29	9.0718E 05	8.2085E 05	79	7.8893E 01	6.1442E 01
30	8.2085E 05	7.4274E 05	80	6.1442E 01	4.7851E 01
31	7.4274E 05	6.7206E 05	81	4.7851E 01	3.7267E 01
32	6.7206E 05	6.0810E 05	82	3.7267E 01	2.9023E 01
33	6.0810E 05	5.5023E 05	83	2.9023E 01	2.2603E 01
34	5.5023E 05	4.9787E 05	84	2.2603E 01	1.7604E 01
35	4.9787E 05	4.5049E 05	85	1.7604E 01	1.3710E 01
36	4.5049E 05	4.0762E 05	86	1.3710E 01	1.0677E 01
37	4.0762E 05	3.6883E 05	87	1.0677E 01	8.3153E 00
38	3.6833E 05	3.3373E 05	88	8.3153E 00	6.4760E 00
39	3.3373E 05	3.0197E 05	89	6.4760E 00	5.0435E 00
40	3.0197E 05	2.7324E 05	90	5.0435E 00	3.9279E 00
41	2.7324E 05	2.4724E 05	91	3.9279E 00	3.0590E 00
42	2.4724E 05	2.2371E 05	92	3.0590E 00	2.3824E 00
43	2.2371E 05	2.0242E 05	93	2.3824E 00	1.8554E 00
44	2.0242E 05	1.8316E 05	94	1.8554E 00	1.4450E 00
45	1.8316E 05	1.6573E 05	95	1.4450E 00	1.1254E 00
46	1.6473E 05	1.4996E 05	96	1.1254E 00	8.7644E-01
47	1.4996E 05	1.3569E 05	97	8.7644E-01	6.8257E-01
48	1.3569E 05	1.2277E 05	98	6.8257E-01	5.3159E-01
49	1.2277E 05	1.1109E 05	99	5.3159E-01	4.1400E-01
50	1.1109E 05	8.6517E 04	100	4.1400E-01	1.0000E-04

*Read 1.4918×10^7.

TABLE 5.2

21-Group Gamma-Ray Structure

Gamma-Ray Group	Coupled Group	Group Boundaries (MeV)
1	101	1.2E01-1.4E01*
2	102	1.0E01-1.2E01
3	103	8.0E00-1.0E01
4	104	7.5E00-8.0E00
5	105	7.0E00-7.5E00
6	106	6.5E00-7.0E00
7	107	6.0E00-6.5E00
8	108	5.5E00-6.0E00
9	109	5.0E00-5.5E00
10	110	4.5E00-5.0E00
11	111	4.0E00-4.5E00
12	112	3.5E00-4.0E00
13	113	3.0E00-3.5E00
14	114	2.5E00-3.0E00
15	115	2.0E00-2.5E00
16	116	1.5E00-2.0E00
17	117	1.0E00-1.5E00
18	118	4.0E-01-1.0E00
19	119	2.0E-01-4.0E-01
20	120	1.0E-01-2.0E-01
21	121	1.0E-02-1.0E-01

*Read 1.4×10^{1}.

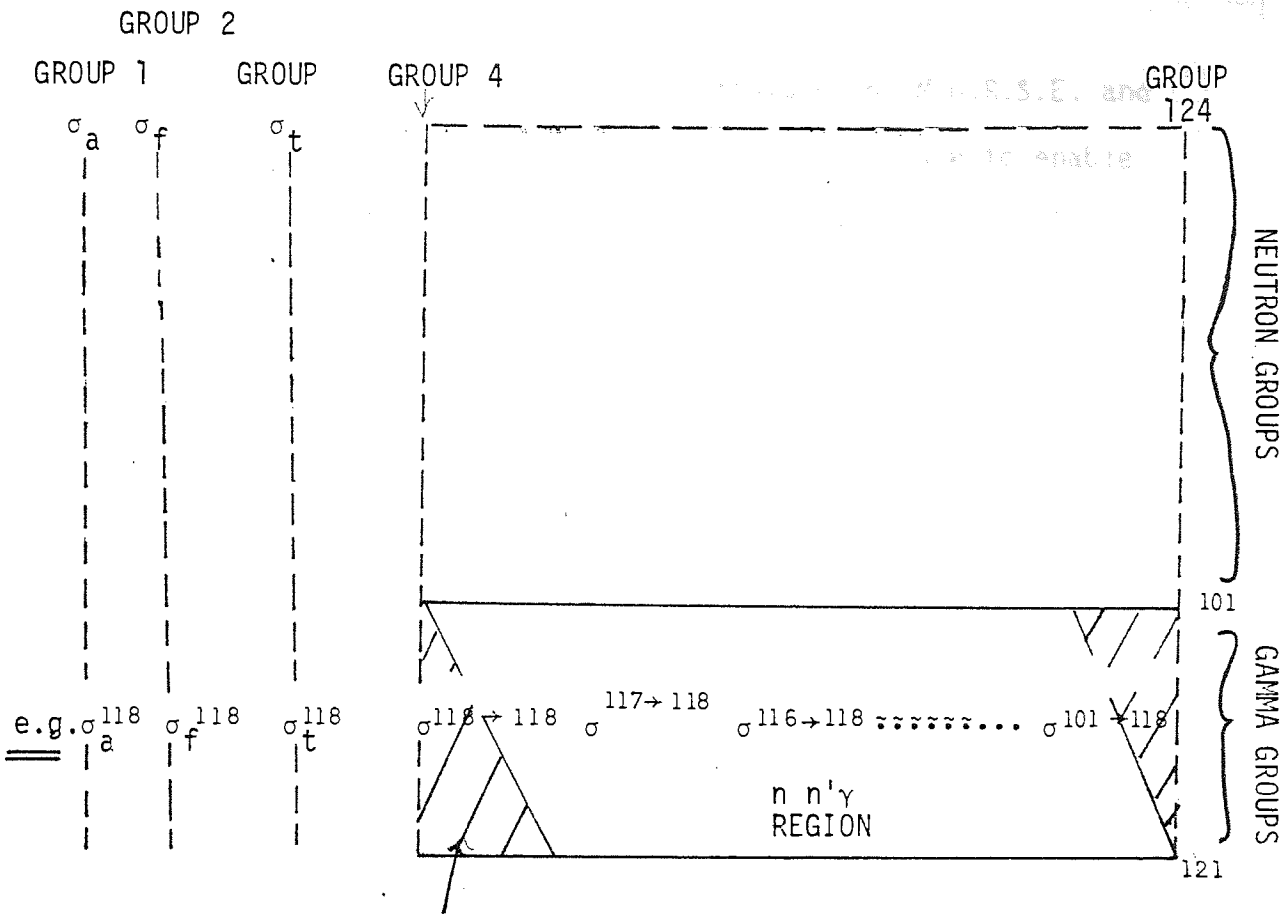

σ_a = TOTAL ABSORPTION CROSS-SECTION

σ_f = TOTAL FISSION CROSS-SECTION

σ_t = TOTAL CROSS-SECTION

$\sigma^{118\to 117}$ = Probability of a neutron in group 118 being scattered into group 117

FIGURE 5.4 STRUCTURE OF MATRIX IN WHICH CROSS-SECTIONS ARE STORED ON THE DLC-37F LIBRARY TAPE

5.6.4 Geometry

This section is one of the main features of M.O.R.S.E. and is read in by the subroutine JOMIN. Provision is made to enable very complicated three dimensional problems to be set up. The manner in which this is achieved will be discussed below.

The combinational geometry module employs standard simple shapes, such as rectangular block cylinder or sphere, and by combining these, using the principles of Boolean algebra, complicated shapes are formed. The possible standard shapes are termed zones and may be listed:

1. Rectangular parallelepiped
2. Rectangular block
3. Sphere
4. Right circular cylinder
5. Right elliptical cylinder
6. Truncated Right angle cone
7. Ellipsoid
8. Right angle wedge
9. Arbitrary polyhedron (4, 5 or 6 sides)

There are two other possible zone features, in that once a region is formed it may be labelled as either an internal void, in which a neutron may be tracked with no interaction taking place, or an external void in which a neutron's history is immediately terminated. A two-dimensional example of how different shapes may be combined will be illustrated overleaf using the following operators:

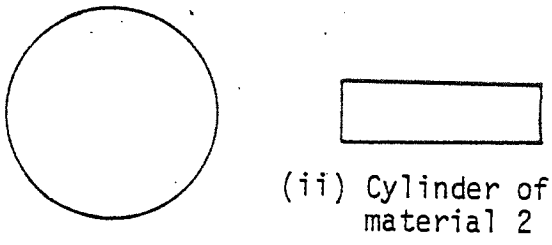

(i) Sphere of material 1

(ii) Cylinder of material 2

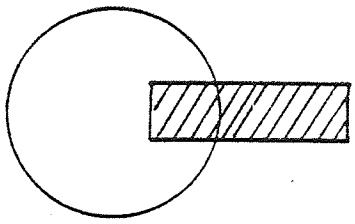

+ 2 - 3 Gives (iii) Sphere with hole in which material 2 fits

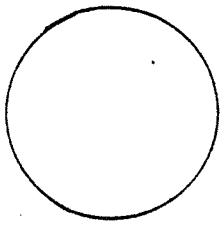

(i) Sphere of material 1

(ii) Cylinder of material labelled 2 but same as 1

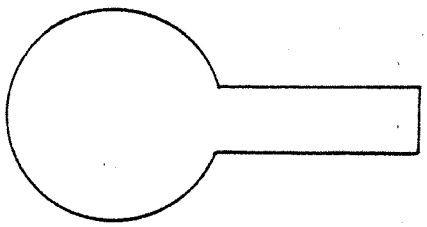

or + 1 or +2 gives (iii) above shape all of same material

FIGURE 5.5 BOOLEAN ALGEBRA METHOD OF COMBINING STANDARD SHAPES

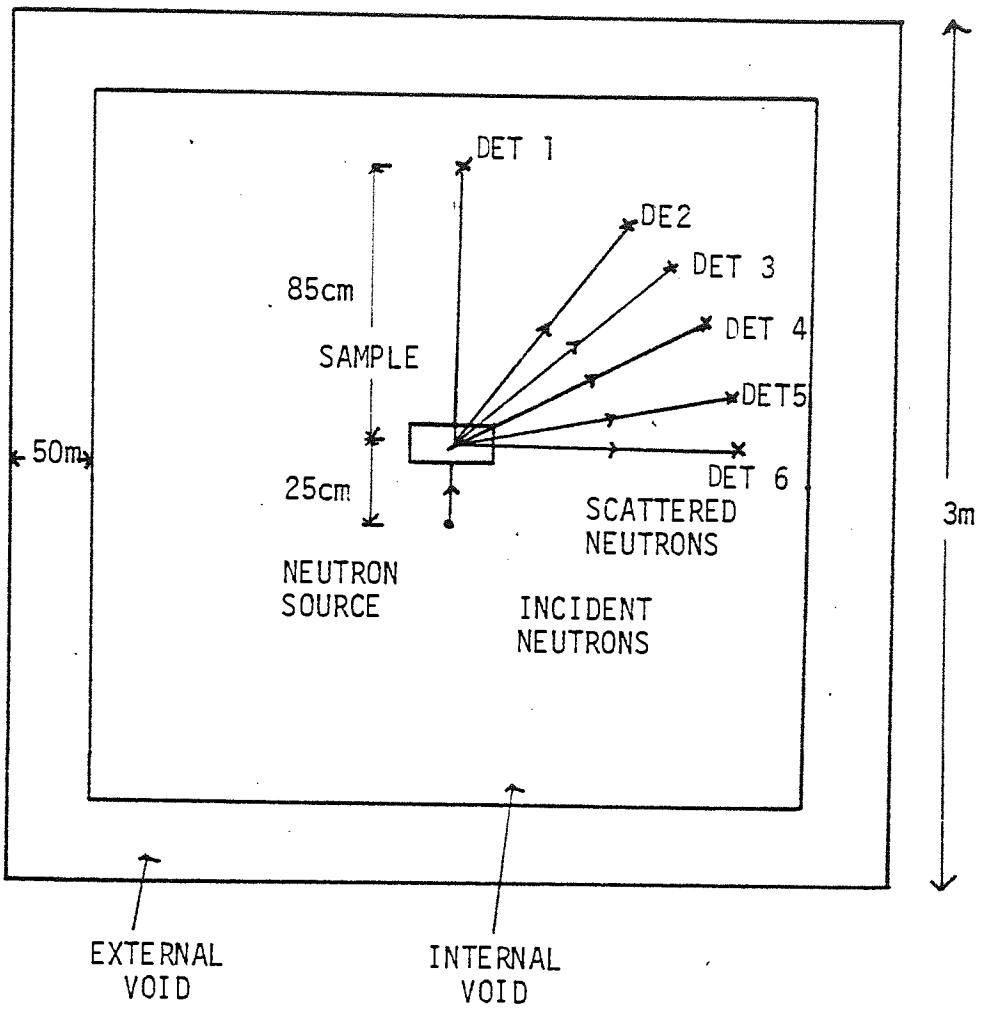

FIGURE 5.6 COMBINATIONAL GEOMETRY SIMULATION OF LABORATORY EXPERIMENT

1 + = The zone described is wholly contained in the body

2 - = The zone described is wholly outside the body

3 OR = The zone described contains all points in the body

The diagram (Figure 5.5) shows how a sphere and cylinder may be combined using the above operators.

In the present application, the whole laboratory simulation was enclosed in a box of 3 x 3 x 3m. The samples were placed at the centre of the box with a neutron source 25cm from the sample face. Scattered neutrons and gamma rays were collected in a number of detectors placed at 85cm from the centre of the sample, arranged at different positions aruund the sample. A plan view of the simulation is shown in Figure 5.6.

5.6.5 Walk

This section contains the subroutines INPUT 1 and INPUT 2 which contain all the information necessary to perform the random walk. In essence, the module generates a source batch of particles and stores them in a bank. It then selects one particle and traces its history. Any secondary particles generated are also stored in a bank ready for processing. On completion of a batch a summary of events are output via the input/output section of the programme. A complete summary of all histories is given by the analysis module which is discussed in the next section. A flow diagram illustrating the basic random walk computing procedure is shown in Figure 5.7.

FIGURE 5.7 RANDOM WALK GENERATING PACKAGE

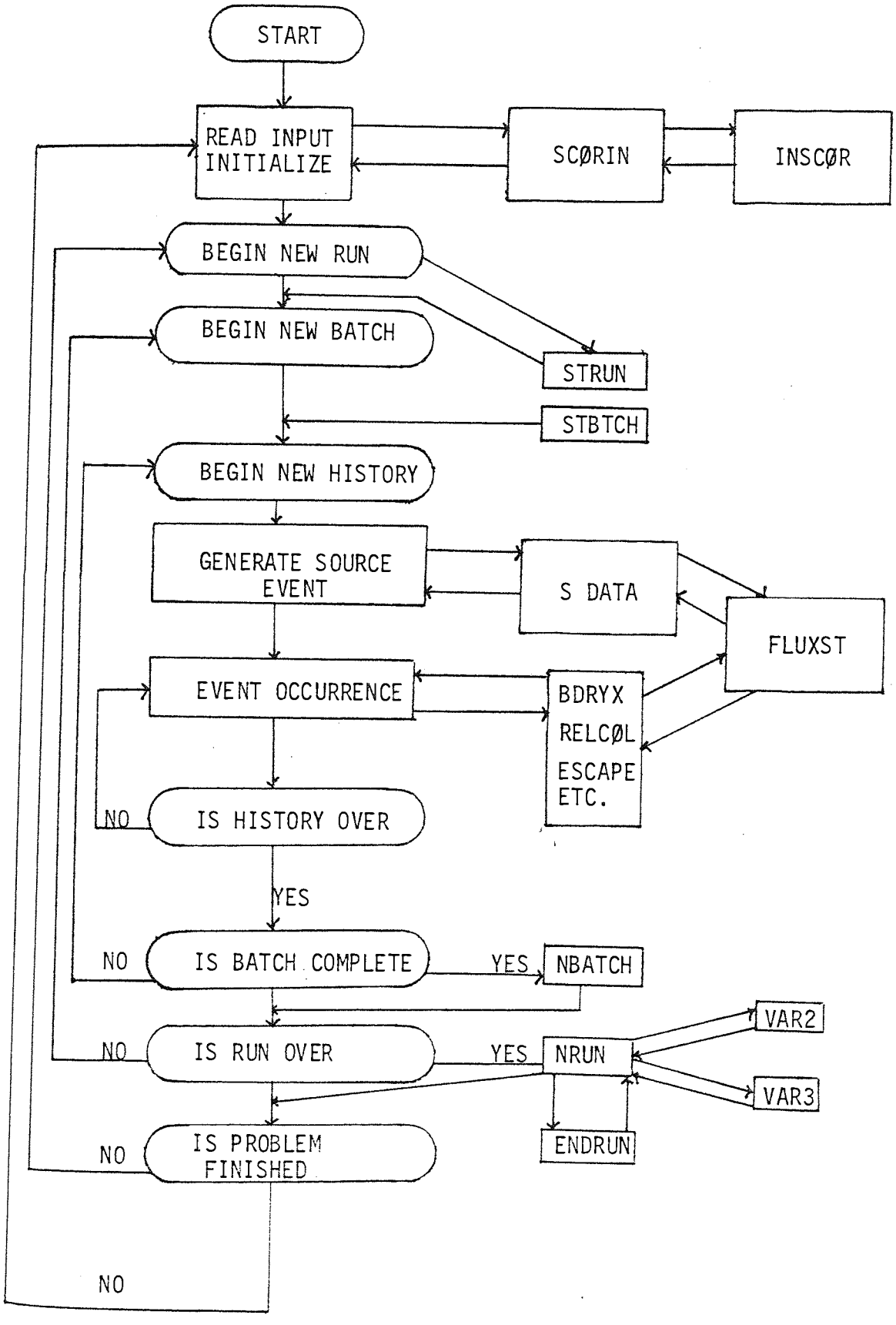

5.6.6 Analysis

The module in M.O.R.S.E. concerned with analysis is a special package called S.A.M.B.O. (Stochastic Analysis Machine BOok-keeping). It allows for an arbitrary number of detectors, energy dependent response functions, energy bins, time bins and angle bins. Output from this section may be subdivided:

1. Uncollided and total response - the uncollided response gives the total response of the detector to neutrons that pass through a sample without interacting. The total response gives the total particle flux incident on a detector.

2. Fluence versus energy and detector. This gives the flux of either neutrons or gammas being analysed for specific energy groups.

3. Time dependent response - This gives the change in flux with time and was not used in present application.

4. Fluence versus time, energy and detector number - again this was not used.

5. Fluence versus angle, energy and detector - the flux of neutrons and gamma rays for the specific energy groups under analysis is given in pre-determined angle bins.

The package contains both point and track length detectors. The latter allows a detection volume to be set up, the former being a point detector with facial area $1cm^2$. Point detection was chosen for the present application so that detectors could be arranged as almost theoretical points at set distances around the sample analogous to the practical arrangement. It is worth noting that

since the detectors are so small, the flux at each point would also be correspondingly small, if it were not for the following fact. If a neutron is not scattered in the direction of the detector, the programme evaluates the probability that it would have been scattered in that direction. The flux is then found from:

$$\phi(r) = \int dV' \int dr' \int dV \int d\Omega E(r', V\Omega) \left[P\left(\frac{\underline{r} - \underline{r}'}{|\underline{r} - \underline{r}'|} \cdot \underline{\Omega V} \right) \frac{e^{-\Sigma(v')(|r-r'|)}}{|r-r'|^2} \right]$$

where

$E(r', V, \underline{\Omega}) dr' dV' d\Omega$ = density of particles of speed dV in direction $d\Omega$ entering volume dr'

$P(\mu v)$ = Probability of a particle scattering with speed v into cosine μ. V' is the outgoing velocity and $\Sigma(v')$ is the total macroscopic cross-section for speed v'.

This mathematical trick speeds up accumulation time and makes the overall programme more efficient.

The actual output from the analysis section begins by giving the history of each batch of neutrons. To illustrate this consider a typical output from M.O.R.S.E. with explanatory notes:

WTAVE = 1000 - the number of neutrons in batch 1

IAVE = 1 - number of neutron sources

UVAVE,; VAVE; WAVE; Are 0, 0, 1 respectively and denote the direction cosines of the neutron source

SAVE,; YAVE; ZAVE - Are 1.5×10^2, 1.5×10^2, 1.2×10^2 respectively denoting the coordinates of the neutron source relative to an initial frame

AGEAVE = 0 Gives the starting age of the neutrons

SOURCE = 1000 - Number of neutrons incident on sample

SPLIT(D) = 0 - Number of neutrons split into two or more particles

FISHN = 0 - Number of incident particles creating fission neutrons

GAMGEN = 455 - Number of gamma rays generated by 1000 neutrons

REALCOLL = 1392 - Total number of neutron collisions including multiple scattering

ALBEDO = 0 - Number of reflected neutrons - Abedo option was not used in present work

BORYX = 2231 - Number of border crossings

ESCAPE = 1231 - Number of particles that escape the sample

E-CUT = 206 - Number of neutrons reaching energy cut off

TIME KILL = 0 - Number of neutrons killed by present time

RR-KILL = 0 - Number of neutron histories terminated by Russian Roullete

RR-SURV = 0 - Number of neutrons surviving Russian Roullete

GAMLOST = 0 - Number of gamma rays lost

After the latter is output batch 2 begins its output and so forth until all batches are complete or a time cut off is reached.

The next section in the output gives the total responses of the detectors for both the uncollided response and total response for gamma rays and neutrons. The flux in this section is given by:

$$\text{FLUX} = \int \emptyset\ (\underline{r}, \underline{E})\ dE \text{ units } cm^{-2}\, sec^{-1}$$

where:

$\emptyset\ (\underline{r}, E)$ = FLUENCE in units $cm^{-2}\, sec^{-1}\, eV^{-1}$ for a 1n/sec source.

From the latter is calculated the flux for each detector and corresponding energy group under analysis and this is output after the total responses.

The final section gives the flux in terms of $\emptyset\ (\underline{r},E,\underline{\Omega})$. The units are $cm^2\ sec^{-1}\ eV^{-1}$ steradian^{-1} and the relation between this and the latter is:

$$\emptyset(\underline{r},E) = \emptyset(\underline{r},E,\underline{\Omega})\ d\underline{\Omega}$$

Neutron or gamma ray cross-sections were calculated using M.O.R.S.E. fluxes and the corresponding formula:

$$\frac{d\sigma}{d\Omega} = \frac{\emptyset\ (\underline{r},E)\ \Delta E\ \sigma_T}{\Delta\Omega(1-\exp(-\Sigma(Eo)x))}$$

σ_T = Total cross-section

$\Delta\Omega$ = Elemental solid angle (NB detector area - $1cm^2$)

$\Sigma(Eo)$ = Macroscopic cross-section for neutrons of incident energy Eo

5.6.7 Errors

Beneath all flux estimates is given the fractional standard deviation as a measure of the validity of the statistics. In M.O.R.S.E. these estimations are made using:

$$\sigma_{\bar{x}}^2 = \frac{1}{N-1}\left[\frac{1}{n}\sum_{i=1}^{N} n_i x_i^2 - \frac{1}{n^2}\left(\sum n_i x_i\right)^2\right]$$

n = Number of independent histories (total)

n_i = Number of independent histories of the i^{th} batch

where:

$$n = \sum_{i=1}^{N} n_i$$

$$x_i = \frac{1}{n_i} \sum_{j=1}^{n_i} x_{ij} \quad \text{mean batch estimate}$$

$$\bar{x} = \frac{1}{n} \sum_{i=1}^{n} n_i x_i \quad \text{overall mean estimate}$$

The fractional standard deviation is then given by:

$$\text{f.S.D.} \qquad \frac{\sqrt{\sigma_{\bar{x}}^2}}{\bar{x}}$$

TABLE 5.3:

TABULATED M.O.R.S.E. RESULTS FOR GAMMA RAY PRODUCTION CROSS-SECTION OF ^{7}Li

THICKNESS		DIFFERENTIAL CROSS-SECTION FOR 0.478MeV LEVEL IN ^{7}Li (mb/st)
CM	MEAN FREE PATHS	
1	0.1	6.5 ± 0.3
4	0.42	9.9 ± 0.5
9	0.84	13.5 ± 0.7
13	1.36	17.0 ± 0.8
17	1.8	18.8 ± 0.9
22	2.2	19.2 ± 1.0

FITTING PARAMETERS FOR ABOVE POINTS:

σ_o = 4.55 mb/st

σ_M = 21.1 mb/st

ERRORS ARE ONLY STATISTICAL

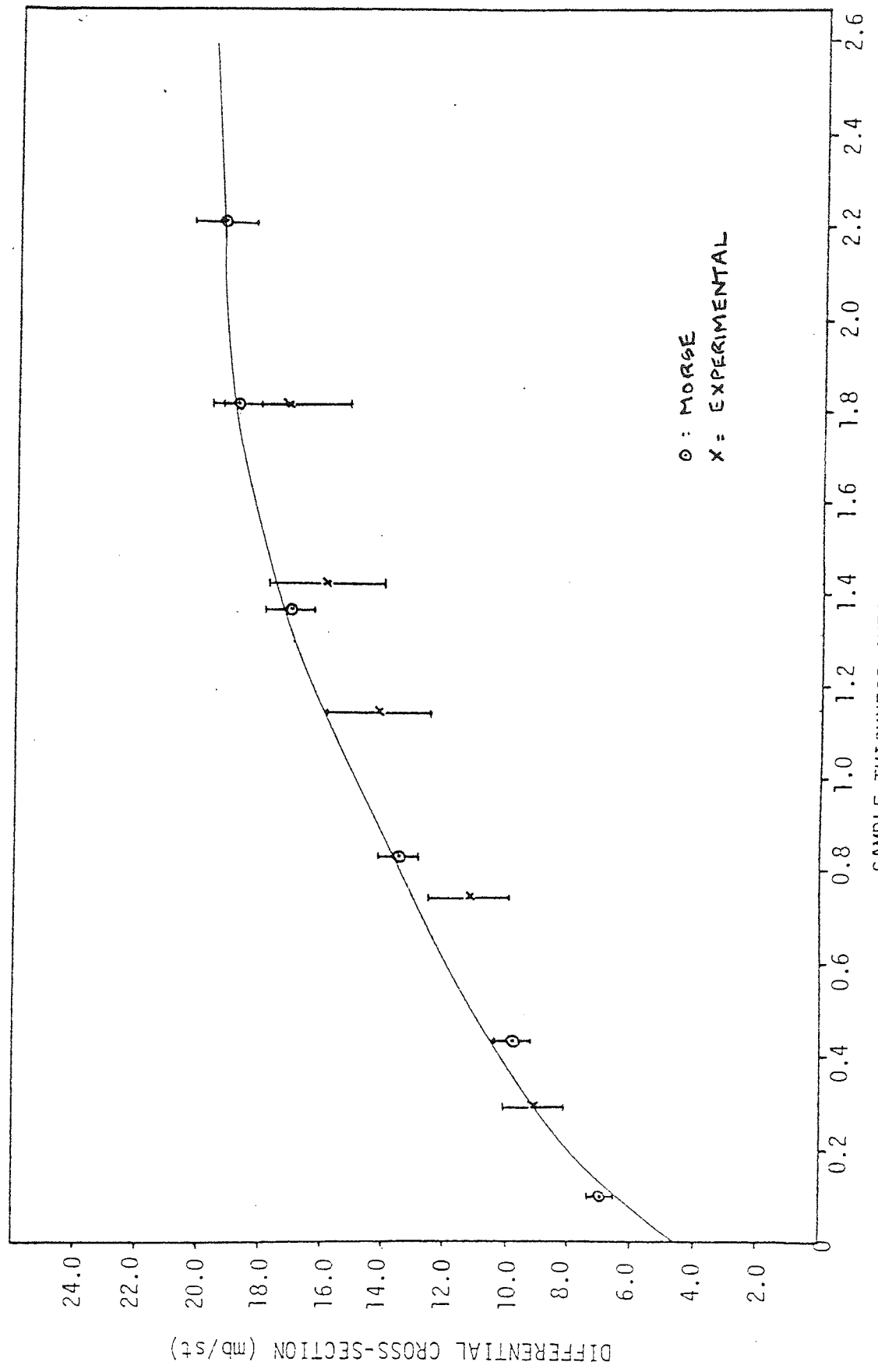

FIGURE 5.8 COMPARISON OF EXPERIMENTAL AND M.O.R.S.E RESULTS FOR GAMMA RAY PRODUCTION DIFFERENTIAL CROSS-SECTIONS IN ^{7}Li (0.478MeV LEVEL)

TABLE 5.4 M.O.R.S.E. RESULTS FOR LEAD

THICKNESS		DIFFERENTIAL CROSS-SECTION AT 90° (mb/st)				
(cm)	(m.f.p.)	ENERGY→0.4-1MeV	1-2MeV	2-3MeV	3-4MeV	4-5MeV
0.9	0.16	233	128	73	42	30.5
2.0	0.36	257	139	81	44	31.0
3.0	0.54	277	146	89	48	30.3
5.0	0.89	320	166	96	51	36.6
7.0	1.25	351	183	103	57	40.0
9.0	1.59	379	192	113	60	38.0
12.0	2.14	414	212	124	63.5	46.0
15.0	2.68	442	220	133	68.0	48.0
25.0	4.46	498	243	146	72.0	53.0

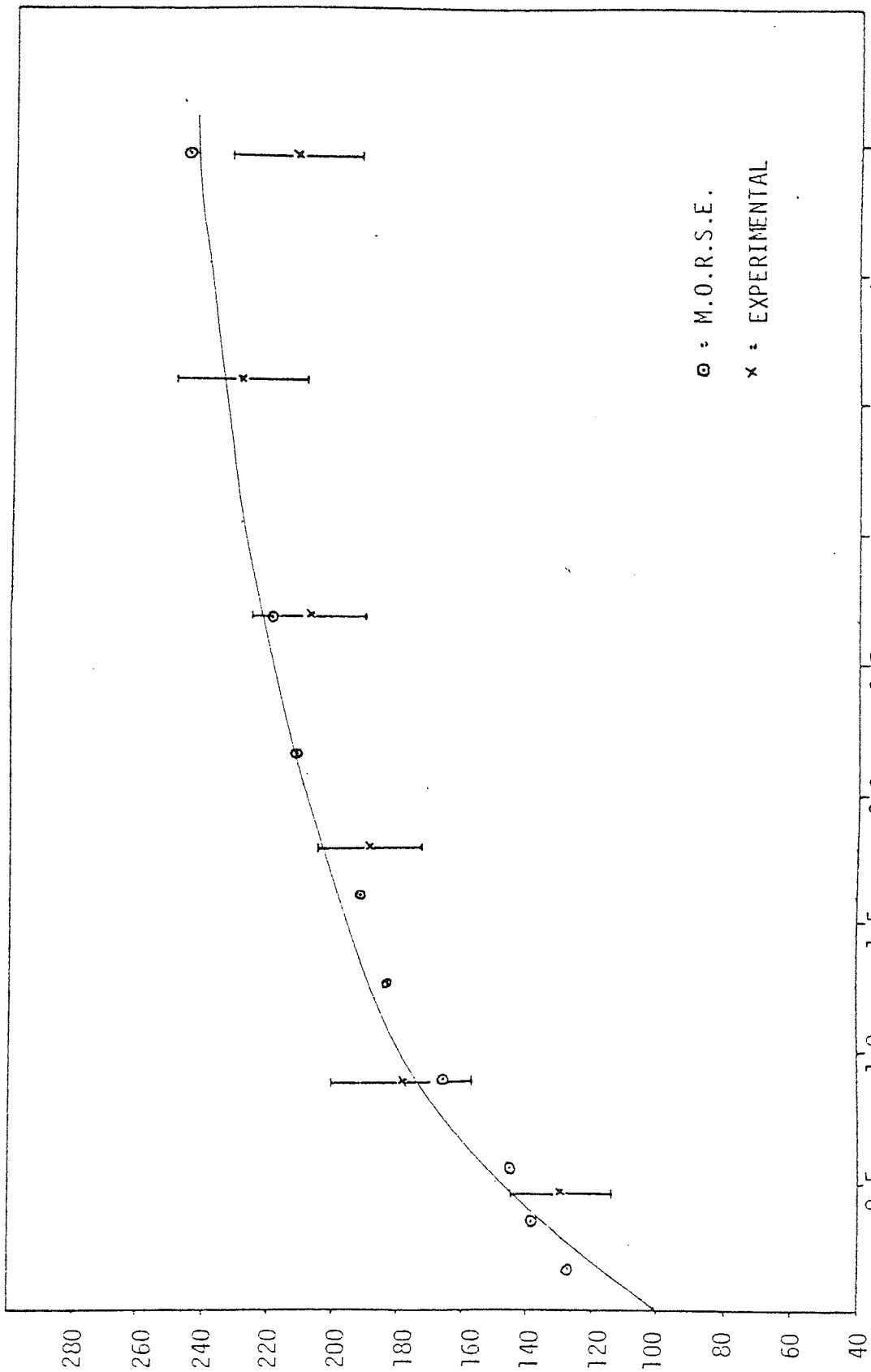

FIGURE 5.9 COMPARISON OF M.O.R.S.E. AND EXPERIMENTAL RESULTS FOR LEAD SAMPLES IN THE 1-2MeV REGION

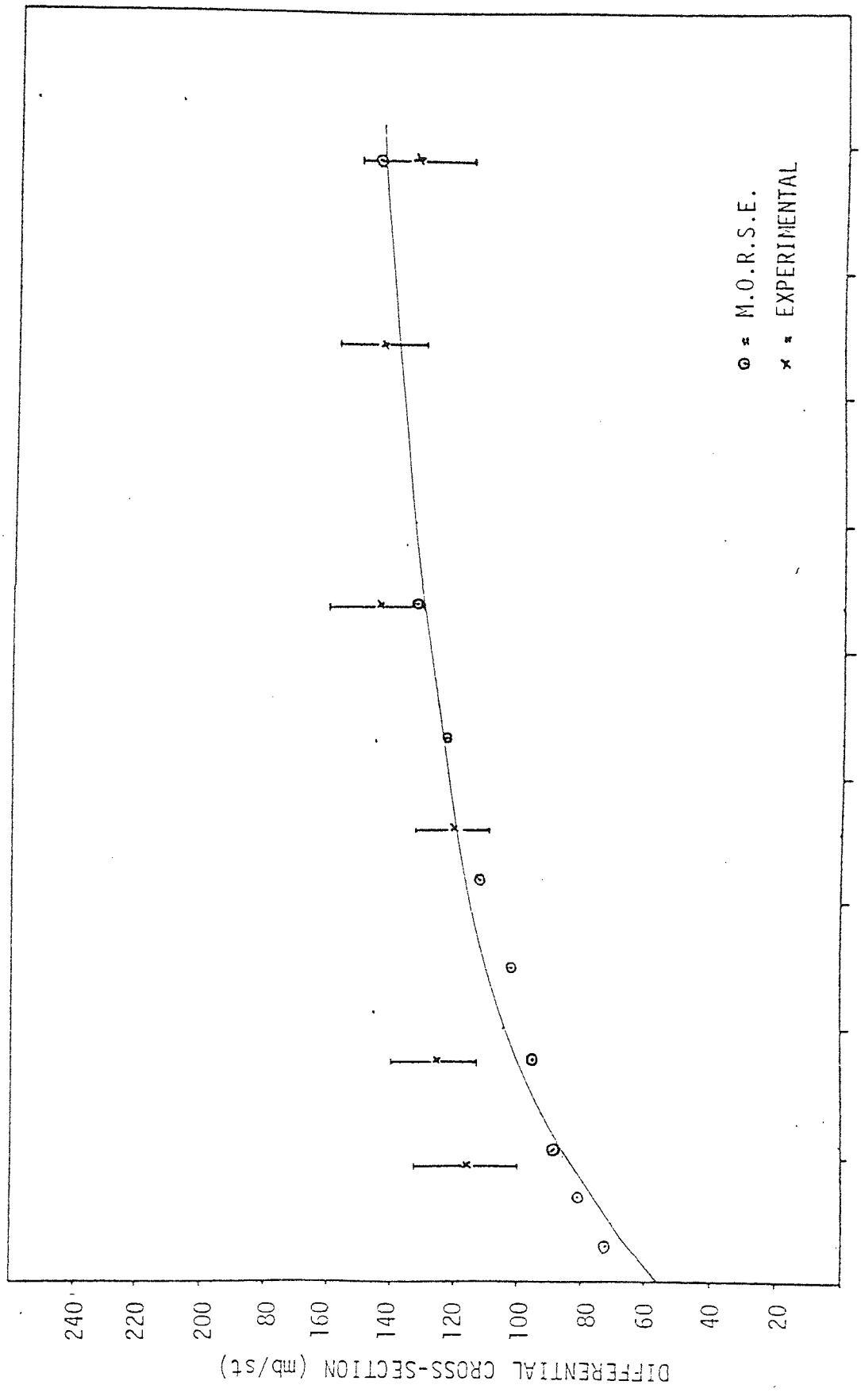

FIGURE 5.10 COMPARISON OF M.O.R.S.E AND EXPERIMENTAL RESULTS FOR LEAD SAMPLES IN THE 2-3MeV REGION

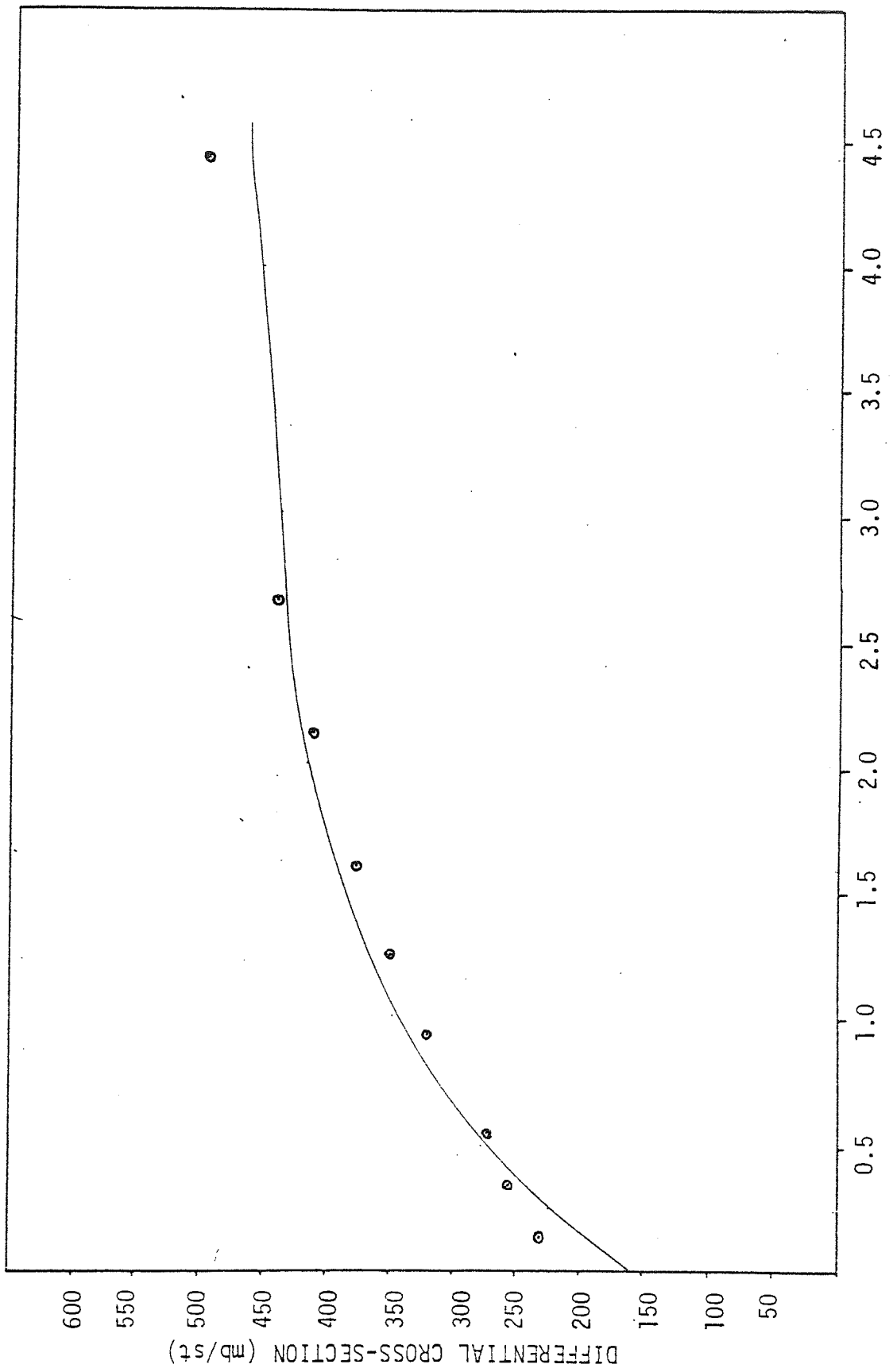

FIGURE 5.11 M.O.R.S.E. RESULTS FOR LEAD SAMPLES IN THE 0.4-1MeV

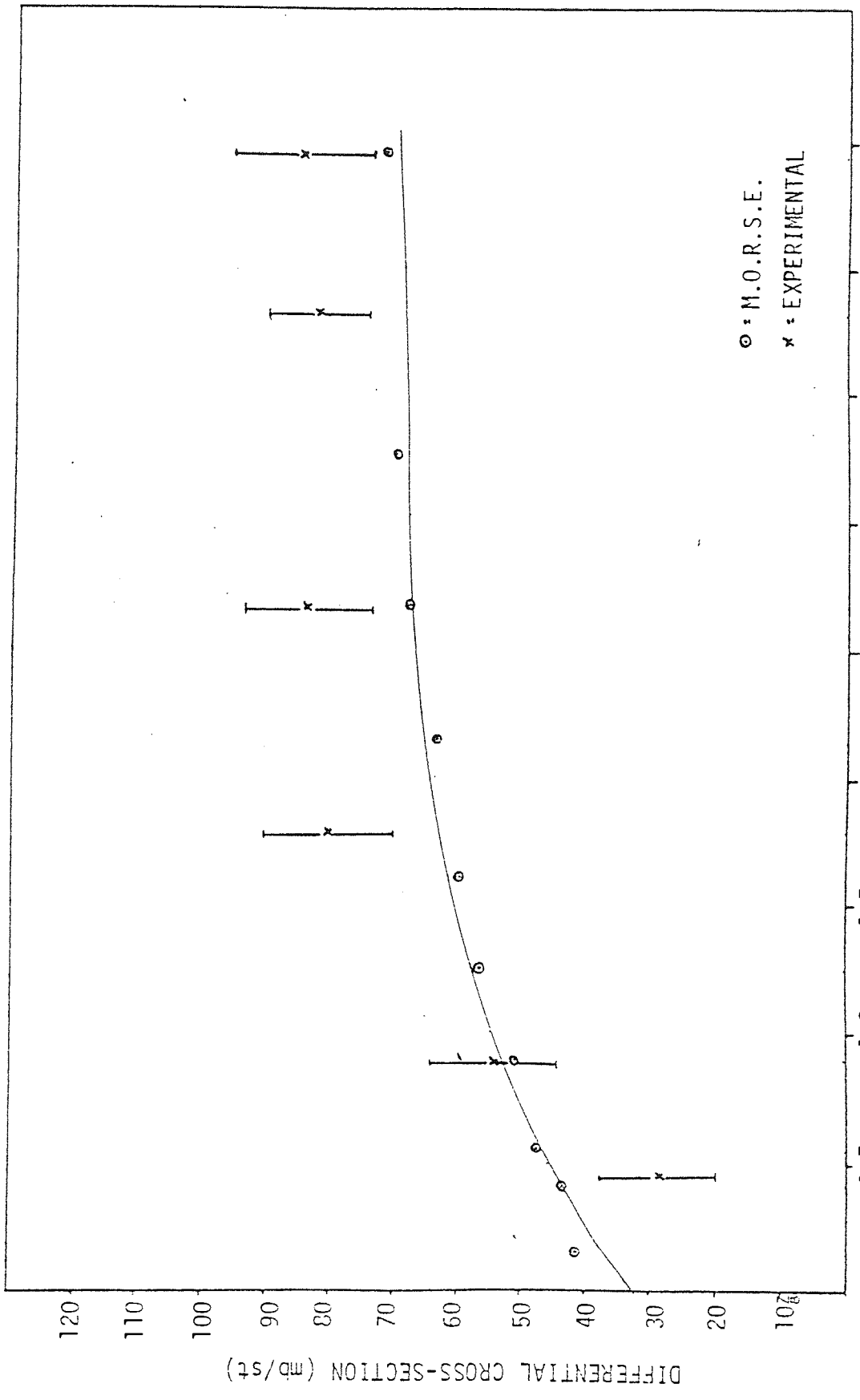

FIGURE 5.12 COMPARISON OF M.O.R.S.E. AND EXPERIMENTAL RESULTS FOR LEAD SAMPLES IN THE 3-4MeV REGION

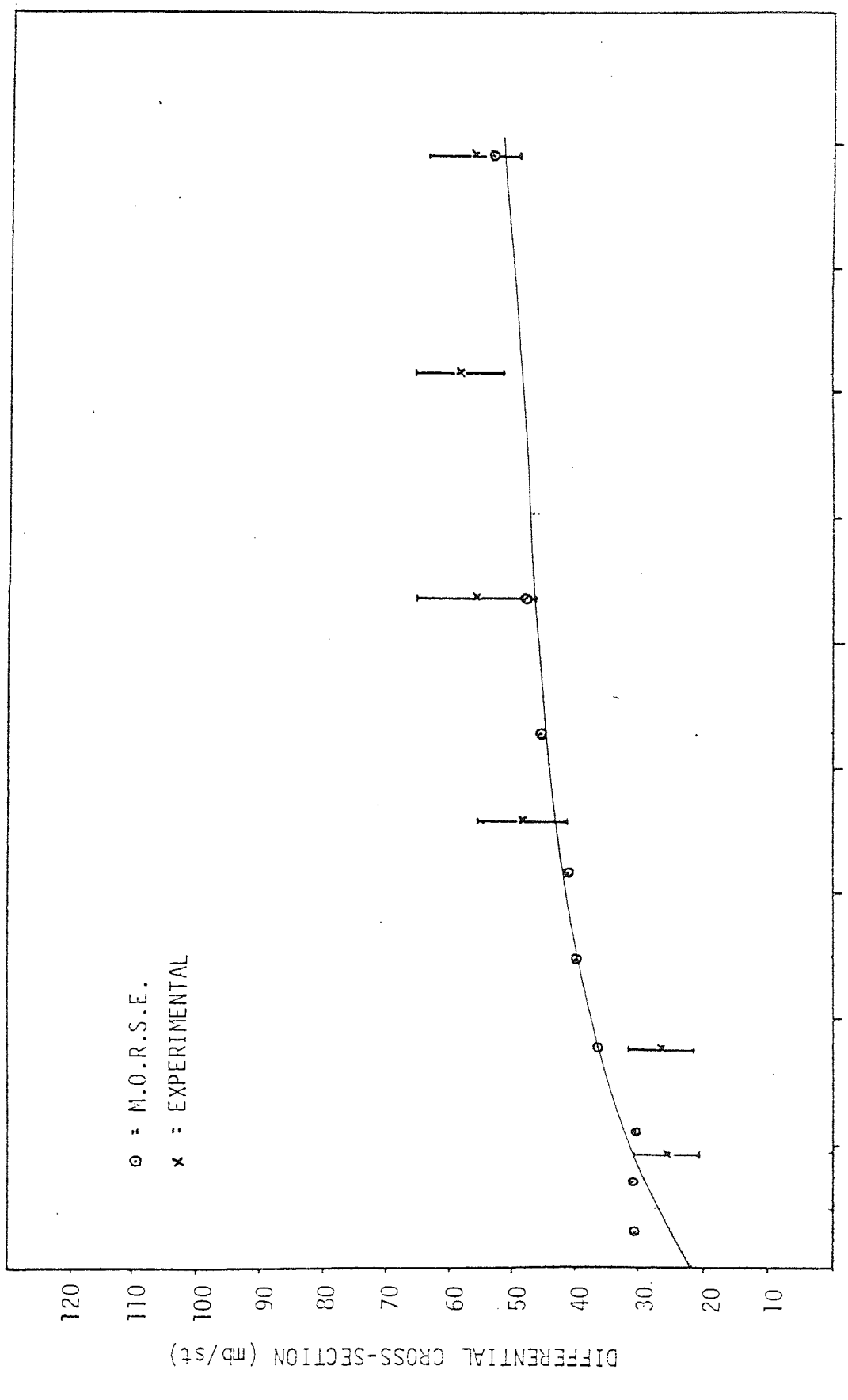

FIGURE 5.13 COMPARISON OF M.O.R.S.E. AND EXPERIMENTAL RESULTS FOR LEAD SAMPLES IN THE 4-5MeV REGION

5.7 Notes for Comparison of Theoretical and Experimental Multiple Scattering Effects in Iron samples

Table 5.5 overleaf gives the variation in cross-section with sample thickness, as predicted by M.O.R.S.E, for iron samples. The experimental results are taken from Al-shalabi[40] and reveal individual level cross-sections, for gamma rays produced from the first excited state 0.845MeV and second excited state 1.24MeV. As might be expected these results are lower than those predicted by M.O.R.S.E. in the same energy range. This is because, the cross-section predicted by M.O.R.S.E. includes the cross-section for all levels within a certain energy group. Thus for group 1:

$$\sigma_{g1} = \sigma_{L_1} + \sigma_{L_2} + \sigma_{L_3} \cdots\cdots \sigma_{LN}$$

σ_{Li} = Gamma ray production cross-section for i^{th} level.

Hence

$$\sigma_{gj} = \sum_{i=1}^{N} \sigma_{Li}$$

σ_{gj} = Gamma ray production cross-section predicted by M.O.R.S.E. for energy group j.

To compare M.O.R.S.E with Al-shalabi it was necessary to use the data of Western[60] et al. which gave the cross-section for all levels in iron between 1 and 2MeV except the 1.24MeV level. The M.O.R.S.E. results were then multiplied by the probability of decaying to the 1.24MeV level. This was calculated as:

$$P_{1.24} = \frac{\sigma_{o,1.24}}{\left(\sum_{i=1}^{N} \sigma_{Li} - 1.24\right) + \sigma_{o,\,1.24}}$$

where

$P_{1.24}$ = Probability of decaying to the ground state from the 1.24MeV level in the energy range 1-2MeV.

$\sum_{i=1}^{N} \sigma_{Li-1.24}$ = Gamma ray production cross-section for all levels except 1.24MeV in the 1-2MeV energy range as given by Western et al.

$\sigma_{o,1.24}$ = Gamma ray production cross-section for the 1.24MeV level is given by Al-shalabi.

Table 5.4 gives the corrected M.O.R.S.E values and the experimental values. As can be seen the agreement is quite good within the experimental uncertainties shown. It was not possible to make any other such comparisons for other levels but the M.O.R.S.E. results are given for all other energy ranges up to 3.0MeV along with the appropriate curve fit.

TABLE 5.5 TABULATED RESULTS FOR IRON (M.O.R.S.E.)

THICKNESS		ENERGY →	DIFFERENTIAL CROSS-SECTION (mb/st)				
(cm)	(mfp)		0.4-1.0MeV	1.0-1.5MeV	1.5-2.0MeV	2.0-2.5MeV	2.5-3.0MeV
0.9	0.2		93	60.2	20.6	14.5	15.0
2.0	0.44		103	66	23	18	18
5.0	1.10		147	82	29	21	20
9.0	1.96		178	92	33	25	22
11.0	2.39		196	98	36	27	24
18.0	3.92		225	108	39	30	27

TABLE 5.6 PREVIOUS RESULTS FROM ASTON[40] (EXPERIMENTAL)

THICKNESS		ENERGY OF LEVEL →	DIFFERENTIAL CROSS-SECTION (mb/st)	
(cm)	(mfp)		0.847MeV	1.24MeV
2.0	0.44		63.5 ± 0.5	35.2 ± 1.9
7.6	1.67		78.52 ±1.6	47.68 ±1.3
10.4	2.288		86.3 ± 4.3	48.66 ±1.8

TABLE 5.7 RESULTS FROM IRON AFTER USING CONTINUOUS GAMMA DATA FROM (REF.61) TO CORRECT GROUP 1-2MeV FOR THE 1.24MeV LEVEL

THICKNESS		ENERGY →	DIFFERENTIAL CROSS-SECTION (mb/st)
(cm)	(mfp)		1.24MeV
0.9	0.20		34.1
2.0	0.44		37.6
5.0	1.10		46.8
9.0	1.96		52.7
11.0	2.39		56.5
18.0	3.92		62.0

ERRORS IN M.O.R.S.E. RESULTS ± 5%

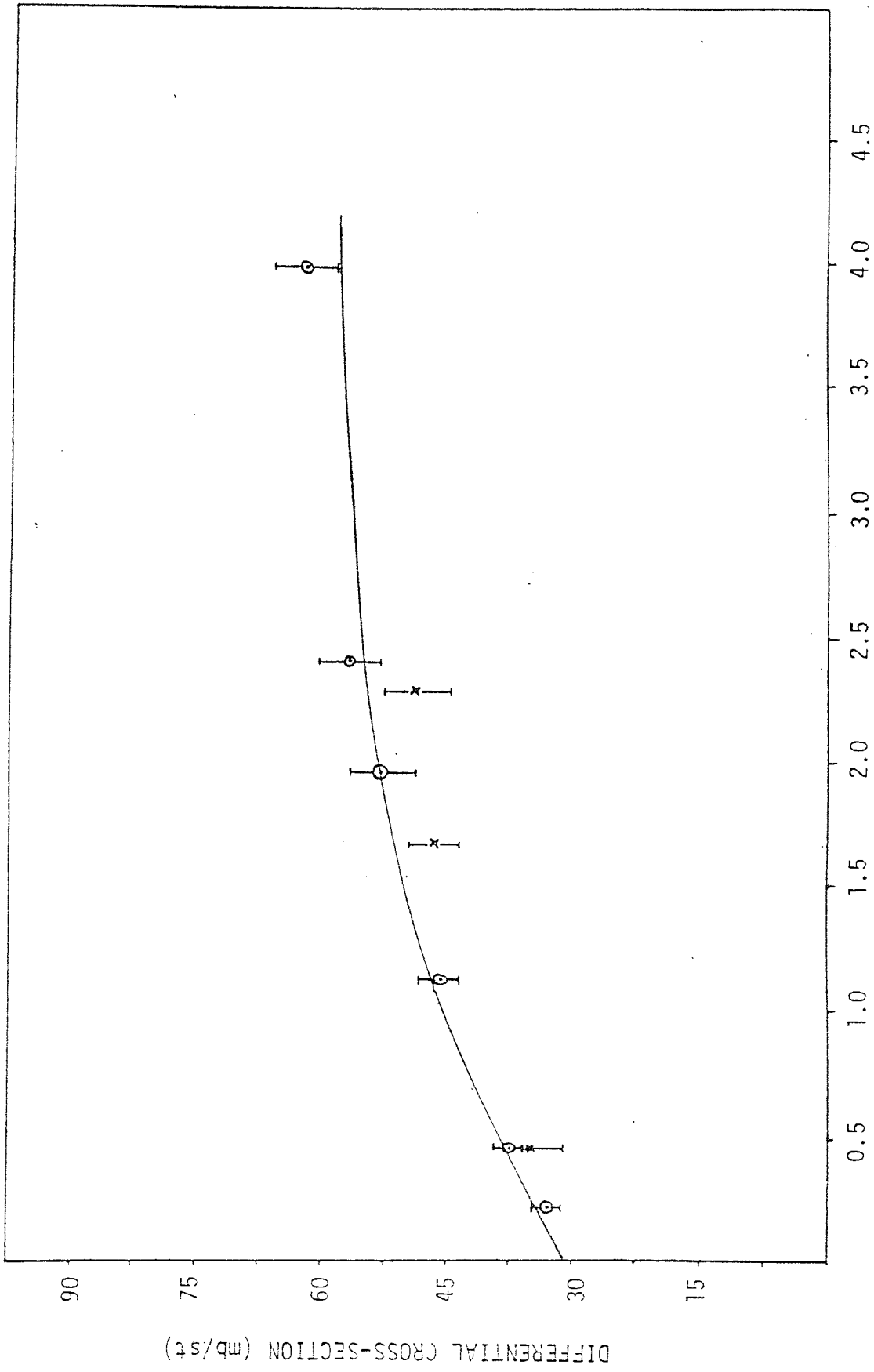

FIGURE 5.14 COMPARISON OF M.O.R.S.E. AND EXPERIMENT ON THE 1.24MeV LEVEL IN IRON SAMPLES

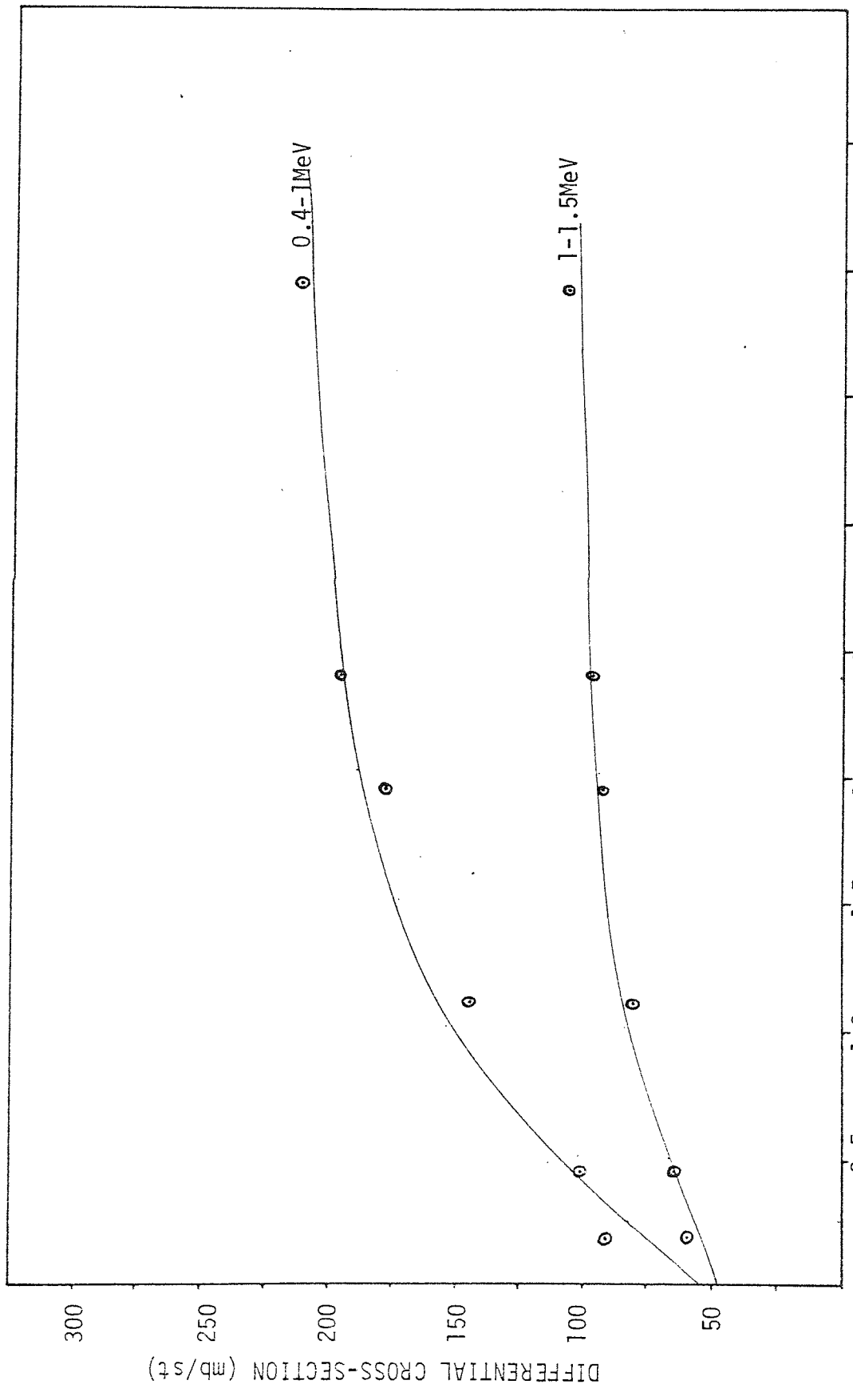

FIGURE 5.15 M.O.R.S.E. RESULTS FOR IRON IN THE 0.4-1MeV and 1-1.5MeV ENERGY GROUPS

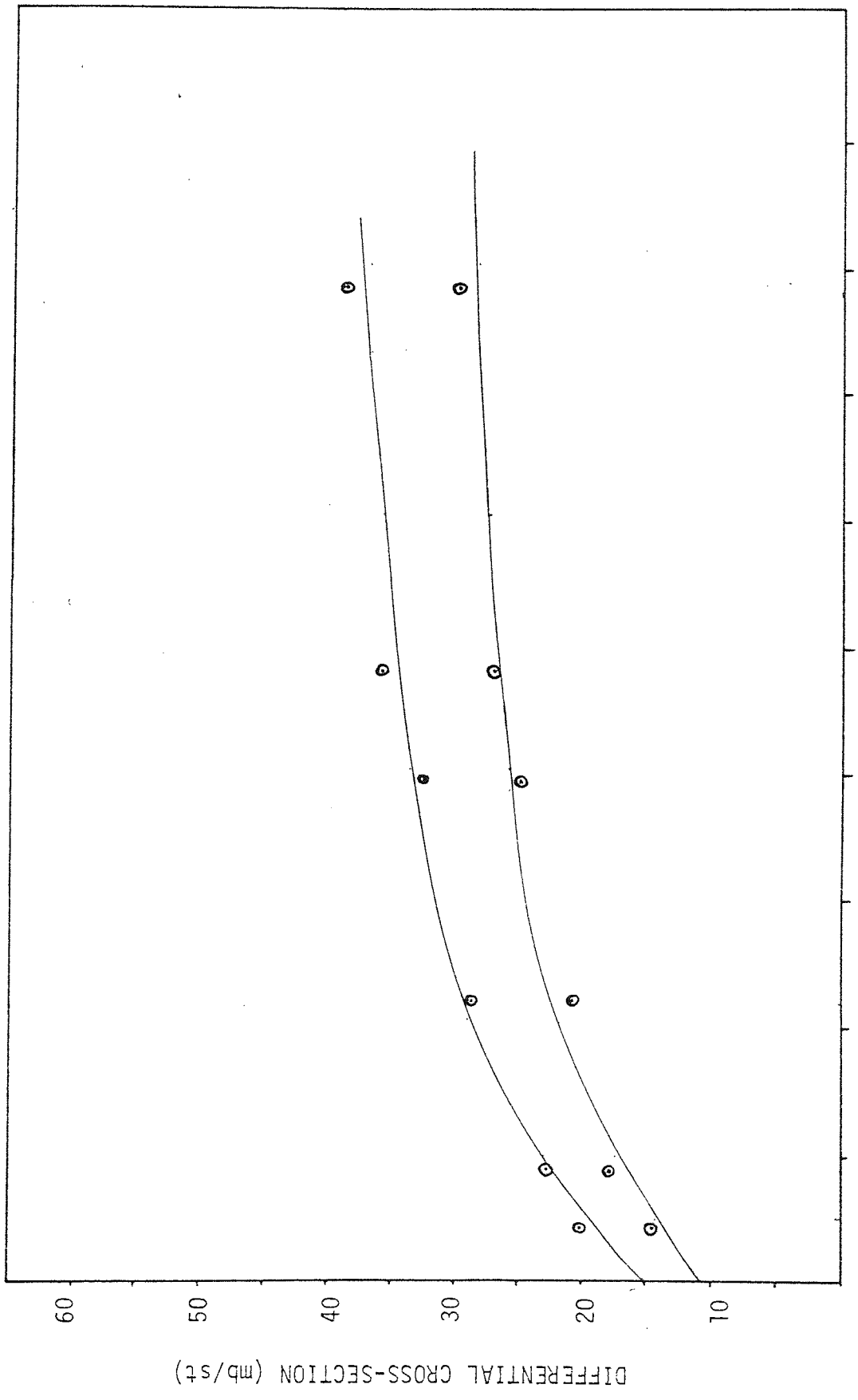

FIGURE 5.16 M.O.R.S.E. RESULTS FOR IRON IN THE 1.5-2MeV AND 2-2.5MeV ENERGY GROUPS

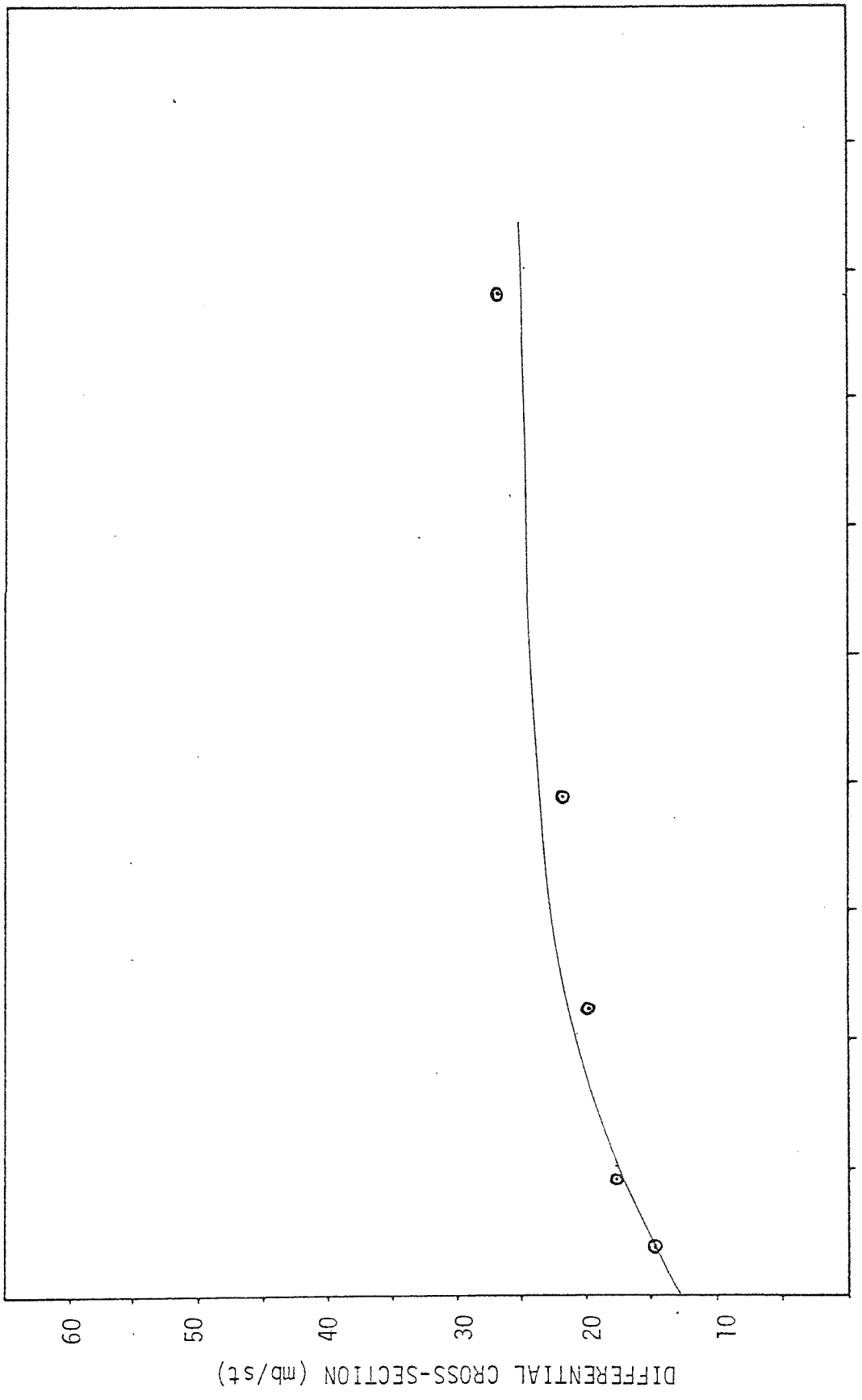

FIGURE 5.17 M.O.R.S.E. RESULTS FOR IRON IN THE 2.5-3.0MeV GROUP

CHAPTER 6

DISCUSSION OF RESULTS AND FINAL CONCLUSIONS

6.1 DISCUSSION OF RESULTS AND FINAL CONCLUSIONS

The results in general agree with the predictions of M.O.R.S.E. to within the estimated experimental uncertainties. Furthermore, both the M.O.R.S.E. results and the experimental results confirm the idea that the gamma ray cross-sections, may be expressed in terms of a theoretically zero thickness cross-section σ_0, and a theoretically constant cross-section σ_M at large sample thicknesses, varying exponentially in between. This latter value is usually reached by about 4 mean free paths.

The angular distributions are generally isotropic for the measurements made. This means that the 90° scattering results, which illustrate the variation in differential gamma ray production cross-section with thickness, may be multiplied by 4π to obtain the total gamma ray production cross-section at any thickness. The only case where the angular distribution is not found to be isotropic is for the 4-5MeV lead results. This also agrees with the assumption made in M.O.R.S.E. that gamma rays are emitted isotropically. The agreement between M.O.R.S.E and experimental is good for this energy range, especially since M.O.R.S.E. gamma ray generation probabilities are calculated at 90° from existing experimental data. However, if the lead results for the 4-5MeV region are required in blanket flux calculations at all angles and thicknesses, then the experimental angular distribution should be taken into account. The generalization for all angles can be approximated closely by using the shape of the thin sample angular distribution and multiplying the 90° thick sample cross-sections by a correction factor:

$$\frac{d\sigma(\theta)}{d\Omega}_{THICK} = K(\theta) \times \frac{d\sigma(90^\circ)}{d\Omega}_{THICK} \qquad 6.1$$

where:

$K(\theta)$ = Angular correction factor

$\frac{d\sigma(\theta)}{d\Omega}_{THICK}$ = Thick sample angular distribution measurement at angle θ

$\frac{d\sigma(90^\circ)}{d\Omega}_{THICK}$ = Thick sample angular distribution measurement at 90°

The constant $K(\theta)$ can be found using the Legendre polynomials:

$$K(\theta) = \frac{\frac{d\sigma}{d\Omega}(\theta)_{THIN}}{\frac{d\sigma}{d\Omega}(90^\circ)_{THIN}}$$

where:

$\frac{d\sigma}{d\Omega}(\theta)_{THIN}$ = Thin sample differential x-section measurement at angle θ

$\frac{d\sigma}{d\Omega}(90^\circ)_{THIN}$ = Thin sample differential x-section measurement at 90°

Hence:

$$K(\theta) = \frac{Ao + A_2\cos^2\theta + A_4\cos^4\theta}{Ao}$$

$$= 1 + \frac{A_2}{Ao}\cos^2\theta + \frac{A_4}{Ao}\cos^4\theta$$

which may be written:

$$K(\theta) = 1 + K_2\cos^2\theta + K_4\cos^4\theta$$

where $K_2 = \frac{A_2}{Ao}$ $\quad K_4 = \frac{A_4}{Ao}$

It is hoped that all the data contained in this work will be useful for fusion blanket calculations. The data will serve as a comparison for theoretical calculations and will enable the gamma ray flux, scattered into solid angle $d\Omega(\theta)$, with respect to incident neutrons in thick blanket materials, to be calculated. The flux may then be integrated over all incident neutron angles to obtain the total gamma ray flux entering a solid angle, or integrated over all neutron and gamma angles to obtain the total flux. The flux calculations may then be used to assist calculations of: neutron slowing down parameters, heat degradation within blanket materials and biological shielding calculations.

The work also shows that for thicknesses greater than 4 mean paths, the cross-section reaches a constant value of $d\sigma_M/d\Omega$. This in turn means that the gamma ray flux for a given neutron flux becomes constant even with further increases in thickness. It is not uncommon in design to expect blanket materials to be greater than four mean free paths thick, so that $d\sigma_M/d\Omega$ may be used for flux estimates.

6.2 Generalization

All measurements and theoretical work contained within this project is of an empirical nature, in that, the data may be used for the materials used and conditions described. What follows is an attempt to generalise the work, so that almost any element may be corrected for multiple scattering effects in gamma ray production cross-section measurements.

Nearly all known tabulated thin sample cross-section data is for thicknesses of 0.2 mean free paths or below. The reason

for this is that multiple scattering is negligible below this value. From the theoretical and experimental data contained in this project, the thin sample measured cross-section was taken to be at 0.2 mean free paths. Table 6.1 indicates the ratio of $\frac{d\sigma_o}{d\Omega}$ to $\frac{d\sigma}{d\Omega}(0.2)\text{THIN}$ for all the results illustrated.

From these values an average value was found:

$$\frac{\frac{d\sigma_o}{d\Omega}}{\frac{d\sigma}{d\Omega}(0.2)\text{THIN}} = 0.8$$

The standard deviation in this value for the given elements and energy ranges was calculated to be ± 11%.

From the above it can be seen that in general, for the accuracy quoted:

$$\frac{d\sigma_o}{d\Omega} = 0.8 \frac{d\sigma}{d\Omega}\text{ THIN} \qquad \ldots\ldots\ldots\ldots\ldots\ldots\ldots\ldots 6.2$$

Using equation (4.4) for the curve fitting we obtain:

$$\frac{d\sigma}{d\Omega}\text{ THIN }(0.2) = \left(\frac{d\sigma_M}{d\Omega} - \frac{d\sigma_o}{d\Omega}\right)(1 - \exp(-0.2)) + \frac{d\sigma_o}{d\Omega}$$

sub. in eqn.6.1 and write as:

$$\frac{d\sigma}{d\Omega}\text{ THIN }(0.2) = A\,(1-\exp(-0.2)) + 0.8\,\frac{d\sigma}{d\Omega}\text{ THIN}(0.2)$$

where:

$$A = \frac{d\sigma_M}{d\Omega} - \frac{d\sigma_o}{d\Omega}$$

$\frac{d\sigma_o}{d\Omega} / \frac{d\sigma}{d\Omega}$ (0.2)THIN	ELEMENT WITH GIVEN ENERGY RANGE
0.60	$^{7}_{3}Li$ 0.478MeV Level Experiment
0.60	$^{7}_{3}Li$ 0.478MeV Level M.O.R.S.E.
0.80	$^{56}F_e$ 1.24MeV Level M.O.R.S.E.
0.80	Pb 1-2MeV Experiment
8.85	Pb 1-2MeV M.O.R.S.E.
0.95	Pb 2-3MeV Experiment
0.85	Pb 2-3MeV M.O.R.S.E.
0.80	Pb 3-4MeV Experiment
0.90	Pb 3-4MeV M.O.R.S.E.
0.85	Pb 4-5MeV Experiment
0.85	Pb 4-5MeV M.O.R.S.E.
0.80	$^{56}F_e$ 1-1.5MeV M.O.R.S.E.
0.75	$^{56}F_e$ 1.5-2.0MeV M.O.R.S.E.
0.75	$^{56}F_e$ 2.0-2.5MeV M.O.R.S.E.
0.85	$^{56}F_e$ 2.5-3.0MeV M.O.R.S.E.

TABLE 6.1 RATIO OF $\frac{d\sigma_o}{d\Omega} / \frac{d\sigma}{d\Omega}$ (0.2)THIN FOR ALL WORK UNDERTAKEN IN PROJECT

Maximum deviation ± 11%

Maximum experimental uncertainties ± 25%

Rearranging the latter gives:

$$A = 1.16 \frac{d\sigma}{d\Omega} \text{ THIN} \quad \ldots\ldots\ldots\ldots\ldots\ldots\ldots\ldots 6.3$$

Furthermore:

$$\frac{d\sigma_M}{d\Omega} = A + \frac{d\sigma_o}{d\Omega} \quad \ldots\ldots\ldots\ldots\ldots\ldots\ldots\ldots 6.4$$

Equations 6.2, 6.3, and 6.4 may then be used in:

$$\frac{d\sigma}{d\Omega} = \left(\frac{d\sigma_M}{d\Omega} - \frac{d\sigma_o}{d\Omega}\right)\{1-\exp(-\Sigma_T x)\} + \frac{d\sigma_o}{d\Omega}$$

To give the exponential variation for any element in the periodic table. It should be emphasized however, that the above relies on the empirical constants determined and if the equation is taken to its extremes errors will result. For most practical purposes the equations will give $d\sigma/d\Omega$ to within a maximum uncertainty of about ±25%.

Other than present work, there is little data that can be used to test the above equations. Other independent observers of multiple scattering effects in ^{56}Fe are: Day[9] and Al-Shalabi[40] and have been previously mentioned in Section .

The following figures illustrate how well the above equations predict multiple scattering for gamma ray production cross-sections due to excitation of the 0.845MeV level in ^{56}Fe . Hitherto, it was not possible to deal with this cross-section because of the M.O.R.S.E. energy group structure.

For the work of Day[9], the average thin sample cross-section was taken to be 0.87 barns per nucleus. The empirical equations then give:

$$\sigma_o = 0.687 \text{ barns/nucleus}$$
$$\sigma_M = 1.7 \text{ barns/nucleus}$$

The table 6.2 illustrates the comparison of predicted and experimental cross-section values, along with the differences between the predicted points and experimental points.

The work of Al-Shalabi gives the differential cross-section at 90° to the incident neutron beam, for the excitation of the 0.845MeV level. The results are given over a larger range of mean free paths than Day, however, a thin sample cross-section was not given and was taken to be 51 mb/st from the work of Western et al.[60]. Table 6.3 and figure 6.2 illustrates how well the predicted points agree with the experimental points. The parameters are:

$$\frac{d\sigma_o}{d\Omega} = 40 \text{ mb/steradian}$$

$$\frac{d\sigma_M}{d\Omega} = 99 \text{ mb/steradian}$$

TABLE 6.2 COMPARISON OF DAY'S[9] RESULTS WITH THE THEORETICALLY PREDICTED RESULTS FOR THE GAMMA RAY PRODUCTION CROSS-SECTION DUE TO EXCITATION OF THE 0.845MeV LEVEL IN IRON

MEAN FREE PATH	GAMMA RAY PRODUCTION CROSS-SECTION		DIFFERENCE
	DAY (9) (barns/nucleus)	PREDICTED (barns/nucleus)	
0.02	0.85 ± 0.07	0.71	0.14
0.1	0.87 ± 0.07	0.78	0.09
0.2	0.91 ± 0.07	0.87	0.04
0.37	0.99 ± 0.08	1.0	0.01
0.7	1.13 ± 0.09	1.19	0.06

FITTING PARAMETERS:

σ_o = 0.687 barns/nucleus

σ_M = 1.7 barns/nucleus

Maximum Difference = 16% for 0.02 mean free paths

Average Difference = 0.068 barns/nucleus

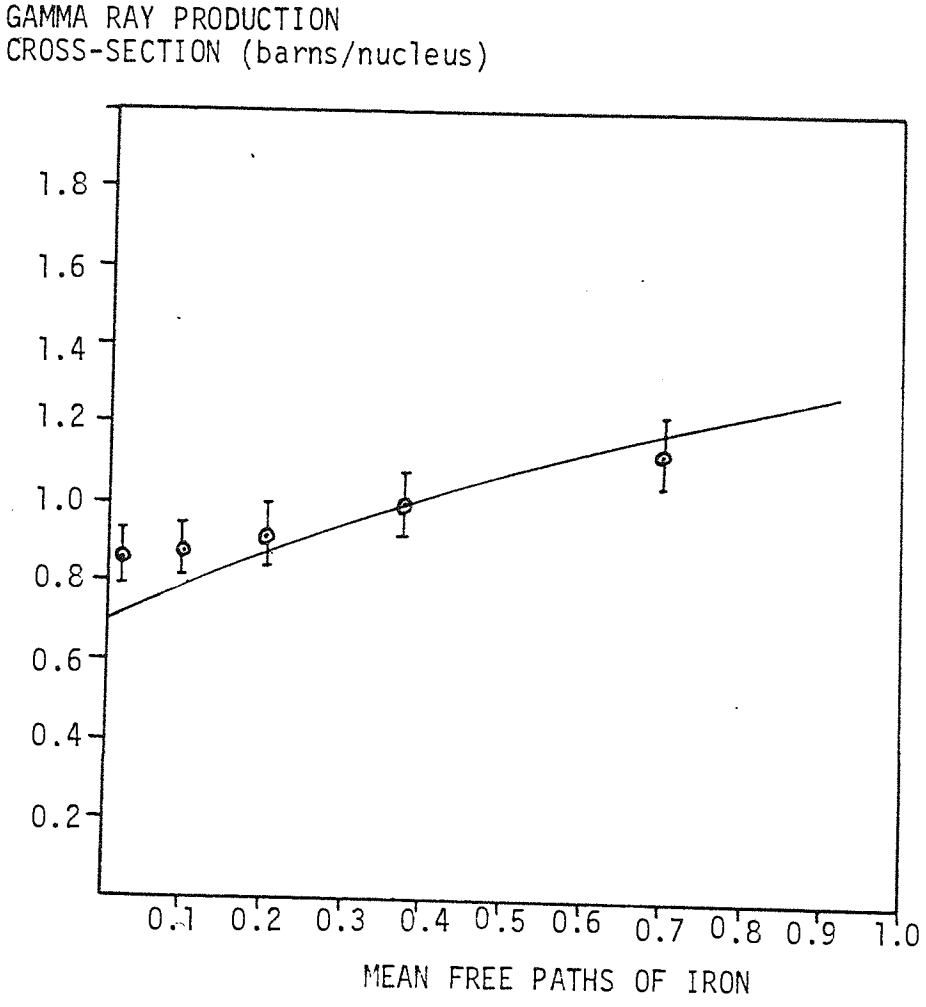

FIGURE 6.1 Comparison of Day's[9] results with predicted curve for the gamma ray production cross-section due to excitation of the 0.845MeV level in iron, with 2.6MeV neutrons.

TABLE 6.3 COMPARISON OF AL-SHALABI'S RESULTS WITH THE THEORETICALLY PREDICTED RESULTS FOR THE DIFFERENTIAL CROSS-SECTION AT 90° DUE TO THE EXCITATION OF THE 0.845MeV LEVEL IN IRON

MEAN FREE PATHS OF ^{56}Fe	DIFFERENTIAL GAMMA RAY PRODUCTION CROSS-SECTION AT 90° (mb/st)		DIFFERENCE
	AL-SHALABI[40]	PREDICTED	
0.2	51*	51	0
0.44	63.53	61	2.5
1.67	78.52	88	9.5
2.29	86.3	93	6.7

FITTING PARAMETERS:

$\frac{d\sigma_o}{d\Omega}$ = 40 mb/st

$\frac{d\sigma_M}{d\Omega}$ = 99 mb/st

Maximum difference = 12% for 1.67 mean free paths

Average difference = 4.7 mb/st

* Thin sample result from Western et al.[60]

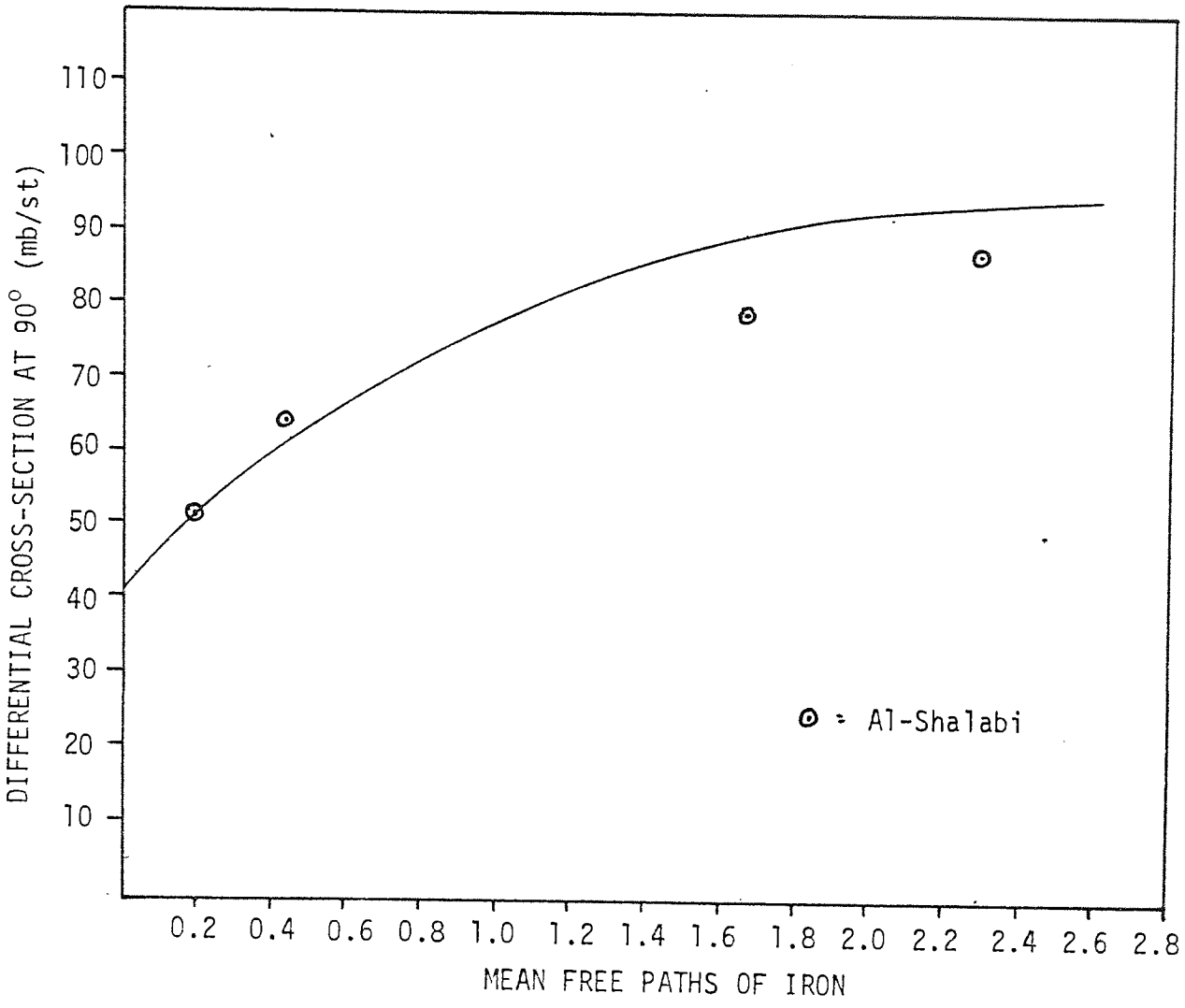

FIGURE 6.2 Comparison of Al-Shalabi's[40] results with the predicted curve for the differential gamma ray production cross-section at 90 degrees scattering angle, for the excitation of the 0.845MeV level in iron

The latter comparison of results indicate that, the assumptions used in predicting the variation of gamma ray cross-sections with thickness, are valid to within about ±20%. The largest deviation between predicted results and experimentally curve fit results, occurs for the extreme case of an infinitely thick LiF sample. At this extreme the predicted value is 35% lower than the experimentally extrapolated value. However, in general equations 6.2, 6.3, 6.4 predicted the effect of multiple scattering on gamma ray production cross-sections to accuracies of about ±20%.

6.3 Further Improvements

One of the assumptions made in the M.O.R.S.E. code, is that gamma rays are emitted isotropically. This is primarily due to the lack of information available, as input data, concerning an angular distribution of gamma rays. However, it has been shown by a number of workers: Al-Shalabi[40], Donahue[66] that gamma rays can be emitted anisotropically. One way of removing this limitation from M.O.R.S.E. would be to use equation 6.1, which includes the necessary angular information. In this way M.O.R.S.E. could be updated as more empirical data becomes available.

The largest source of error in the experimental cross-section measurements, was the uncertainty in measuring $P(\theta)$; the gamma ray counts in the peak (or energy region). The main difficulty in measuring this quantity arose from the estimation of the degraded Compton background. One method of estimating $P(\theta)$ more accurately would be to use the computing

technique outlined by R.L. Heath et al. In this method a line fit is made to standard NaI(Tl) detector responses. The response functions are then interpolated to give response function for almost any gamma ray energy. Using such a technique would require considerable time computing, but would inevitably yield more accurate experimental results.

Another way of reducing the effect of Compton background on a gamma ray spectrum would be to use a method of detection based upon an idea by Trail and Raboy[66]. The adaption to $(n,n'\gamma)$ cross-section measurements is now well known. It involves, as shown in Figure 6.3 a cylindrical crystal (NaI(Tl)) surrounded by an annular shaped crystal. The annular detector is placed in anti-coincidence with the cylindrical inner detector. The whole arrangement should be enclosed in a shield, as in the closed geometry situation used here. The idea is that, Compton scattered radiation from the inner detector is also detected by the annular detector since the detectors are in anti-coincidence most of the Compton scattered gamma rays are not counted and the resulting gamma ray spectra are extremely clean.

The use of such a detector, with time of flight coincidence gating would be a considerable improvement for further research in this current field.

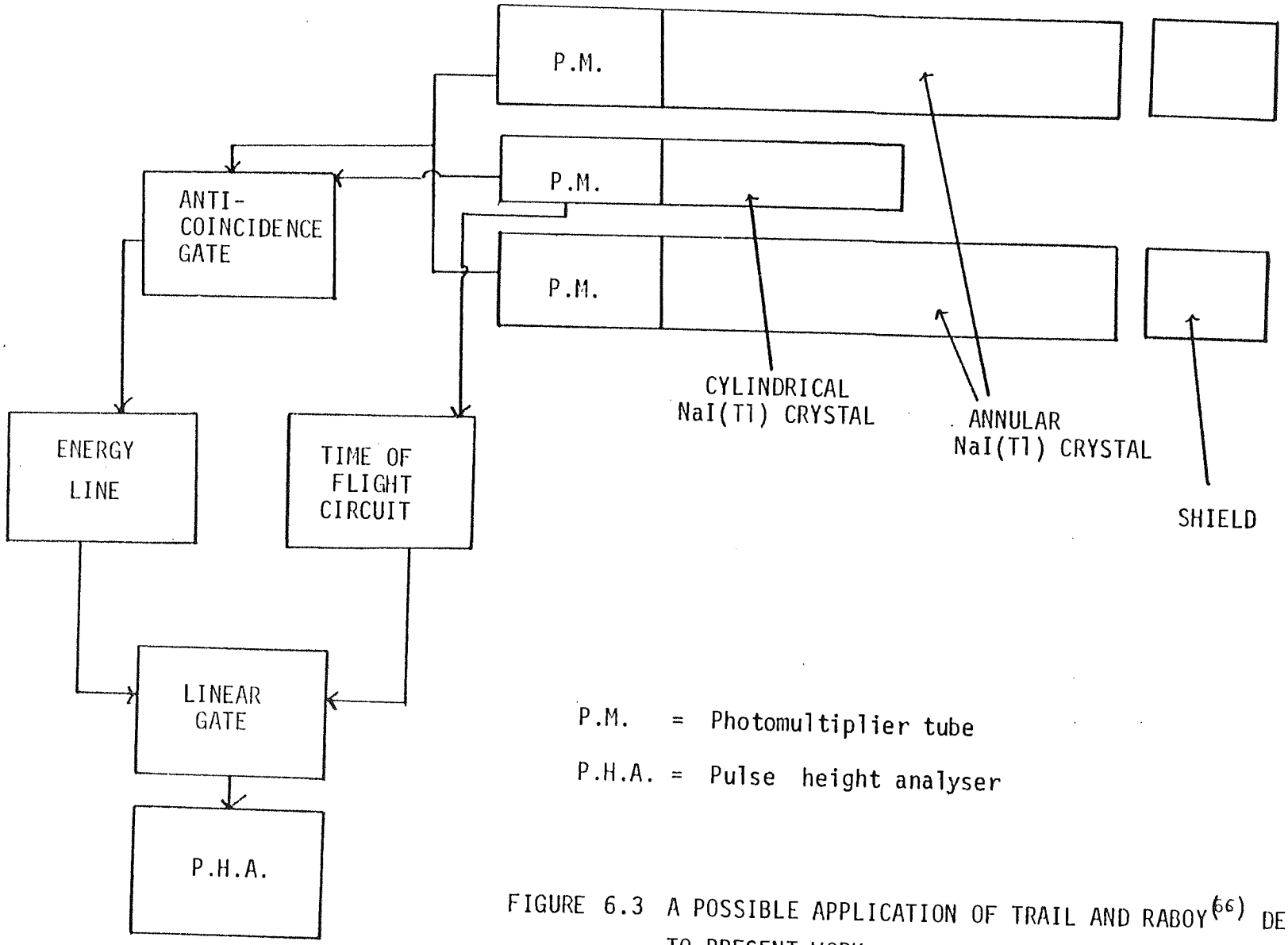

P.M. = Photomultiplier tube

P.H.A. = Pulse height analyser

FIGURE 6.3 A POSSIBLE APPLICATION OF TRAIL AND RABOY[66] DETECTOR TO PRESENT WORK

APPENDICES

APPENDIX 1

PROGRAMME IN BASIC FOR GEOMETRY FACTOR CALCULATION

```
1.  PRINT "GEOMETRY FACTOR PROGRAMME"
2.  INPUT "THETA"; T: PRINT T
3.  INPUT "SOURCE TO SAMPLE DISTANCE"; X1: PRINT X1
4.  INPUT "SAMPLE THICKNESS"; X2: PRINT X2
5.  H1 = X1 * TAN (3.18*π/18Ø)
6.  H2 = X1 * TAN (6.34*π/18Ø)
7.  B = SQR(H1↑2 + H2↑2)
8.  X = SQR(X1↑2 + B↑2): Z9 = 2*H2
9.  H3 = (X1 + X2) *TAN (3.18*π/18Ø)
10. H4 = (X1 + X2) *TAN (6.34*π/18Ø): Z8 = 2*H4
11. A = SQR (H3↑2 + H4↑2)
12. Y = SQR((L X1 + X2)↑2 + A↑2)
13. L = Y - X
14. Z = Z*H3
15. G = Z / (Ø.9985*L) - Ø.Ø555533
16. G1 = 1/G
17. B1 = ATN(G1)
18. L1 = (L* Ø.9985)/(SIN(B1))
19. L2 = L1*Ø.9938Ø
20. A1 = L2*(Z9+Z8)/2
21. C = π/2 - B1: C1 = C*18Ø/π
22. A2 = SIN(T*π/18Ø + C)*A1
23. G4 = A2/45.6
24. PRINT "THETA" = "T"DEG."
25. PRINT "GEOMETRY FACTOR= "G4
26. END.
```

APPENDIX 2

LEGENDRE POLYNOMIAL FITTING

The reactions of the type X(a,b)Y are described by an equation:

$$\sigma(\theta) = Ao + A_2Cos^2\theta + A_4Cos^4\theta$$

Let $Y_i = \sigma(\theta)$
And $X_i = Cos\theta$

Then by minimising the square of the deviations for n data points a fit may be made based upon the least squares fit.

The deviations will be expressed by:

$$\sum_{n=1}^{n} \{Y_i = (Ao + A_2X^2 + A_4X^4)\}^2$$

Differentiating wrt Ao, A_2 and A_4 respectively and equating to zero one obtains:

$$\Sigma Y_i = na_o + a_2\Sigma X_i^2 + a_4\Sigma X_i^4$$

$$\Sigma Y_i X_i^2 = a_o\Sigma X_i^2 + a_2\Sigma X_i^4 + a^4\Sigma X_i^6$$

$$\Sigma Y_i X_i^4 = a_o\Sigma X_i^4 + a_2\Sigma X_i^6 + a_4\Sigma X_i^8$$

Where ai gives best estimate of Ai.

The equations may be solved by Cramer'srule.

Error estimation in curve fit

If a_o, a_2 and a_4 are the fitted coefficients then the residuals are given by:

$$d_i = Y_i = (a_o + a_2X_i^2 + a_4X_i^4)$$

And the standard error of which is:

$$\alpha^2 = \frac{\sum_{n=1}^{n} d_i^2}{n-m}$$

m = 3 (number of coefficients)

Using the method by Topping[67] the errors α_i are given by:

$$\frac{\alpha_o^2}{\begin{vmatrix} \Sigma X_i^4 & \Sigma X_i^6 \\ \Sigma X_i^4 & \Sigma X_i^8 \end{vmatrix}} = \frac{\alpha_2^2}{\begin{vmatrix} n & \Sigma X_i^4 \\ \Sigma X_i^4 & \Sigma X_i^8 \end{vmatrix}} = \frac{\alpha_4^2}{\begin{vmatrix} n & \Sigma X_i^2 \\ \Sigma X_i^2 & \Sigma X_i^4 \end{vmatrix}} = \frac{\alpha^2}{\Delta}$$

Where:

$$\Delta = \begin{vmatrix} n & \Sigma X_i^2 & \Sigma X_i^4 \\ \Sigma X_i^2 & \Sigma X_i^4 & \Sigma X_i^6 \\ \Sigma X_i^4 & \Sigma X_i^6 & \Sigma X_i^8 \end{vmatrix}$$

where summations are 1 to n.

The angular distribution can then be expressed:

$$\sigma(\theta) = a_o \pm \alpha_o + (a_2 \pm \alpha_2)\cos^2\theta + (a_4 \pm \alpha_4)\cos^4\theta$$

APPENDIX 3

One dimensional consideration of multiple scattering

DIAGRAM OF SAMPLE

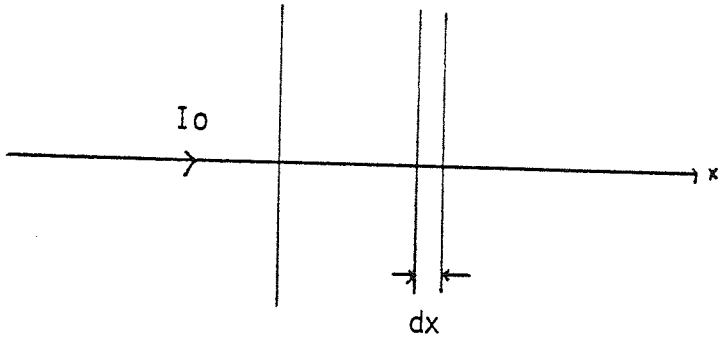

The sample is considered in 2D from $x = 0$ to $x \to \infty$.

It is assumed that there is an incident neutron beam of flux Io which attenuates to a value of zero through the sample as $x \to \infty$. In keeping with this argument we assume there exists an initial gamma ray production cross-section σ_o corresponding to an infinitismal sample thickness dx. Since the neutron flux is eventually attenuated to zero, then it is reasonable to assume that the gamma ray flux resulting from excitation of nuclei will reach a constant value σ_M as $x \to \infty$. Furthermore, it is assumed that the increase in gamma ray production cross-section in element dx, $d\sigma$ is proportional to the probability of neutron absorption and the thickness dx:

$$d\sigma \propto e^{-\Sigma_T x}\, dx$$

Σ_T = TOTAL MACROSCOPIC CROSS-SECTION

$$d\sigma = A\, e^{-\Sigma_T}\, dx$$

A = Constant of proportionality

Integrate with respect to x:

$$\sigma = -\frac{Ae^{-\Sigma x}}{\Sigma_T} + B \quad \ldots\ldots\ldots\ldots\ldots\ldots\ldots\ldots\ 1$$

B = Constant of integration

Using the initial conditions:

When $x = 0 \quad \sigma = \sigma_o$

$$\sigma_o = -\frac{A}{\Sigma_T} + B \quad \ldots\ldots\ldots\ldots\ldots\ldots\ldots\ldots\ldots\ldots 2$$

When $x \to \infty \quad \sigma = \sigma_M$

$$\sigma_M = B \quad \ldots\ldots\ldots\ldots\ldots\ldots\ldots\ldots\ldots\ldots 3$$

Substitute 3 into 2:

$$A = (\sigma_M - \sigma_o)\,\Sigma_T$$

Substitute the latter into 1:

$$\sigma = (\sigma_o - \sigma_M)e^{-\Sigma_T x} + \sigma_M$$

which may be written:

$$\sigma = (\sigma_M - \sigma_o)\,\{1-e^{-\Sigma_T}\} + \sigma_o$$

This can then be expressed as a differential cross-section formula:

$$\frac{d\sigma}{d\Omega} = \left(\frac{d\sigma_M}{d\Omega} - \frac{d\sigma_o}{d\Omega}\right)\{1-\exp(-\Sigma_T x)\} + \frac{d\sigma_o}{d\Omega}$$

REFERENCES

1. K. SAKO, M. OHTA, Y. SEKI, H. YAMATO, T. HIRAOKA, K. TANAKA, N. ASAMI, S. MORI *Conceptual design of a gas-cooled Tokamak reactor* Proceedings of IAEA Workshop, UK, pp27-37 29 January (1974)

2. F.H. TENNEY *A 2100 MW(e) fusion power plant* Proceedings of IAEA Workshop, UK, pp17-27 29 January (1974)

3. S.E. HUNT *Fission Fusion and the Energy Crisis* Pergamon Press (1974)

4. A.J. COX *The differential cross-section measurements for the scattering of 14MeV neutrons and associated gamma rays* Dept. Phys. Aston University in Birmingham, England Atomki Közemenyek Vol. 18 pp259-271 (1976)

5. M.C. JANICKI AND A.J. COX *Study of elastic scattering of 2-3MeV neutrons by ^{40}Ca and ^{32}S using an associated particle time of flight spectrometer* International Journal of Applied Rad. Isotopes Vol. 30 pp439-445 (1979)

6. R.L. CLARKE AND P. PERRIN *Elastic and inelastic scattering of neutrons from fluorine* Nucl. Phys. Vol. A147 pp174-182 (1970)

7. AL-SHALABI AND A.J. COX *Angular distributions of gamma rays produced by scattering of 14MeV neutrons in large samples of concrete* Dept. Phys. Aston University in Birmingham, England (1981)

8. R.B. DAY *Gamma rays from inelastic scattering* (from *Progress in fast neutron physics*) G.C. PHILLIPS, J.B. RISER AND J.R. MARION, The University of Chicago Press

9. R.B. DAY *Gamma rays from neutron inelastic scattering* Phys. Rev. Vol. 102 No. 3, pp767-787 (1956)

10. *General purpose Monte Carlo multigroup neutron and gamma ray transport code with combinatorial geometry* ORNL-4972 Contract No. W-7405-ENG-26 (1975)

11. J. BENVISTE AND J. ZENGER *Information on the neutrons produced in the T(d,n)α reaction* UCRL-4266 (1954)

12. K. ALLENBY *The study of gamma rays associated with the inelastic scattering of neutrons* Thesis. Phys. Dept. Aston University in Birmingham, England (1974)

13. J.P. CONNER, T.W. BONNER AND J.R. SMITH *A study of the ^{3}H $(d,n)^{4}He$ reaction* Phys. Rev. Vol. 88, pp468-473, (1952)

14. B.T. PRICE, C.C. HORTON, K.T. SPINNEY *Radiation shielding* Pergamon Press (1957)

15. W. HEITTER *Quantum theory of radiation* 3rd edition, Oxford Press (1954)

16. J.W. ALLISON *Gamma ray absorption coefficients of various materials allowing for bremstratilung and other secondary*

radiations Australian J. Phys. Vol. 14, pp443-468 (1961)

17. F. SAUTER *In German* Ann. d. Phys. Vol. 11, pp454-458 (1931)

18. M. STOBBE *In German* Ann. d. Phys. Vol. 7, p661 (1930)

19. F. PERRIN *In French* Comptes Rendus. Vol. 197, pp1100-1103 (1934)

20. G.R. WHITE U.S.A. Nat. Bureau of Standards rep. 1003 (1934)

21. J.A. VICTOREEN *Calculation of x-ray mass absorption coefficients* J. of Appl. Physc. Vol. 20, pp1141-1147 (1949)

22. G.W. GRODSTEIN National Bureau of Standards Circular 583 (1957)

23. D.E. BAYNHAM *The design of a neutron time of flight spectrometer and its use in the study of scattering from* $^{14}_{7}N$ *at 14.2MeV* University of Aston, Birmingham, England (1971)

24. H.M. MANN AND J.L. YNTEMA *Heavy particle radiation damage effects in Si(Li) detectors* I.E.E.E. Trans. Nucl. Sci. N.S. 11, No. 3, pp201-205 (1964)

25. T. ROZMANN AND K.G. ZIMMER *The damage to plastic scintillators* International J. Appl. Radiation Isotopes Vol. 3, pp36-42 (1958)

26. G.K. O'NEIL *Time of flight measurements of the inelastic scattering of 14.8MeV neutrons* Phys. Rev. Vol.95, pp1235-1245 (1954)

27. J.B. MARION AND F.C. YOUNG *Nuclear reaction analysis* North Holland (1968)

28. W. WHALING *Handbook der physik* Vol. XXXIV (1930)

29. GEOFFRY G. ECHNDZ AND J.W. POSTEN *Principles of radiation detection* Pergamon Press

30. *Neutron cross-sections* BNL-325 (1958)

31. C.D. ZERBY, A. MEYER AND R.B. MURRAY (ORNL) *Intrinsic line broadening in NaI(Tl) Gamma ray spectrometers* Nucl. Inst. and Meth. Vol. 12, pp115-123 (1961)

32. G.G. KELLY, P.R. BELL, R.C. DAVIS AND H.N. LAZAR *Intrinsic scintillator resolution* I.R.E. Trans. Nucl. Sci. NS-3, pp57-58 (1956)

33. F.S. EBY AND W.K. JENTSHKE *Fluorescent response of NaI(Tl) to nuclear radiatons* Phys. Rev. Vol. 96, pp911-920 (1954)

34. K.P. NICHOLSON AND G.F. SNELLING *Some lithium iodide phosphors for slow neutron detection* Brit. J. Appl. Phys. Vol. 6, pp104- (1955)

35. Barn Book of Cross-sections

36. J.J. VAN LOEF AND D.A. LIND *Measurements of inelastic cross-sections for fast neutrons* Phys. Rev. Vol. 101, pp103-113 (1956)

37. R.W. ENGSTROM, R.G. SLOVDENHEIMER AND A.M. GLOVER *Production testing of multiplier tubes* Nucleonics, Vol.10, No. 4, pp58-62 (1952)

38. R.D. CONNER AND M.K. HUSSAIN *Some factors affecting the gain and resolution of photomultiplier tubes* Nucl. Inst. and Meth Vol. 6, pp337-342 (1960)

39. R.L. HEATH *Recent developments in scintillation spectrometry* IRE Trans. Nucl. Sci. NS-9, No. 3, pp294-304 (1962)

40. AL-SHALABI *A study of the gamma rays associated with the inelastic scattering of neutrons in extended samples* Thesis, Aston University in Birmingham, England (1981)

41. F. PETER, F. BERRY *Gamma ray attenuation coefficients* Nucleonics, Vol. 19, pp62-62 (1962)

42. K.A. CONNELL *The study of gamma rays produced in the inelastic scattering of neutrons* Thesis, Aston University in Birmingham, England (1972)

43. W.A. WENZEL AND W. WHALING *The stopping cross-sections for D_2O ice* Phys. Rev. Vol.87, pp499-503 (1953)

44. ABBANDANO *Gamma rays resulting from non-elastic processes of 14.2MeV neutrons with sodium, magnesium, silicon, sulphur, titanium, chromium and iron* Journal of Nucl. Energy, Vol.27, pp227-239 (1973)

45. R.L. HEATH *Computer techniques for analysis of gamma ray spectra obtained with NaI and lithium ion drifted germanium detectors,* Nucl. Inst. and Meth. Vol. 43, pp209-229 (1966)

46. R.L. HEATH, R.G. HELMER, L.A. SCHIMITTROTH AND G.A. CARIER *A method for generating gamma ray shapes for the analysis of spectra* Nucl. Inst. and Meth. Vol. 47, pp281-304 (1967)

47. M.J. BERGER AND S.M. SELTZER *Response functions for sodium iodide scintillator detectors* Nucl. Inst. and Meth. Vol.104, pp317-332 (1972)

48. D.F. COVELL *Determination of gamma ray abundance directly from the absorption peak* Analytical Chemistry, Vol. 31, No. 11, pp1787-1790 (1959)

49. D.O. NELLIS, R.W. BENJAMIN, J.B. ASHE, J.T. PRODHOMME, I.L. MORGAN *Gamma ray production cross-sections for 4.0 to 14.8MeV neutrons* TID 20689 Contract at (40-1)-2791, pp29-40, (1961)

50. T. LAURITZEN AND F. AJZENBERG-SELOVE *Energy levels of light nuclei* Nucl. Phys. Vol.78, pp1-175 (1966)

51. D. DEHNHARD AND M. HINTZ *Octupole and Quadrupole Transition rates in ^{19}F from 15MeV Deuterons* Phys. Rev. Vol.1, pp460-467

52. G.L. MORGAN *Cross-sections for $^{7}Li(n,xn)$ and $^{7}Li(n,n'\gamma)$ reactions between 1 and 20 MeV* ORNL-TM-6247, ORNL (1978)

53. J.K. DICKENS, G.L. MORGAN AND T.A. LOVE *Gamma ray production due to neutron interactions with fluorine and lithium for incident neutron energies between 0.55 and 20MeV-tabulated cross-sections* ORNL-TM-4538 (1974)

54. R.J. BAUVE, L. STEWART AND M. BATTAT *ENDF/B-IV data file for ^{7}Li (Mat 1272)* (1974)

55. D. STROMINGS, J.M. HOLLANDER AND G.T. SEABORG *Table of isotopes* Rev. Modern Phys. Vol.30, No.2, Part 2

56. J.T. PRUD'HOMME, P.L. OKHUYSEN AND I.L. MORGAN *Non-elastic scattering of fast neutrons* Phys. Rev. Vol.118, No.4, pp1059-1062 (1960)

57. A. BRATENALL, M.J. PETERSON AND J.P. STAERING *Neutron total cross-sections in the 7 to 14MeV region* Phys. Rev. Vol.110, No.4, pp927-933 (1958)

58. ENGESSER AND W.E. THOMPSON *Gamma rays resulting from the interactions of 14.7MeV neutrons with various elements* Journal of Nucl. Energy, Vol.21, pp487-507 (1967)

59. V.E. SCHERRER, R.B. THEUS AND W.R. FAUST *Gamma rays from the interaction of 14MeV neutrons with various materials* Phys. Rev. Vol.91, No.6, pp1476-1478 (1953)

60. G.T. WESTERN, F.L. GIBBONS, R.C. BAIRD, J.R. WILLIAMS *The interactions of 14.6MeV neutrons in iron, lithium 7 and carbon* Nuclear Aerospace Research Facility (1965) Techn. rep. no. WL-TR-64-140 Contract No. AF 29(601)-6213

61. L. CRANBERG *Neutron scattering by ^{235}U, Pu and ^{238}U* LA-2177 (Contract W-7405-Eng-36) (1959)

62. S.P.T. ANVARIAN *A study of fast neutron scattering in large samples* Thesis, University of Aston in Birmingham, England (1982)

63. YU A. SHREIDNER *The Monte Carlo Method* Pergamon Press (1966)

64. D. DICKINSON AND G.E. WHITESIDES *The Monte Carlo Method for array criticality calculations* Nucl. Tech. Vol.30, pp166-189 (1976)

65. D.J. DONAHUE *Neutron inelastic scattering from some collective nuclear states* Phys. Rev. Vol.128, No.3 (1962)

66. TRAIL AND RABOY, see R.B. DAY *Gamma rays from inelastic scattering* from *Progress in fast neutron physics* G.C. PHILLIPS, J.B. RISER AND J.R. MARION The University of Chicago Press

67. J. TOPPING *Errors of observation and their treatment* Institute of Physics and Phys. Soc. Monograph (1955)